Doctoral Dissertations   Student Theses and Dissertations

Spring 2009

Novel modulated antennas and probes for millimeter wave imaging applications

Mohamed A. Abou-Khousa

Recommended Citation

NOVEL MODULATED ANTENNAS AND PROBES FOR MILLIMETER WAVE

IMAGING APPLICATIONS

by

MOHAMED AHMED ABOUKHOUSA

A DISSERTATION

Presented to the Faculty of the Graduate School of the

MISSOURI UNIVERSITY OF SCIENCE AND TECHNOLOGY

in Partial Fulfillment of the Requirements for the Degree

DOCTOR OF PHILOSOPHY

in

ELECTRICAL ENGINEERING

2009

Approved by

Reza Zoughi
Richard E. Dubroff
Barbara N. Hale
David Pommerenke
R. Joe Stanley

ABSTRACT

Microwave and millimeter wave (300 MHz - 300 GHz) imaging techniques have shown great potential for a wide range of industrial and medical applications. These techniques are fundamentally based on measuring relative and coherent electromagnetic fields distributions, e.g., electric fields, around the object to be imaged. Various imaging systems can be devised for measuring relative electric field distributions; each with it own advantages and limitations. This dissertation is focused on addressing critical challenges related to the practical implementation of various microwave and millimeter wave imaging systems. Specifically, this research is meant to achieve three main objectives related to designing efficient modulated imaging methods/array elements, reducing the sensitivity to standoff distance variations in near-field imaging, and designing a simple and accurate vector network analyzer (VNA) for *in-situ* imaging applications. The concept of modulating millimeter wave antenna and scatterer structures, directly to increase the overall system sensitivity and reduce the image acquisition time, is central to the development presented herein. To improve upon the conventional modulated scatterer technique (MST) based on dipole scatterers; a new multiple loaded scatterer (MLS) method and novel loaded elliptical slot are introduced and analyzed. A unique near-field differential probe based on dual-loaded modulated single waveguide aperture is developed to compensate for and reduce the effect of standoff distance variations in near-field imaging. Finally, a novel vector network analyzer (VNA) design is introduced to meet the rising need for *in-situ* vector measuring devices. To realize a robust handheld millimeter wave VNA, a custom-designed waveguide phase shifter based on sub-resonant loaded slots is introduced. The proposed MLS method, modulated elliptical slot, dual-loaded modulated aperture probe, and VNA are thoroughly investigated and their efficacy for microwave and millimeter wave imaging is demonstrated.

ACKNOWLEDGMENT

TABLE OF CONTENTS

LIST OF ILLUSTRATIONS

LIST OF TABLES

1. INTRODUCTION

Electromagnetic (EM) fields in the microwave and millimeter wave range (300 MHz – 300 GHz) have many unique characteristics which make them particularly suitable for subsurface sensing purposes. Microwaves and millimeter waves can be used to interrogate and image through dielectric materials. These waves, unlike sound waves, do not experience severe attenuation while propagating in free-space. Furthermore, EM radiation in the microwave and millimeter wave range is non-ionizing, and hence, the associated imaging equipment and procedures are hazard-free and can be readily deployed anywhere, i.e., no need for special imaging environments [1].

Microwave and millimeter wave imaging and inspection techniques have shown great utility for a wide range of applications [1], [2]. These techniques have been successfully used for composite material inspection [3]-[5], corrosion under-paint evaluation [6], paint thickness monitoring [7], material characterization [8]-[10], and detection of surface cracks in metals [11], to name a few. Applying microwave imaging techniques for emerging applications such medical imaging and early detection of breast cancer has also shown promising viability [12], [13].

1.1. MICROWAVE AND MILLIMETER WAVE IMAGING

Active microwave and millimeter wave imaging is fundamentally based on measuring spatial (relative) distribution of an EM field, e.g., electric field, scattered from the object to be imaged [14]. In the imaging process, the object to be imaged is illuminated with microwaves or millimeter waves. When the object is made of dielectric material, the irradiating waves interact with the object as well as its interior structure. Depending of the properties of the object, some or all of the electric field associated with the irradiated waves scatter in different directions. The imaging system measures the scattered electric field in a certain spatial domain around the object. The spatial scattered field measurements are subsequently used to generate 2D or 3D images of the object's spatial and/or dielectric profiles [15]-[20].

1.1.1. Measurement of Electric Field Distribution. The simplest microwave and millimeter wave imaging system uses a single mechanically scanned antenna to measure the coherent electric field distribution in the spatial domain of

interest. Measuring the electric field of interest using a single scanned antenna is relatively simple, and hence, attractive for many applications. However, it requires lengthy scanning process to cover the whole spatial domain. Such lengthy scan process is generally undesirable in applications where real-time imaging is needed.

For real-time imaging, array of antennas can be utilized where each antenna (element) in the array provides a measure of the electric field at its location in the array. Using arrays provides for the required spatial field sampling while eliminating the need for time-consuming mechanical scanning. Proper design of the antenna array, array elements, and the receiving scheme are critical to realize relatively inexpensive, high-resolution, and sensitive imaging systems.

For high-resolution real-time imaging systems, spatially large and compact antenna arrays are required. For microwave and millimeter wave imaging, this requires implementing arrays with the number of elements ranging from few hundreds to few thousands. Designing receiving schemes for such large arrays is the main challenge in building microwave and millimeter wave imaging systems. Due to the required large number of array elements, using a dedicated receiver to measure the signal picked up by each element is prohibitively expensive and complex to implement in practice, especially in the millimeter wave frequency range. Hence, cost-effective receiving schemes should utilize spatial-signal multiplexing to reduce of number of receivers and the complexity of the high-frequency circuitry, i.e., switches, while providing high measurement sensitivity. The modulated scatterer technique (MST)-based imaging systems use such spatial multiplexing schemes [14]. With MST, an array of auxiliary scatterers, i.e., small loaded dipoles, are placed in the unknown field of interest. Figure 1.1 shows schematic of a generic MST-based electric field distribution measurement system using modulated dipoles. By controlled electrical loading, the properties of these dipoles, i.e., their scattering cross-sections, are modulated (changed over time), which in turn causes the scattered electric field to be modulated as well. The modulated electric field is then detected by a single receiver located at a remote position away from the object being imaged, as shown in Figure 1.1. In this way, the information about the field of interest, i.e., its magnitude and phase at the location of each scatterer, is "encoded" into the modulated signal received form each dipole. Basically, modulating the array dipoles allows for spatial electric field tagging/multiplexing and

thus, MST-based imaging systems can potentially be built with a single receiver only as desired to reduce design complexity and cost.
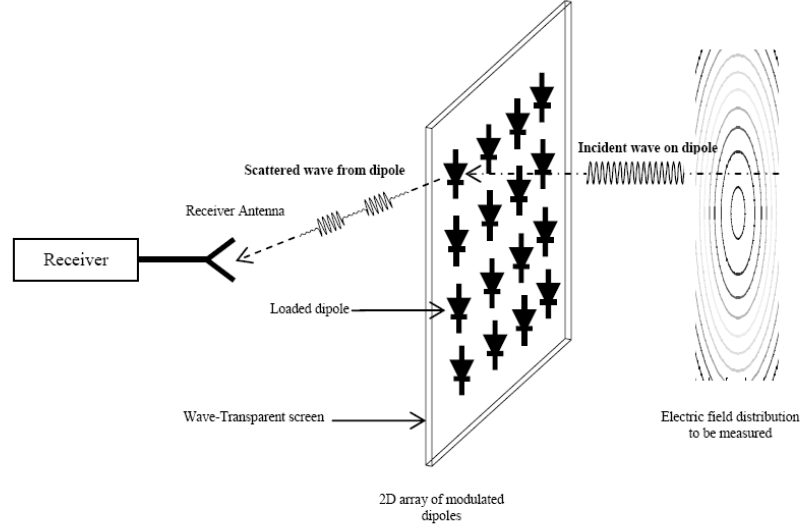
Figure 1.1. Schematic of an MST based electric field distribution measurement system.

Although MST allows for a relatively simple spatial multiplexing (compared to switched arrays for instance), the conventional MST-based imaging systems as known today suffer from major limitations that render their implementation in or near the millimeter wave frequencies very challenging. The inefficiency of the small dipoles that are typically used with these systems limits the modulation depth and the signal-to-noise ratio (SNR), and hence, the obtained electric field measurement sensitivity. Since the modulated scattered signal level from the array dipole is very small, the robustness of the conventional MST system is undermined by a residual carrier problem which complicates detecting the signal of interest. Furthermore, the mutual coupling among the array dipoles can significantly limit the imaging system dynamic range.

Depending on the type of processing performed on the measured electric field distribution and the nature of the resulting image, microwave and millimeter imaging

techniques can be grouped in two categories: tomography- and signature-based techniques. In microwave and millimeter wave tomography, the actual dielectric profile or distribution of the object being imaged is reconstructed via solving an inverse-scattering problem starting from the scattered field measurements, i.e., recalculating what caused this field to scatter. Subsurface features, i.e., defects or flaws, within the object appears in the reconstructed image in terms of their dielectric contrast with respect to the host object. Due to many factors, tomography-based imaging techniques are currently of limited practical utility. The inverse-scattering problems involved in these techniques are non-linear and ill-posed in nature [21]. Furthermore, these techniques often require stringent measurement setups that are difficult to realize (they need absolute magnitude field measurements) [21]. Hence, so far these techniques are still experimental and extensive research is being conducted to overcome their limitations [19].

On the other hand, signature-based microwave and millimeter wave imaging techniques are very common in practice. These techniques are founded on the idea that the scattering characteristics, i.e., reflection, absorption, etc., of a subsurface feature within a host object, i.e., its signature, is different from its surroundings. Instead of reconstructing the dielectric profile of the object from the scattered field measurements, i.e., solving the inverse problem, these techniques map one or more of the measured scattering characteristics into an intensity image directly. Signatures of interior features within the object appear in the obtained image with different intensities compared to their surrounding. The obtained resolution with these techniques, i.e., the capability of detecting two closely-spaced features within the object, depends on the effective illuminating footprint [6]. Compared to the tomography-based techniques, signature-based imaging techniques are simpler and more cost-effective. These techniques are based on relative field measurements as opposed to the tomography-based techniques. In particular, signature-based near-field and focused far-field imaging techniques are the most prominent imaging techniques that are applied nowadays in a wide range of imaging applications [1]. A brief description of each of these imaging techniques is provided next.

1.1.2. Near-Field Imaging. High-resolution microwave and millimeter wave images can be produced using near-field techniques where the object being imaged is in close proximity to the irradiating/receiving antenna, i.e., in its near-field. Reflectometers with open-ended rectangular waveguide apertures, as probing antennas, are commonly used for active near-field microwave and millimeter wave imaging [1]. The open-ended waveguide aperture is used to illuminate the object with a microwave/millimeter wave signal and to receive the scattered waves from the object. The probe footprint, and consequently the spatial resolution in this case is related to the waveguide aperture size, i.e., smaller waveguide aperture yields higher spatial resolution [17]. Typically, the detection system is designed to produce a dc signal proportional to the phase and/or magnitude of the electric field associated with the scattered/reflected wave. In most cases, the detection system may simply consist of a diode detector, e.g., a standing-wave reflectometer. For imaging purposes, the waveguide aperture is scanned over the object and the measured output dc signal is mapped into a 2D intensity raster image. Using a simple and portable standing-wave reflectometer, which can be optimized for several parameters to enhance the detection sensitivity, makes near-field imaging techniques attractive for many applications. For instance, recent investigations on the capability of various imaging methods for honeycomb-based composites inspection, i.e., radomes, revealed that millimeter wave near-field imaging techniques offer distinct advantages in terms of the detection capability and resolution over other imaging methods considered in that investigation [22], [23]. The result of these recent investigations, which were conducted on two composite radome panels with various subsurface flaws, is summarized in Table 1.1. As shown in Table 1.1, near-field millimeter wave imaging potentially provides a simple and effective alternative to the current imaging methods applied for composite radome structure inspection purposes [22].

The main limitation of near-field imaging probes is their intrinsic sensitivity to the variations in the distance between the probing antenna and the object i.e., standoff distance [24]. Such variations can potentially mask the signature of a defect in an image, and hence adversely influence the detection capability of the probe.

1.1.3. Focused Far-Field Imaging. In far-field imaging techniques, the scattering characteristics from the object to be imaged are measured in the far-field

Table 1.1. Summary of detection and resolution attributes of four imaging methods [22].

Imaging Method	Detection		Resolution/ Complexity
	Panel #1 (22 flaws)	Panel #2 (15 flaws)	
X-Ray Computed Tomography	21 out of 22	14 out of 15	High /High
Near-Field Millimeter Wave	12 out of 22	13 out of 15	High/ Low
Shearography	8 out of 22	8 out of 15	Low/ Low
Through-Transmission Ultrasonic Testing	16 out of 22	8 out of 15	Modrate/ Moderate

of the illuminating antenna. To obtain high spatial resolution, i.e., small effective footprint, a focused antenna, i.e., lens antenna [16], or synthetic aperture focusing techniques (SAFT) [25] may be used. SAFT is basically based on well-established synthetic aperture radar (SAR) concepts. Synthetic aperture focusing, although effective, requires coherent measurements, i.e., phase and magnitude, of the scattered field over a certain spatial domain. Single scanned antenna or MST arrays [18] with a single receiver can be potentially used for this purpose. Currently, focused imaging with SAFT necessitates the use of vector measuring instruments/transceivers such as a vector network analyzer (VNA) [25]. However, These sophisticated transceiver systems, i.e., a VNA, are typically bulky and expensive. These facts limit the practical use of focused far-field imaging based on SAFT.

1.2. QUANTITATIVE INSPECTION

Quantitative inspection has significant utility in many applications. In this context, microwave and millimeter wave imaging and inspection techniques must be capable of closely evaluating the physical properties of the object being inspected, i.e., dimensions, dielectric properties, etc. [26], [27]. To this end, phase and magnitude information, i.e., vector measurements, are typically needed for inspection. Unfortunately, realizing phase and magnitude detectors at microwaves and millimeter wave

frequencies with the current technology is rather expensive. As with synthetic aperture focused imaging, most of the current promising quantitative microwave and millimeter wave inspection techniques require expensive and bulky VNAs to perform the measurements [26]. Hence, there is a great need for a simple, portable, and relatively inexpensive alternative system to facilitate *in-situ* vector measurements as required in these applications .

1.3. SCOPE AND MAJOR CONTRIBUTIONS

This endeavor is directed towards addressing some of the practical limitations associated with applying microwave and millimeter wave imaging and inspection techniques as they were briefly described above. Specifically, this research is meant to achieve three main objectives related to:

- Improving upon the conventional MST-based systems used for electric field distribution measurements, i.e., proposing new methods and modulated elements which yield higher modulation depth and sensitivity,

- Developing imaging probes to compensate for standoff distance variations in near-field imaging,

- Devising inexpensive, accurate and handheld vector measuring devices, i.e., VNA, to be used in imaging as well as for quantitative inspection.

The concept of loading and modulating millimeter wave antenna and scatterer structures directly to increase the overall system sensitivity and reduce the image acquisition time is central to the development presented in this dissertation. The major contributions of this dissertation are described next.

The sensitivity of the conventional MST based on modulated dipoles is studied theoretically and experimentally using a new general approach. The developed approach relates the modulated scatterer characteristics to the signal-to-noise ratio (SNR), and hence, the measurement sensitivity.

A novel multiple-loaded scatterer (MLS) method is developed to improve upon the shortcomings of the conventional MST-based imaging arrays. The proposed MLS method is based on modulating a single strong scatterer loaded with PIN diodes

as opposed to the small loaded dipoles used in the conventional MST arrays. The MLS method allows for accurate recovery of an unknown electric field distribution with measurements conducted at a single observation point, i.e., a single receiver is needed. Since the MLS method is not based on discrete elements, the limiting factors of the conventional MST which are related to array element dispersion and mutual coupling do not limit its performance. Furthermore, the modulated scattered signal level and the modulation depth in the MLS implementation is much higher than that in the conventional MST case. In practice, this fact translates to higher measurement sensitivity. Within the effort of developing the MLS, a new numerical method to analyze loaded wire antennas and scatterers based on the recently proposed Maxwellian Circuits theory is also introduced.

A new modulated slot design is introduced as an alternative to the inefficient loaded dipoles conventionally used with the MST-based imaging systems. The proposed slot is a compact resonant slot loaded with a PIN diode. Although, the longest dimension of the slot is only around one third of the operating wavelength, it is resonated to work at the frequency of interest by special loading. The salient features of the proposed slot are that it results in high modulation depth, i.e., close to 100%, and exhibits very small mutual coupling once used in an array. Consequently, when array of these slots are used in an imaging array, they result in higher sensitivity and dynamic range compared to arrays of loaded dipoles.

A unique near-field microwave and millimeter wave differential probe design based on a dual-loaded modulated single waveguide aperture is developed. In this design, two PIN diode-loaded dipoles are used to modulate the aperture of the waveguide. Using this novel design the undesired influence of standoff distance variation in near-field imaging can be eliminated, or otherwise significantly reduced by non-coherently detecting and subtracting the signals measured at two different aperture modulation states. In addition, this differential probe efficiently overcomes the limitations of the previously developed standoff distance variation compensation methods.

Finally, a novel vector network analyzer (VNA) is developed to meet the rising needs for wideband, simple, handheld, relatively inexpensive, and *in-situ* vector measuring devices. Such a device can be effectively used for quantitative microwave

and millimeter wave inspection and imaging as well as many other critical applications such as circuit characterization, reflectometry, and material characterization. The proposed VNA design is founded on simple standing-wave measurements, and hence, it circumvents the expensive heterodyne detection scheme required to implement tuned-receiver-based VNAs. It is also unique compared to the previously developed power measurement-based VNA systems in that it utilizes a single power detector, and it does not require multi-port coupling devices. Furthermore, the proposed VNA can be calibrated with three known standards only to yield accurate vector measurements. To realize a handheld millimeter wave VNA based on the proposed approach, a custom-designed waveguide phase shifter is introduced. The developed phase shifter uses loaded sub-resonant slots cut into the wall of a waveguide. Loading the slots with PIN diodes and thereafter controlling the impedance of these diodes electronically can provide highly stable and distinctive phase shifts as needed for this VNA design.

This dissertation is organized as follows. Section 2 gives the pertinent theoretical background, i.e., modeling and analysis of loaded wire antennas and scatterers, needed to lay the foundation for the MLS method. The formulation of the MLS method, along with several key simulation results illustrating its efficacy for electric field distribution measurement, is presented in Section 3. The modulated slot design devised for imaging systems is introduced in Section 4. Section 5 gives detailed analysis and performance evaluation of the dual-loaded modulated aperture probe developed for near-field imaging. Section 6 describes the design of the developed VNA and demonstrates its accuracy for complex reflection coefficient measurements. The VNA performance is investigated via simulations as well as experimental measurements obtained using X- and Ka-band VNA prototypes while considering various critically important system parameters. Finally, concluding remarks are highlighted in Section 7.

2. LOADED ANTENNAS AND SCATTERERS

Loaded wire antennas and scatterers are used in wide range of applications including modulated scatterer techniques (MST) devised for electromagnetic fields measurements [28], [29], antenna pattern synthesis, radar cross-section (RCS) control and optimization (see [30] and the references therein). The design and optimization of loaded wire antennas and scatterers involve analyzing the near- and far-field parameters over a wide range of frequencies and/or excitations and/or loading conditions. An integral equation formulation with the Method-of-Moment (MoM) solution is typically applied to such problems. The general analysis of loaded wire antennas and scatterers is considered in this section.

2.1. PRELIMINARY THEORY

Most of the preliminary theory presented here, i.e., Pocklington's integrodifferential equation and the method-of-moments, is well-established and used to serve as the foundation to subsequent analysis. The idea of dealing with a loaded scatterer by considering scattering and radiation sub-problems is of special importance. In addition, modeling the load as an equivalent voltage is fundamental to the development presented in the next section.

2.1.1. Pocklington's Integrodifferential Equation (IE). Pocklington's electric field integrodifferential equation (IE) is widely used to find the electric current over thin linear scatterers or antennas. We consider scattering from a perfect electric conductor (PEC) cylindrical wire scatterer of length L and radius a as shown in Figure 2.1. The scatterer is oriented with its axis along the z-axis. Due to an incident electric field, a surface current is induced on the scatterer structure. This current density, linear in this case, causes the scatterer to reradiate some of the incident energy. The total electric field at any point in the medium surrounding the wire is the superposition of the incident and scattered electric fields. The intention is to find the current induced on the wire.

Due to the presence of the wire, the medium is bounded at the surface of that wire with PEC boundary condition of vanishing tangential electric field. It is always
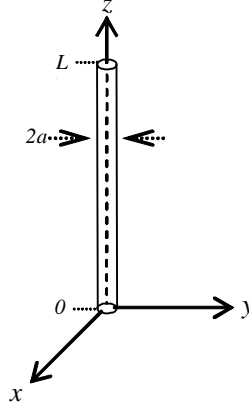
Figure 2.1. Geometry of a cylindrical wire scatterer.

desirable to solve such scattering problems in a medium where we know how to con-
struct the solution, i.e., a medium for which the Green's function is known. This is
true since the boundary conditions for a given bounded medium are embedded in the
corresponding Green's function. For the problem at hand, there is no known Green's
function for the given boundary conditions. However, the problem itself can be mod-
ified using the surface equivalence principle whereby the wire is removed from the
medium and an imaginary surface with an equivalent current density is introduced in
lieu of the wire. The scattering problem can now be solved by considering the radia-
tion due to the introduced equivalent current density in the unbounded medium. For
the unbounded medium, we know how to construct the solution using the free-space
Green's function which satisfies the radiation boundary condition. Subsequently, we
enforce the PEC boundary condition at each point on the imaginary surface coinciding
with original surface of the wire.

From the PEC boundary condition, the tangential component of the total
electric field should be zero at the surface of the scatterer. Hence, for any arbitrary
point on the surface of the scatterer (primed coordinates are used for these source
points), one can write the PEC boundary condition as [31],

$$\left[\mathbf{E}^i(r') + \mathbf{E}^s(r')\right]_{\tan} = 0, \tag{1}$$

such that,

$$\mathbf{E}^s(\mathbf{r}) = -j\omega\mathbf{A} - j\frac{1}{\omega\mu\varepsilon}\boldsymbol{\nabla}(\boldsymbol{\nabla}\cdot\mathbf{A}) = -j\omega\mathbf{A} - \boldsymbol{\nabla}V, \tag{2}$$

where $\mathbf{A}$ and V are the vector magnetic and scalar electric potentials, respectively, and ω is the angular frequency, μ and ε are the permeability and permittivity of the surrounding medium, respectively.

For very thin wires (relative to the wavelength λ), the current density has only one component (neglecting the edge effect); J_z and it does not vary with ϕ [31]. Thus, equations (1) and (2) can be written as,

$$E_z^s(z') = -E_z^i(z') \text{ (Boundary condition)}, \tag{3}$$

$$E_z^s(z') = -j\omega A_z - \frac{dV}{dz}, \tag{4}$$

$$\frac{dA_z}{dz} = -j\omega\mu\varepsilon V \quad \text{(Lorentz condition)}, \tag{5}$$

where, for thin wires,

$$\begin{aligned} A_z &= \mu\int_0^L\int_0^{2\pi} J_z(z')G(z,z')ad\phi'dz' \\ &= \mu\int_0^L 2\pi a J_z(z')G(z,z')dz' \\ &= \mu\int_0^L I(z')G(z,z')dz', \end{aligned} \tag{6}$$

where $I(z') = 2\pi a J_z(z')$ is an equivalent filament-line current source defined along the scatterer. For thin scatterers, the following reduced-kernel approximation based on the free-space Green's function is used to calculate A_z,

$$G(z,z') = \frac{e^{-jkR}}{4\pi R}, \quad R \approx \sqrt{a^2 + (z-z')^2}. \tag{7}$$

To summarize, scattering from a thin wire is fully described by solving the following equations for the induced current $I(z')$,

$$
\begin{aligned}
\frac{dV}{dz} &= -j\omega A_z + E_z^i(z'), \\
\frac{dA_z}{dz} &= -j\omega\mu\varepsilon V, \\
A_z &= \mu \int_0^L I(z')G(z,z')dz'.
\end{aligned}
\tag{8}
$$

After some straightforward manipulations, the equations in (8) can be expressed in the following integrodifferential equation, commonly known as, Pocklington's integrodifferential equation (IE),

$$
\int_0^L I(z') \left[\frac{d^2}{dz} + k^2 \right] G(z,z')dz' = -\frac{jk}{\eta} E_z^i(z'),
\tag{9}
$$

where $\eta = \sqrt{\mu/\varepsilon}$ and $k = \omega\sqrt{\mu\varepsilon}$ are the intrinsic impedance and the propagation constant characterizing the surrounding medium. Equation (9) can be also written as [31],

$$
\int_0^L I_z(z')K(z,z')dz' = -\frac{j4\pi k}{\eta} E_z^i(z'),
$$

$$
K(z,z') = \frac{e^{-jkR}}{R^5} \left[(1+jkR)(2R^2 - 3a^2) + (kaR)^2 \right].
\tag{10}
$$

The kernel $K(z,z')$ exhibits "singular" behavior of order $1/R^3$ when the source and observation points approach each other, i.e., a and $(z-z')$ are small. This behavior is especially apparent for very thin wires. This singularity is treated here using standard singularity subtraction method as proposed in [32].

Equation (10) can be used for radiation problems as well. To this end, the impressed voltage at the feed terminals is modeled as delta gap source, i.e., $V(z') = V_o\delta(z'-z_f)$, where z_f is the feed point. In this case, the excitation $E_z^i(z')$ is replaced with $V_o\delta(z'-z_f)/l_s$ for radiation problems with l_s being the length of the gap (typically l_s is set equal to one segment length in the method-of-moment solution).

2.1.2. Method-of-Moment (MoM) Solution. Pocklington's IE is solved typically using the Method of Moment (MoM) [33]. As per this method, the wire structure is modeled as N interconnected segments each of length $l_s = L/N$ (subdomains) centered at $\{z_n : n = 1, 2, ..., N\}$. The induced current distribution over the wire, $I(z')$, is expanded in terms of the currents at the center of each segment, $I(z_n)$, using subdomain basis functions $f_n(z')$ as,

$$I(z') \simeq \sum_{n=1}^{N} I(z_n) f_n(z'). \tag{11}$$

There are various possible choices of basis functions to be used with MoM [34]. Herein, the following simple set of pulse basis functions are used for the MoM expansion [31],

$$f_n(z) = \left\{ \begin{array}{c} 1 : z_n - l_s/2 \leq z \leq z_n + l_s/2 \\ \\ 0 : \text{ elsewhere} \end{array} \right\}. \tag{12}$$

Substituting (11) into (10) yields,

$$\sum_{n=1}^{N} I(z_n) \int_{z_n - l_s/2}^{z_n + l_s/2} K(z, z') dz' = -\frac{jk}{\eta} E_z^i(z'). \tag{13}$$

Testing the above equation using the point matching (collocation) technique at points $\{z_m : m = 1, 2, ..., N\}$ along the scatterer length,

$$\sum_{n=1}^{N} I(z_n) \int_{z_n - l_s/2}^{z_n + l_s/2} K(z_m, z') dz' = -\frac{j4\pi k}{\eta} E_z^i(z_m). \tag{14}$$

Basically, the collocation method enforces Pocklington's IE at the test points only. Using matrix notation, equation (14) is written as,

$$\mathbf{ZI} = \mathbf{e}, \tag{15}$$

where,

$$\mathbf{I} = [I(z_1), I(z_2), \ldots, I(z_N)]^T, \text{ and} \tag{16}$$

$$\mathbf{e} = (\qquad -j4\pi k/\eta) \left[E_z^i(z_1), E_z^i(z_2), \ldots, E_z^i(z_N) \right]^T, \tag{17}$$

are the unknown current distribution and the excitation $(N \times 1)$ column vectors, respectively, and $\mathbf{Z}$ is the $(N \times N)$ impedance matrix of the wire whose elements are given by,

$$Z_{mn} = \int\limits_{z_n - l_s/2}^{z_n + l_s/2} K(z_m, z')dz'. \tag{18}$$

Finally, the MoM solution is given as,

$$\mathbf{I} = \mathbf{Z}^{-1}\mathbf{e} = \mathbf{Y}\mathbf{e}, \tag{19}$$

where $\mathbf{Y} = \mathbf{Z}^{-1}$ is the wire admittance matrix.

2.1.3. Analysis of Loaded Antennas and Scatterers. The general analysis of wire antennas and scatterers loaded with lumped linear elements can be found in [35]. The scattering from impedance loaded wire of length L and radius a loaded at a point, z_L, as depicted in Figure 2.2 can be analyzed using linear network theory (assuming the loads are linear or can be linearized). Consider a wire loaded with arbitrary impedance Z_L (or admittance $Y_L = 1/Z_L$). The two terminals of this load identify a port, say port 1, with well-defined current I_1 and voltage V_1. In the scattering problem, the wire is illuminated by an electric field produced by some source (might be at infinity), for instance, an infinitesimal dipole as shown in Figure 2.2. In this case, the terminals of the infinitesimal dipole identify a second port, port 2, with current I_2 and voltage V_2. For radiation problems, , i.e., loaded antenna, the second port is located on the wire. The scattering problem will be treated in detail herein. Similar development can be applied directly to the radiation problem as well.

As far as the induced current on the scatterer, and consequently, the resultant scattered field are concerned, the scattering from a loaded wire can be fully described by the superposition of the current solutions of two sub-problems; scattering from short-circuited wire, i.e., when the load is replaced by a short circuit, and the radiation
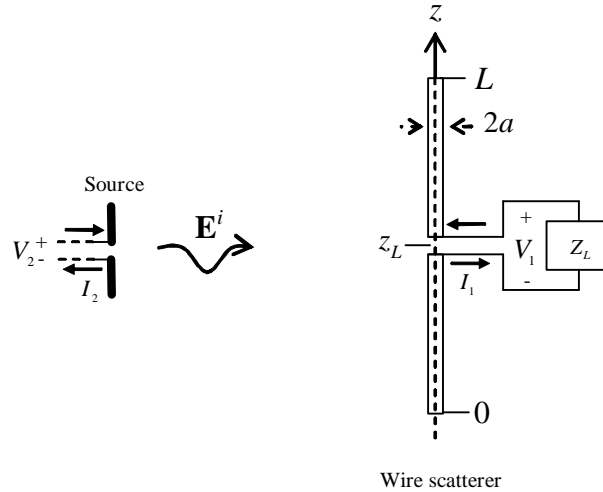
Figure 2.2. Scattering from impedance-loaded wire scatterer.

from the wire when it is fed at the load location with a *load-equivalent voltage, v^e* [30], [35], as illustrated schematically in Figure 2.3. The first problem, finding the induced current on a wire scatterer due to a certain incident field, can be addressed by solving Pocklington's IE using the MoM as described earlier. The current solution for the second problem can be also obtained using Pocklington's IE once the load-equivalent voltage, v^e, is determined. Determination of this voltage follows from the two-port network model and the load boundary condition as shown next.
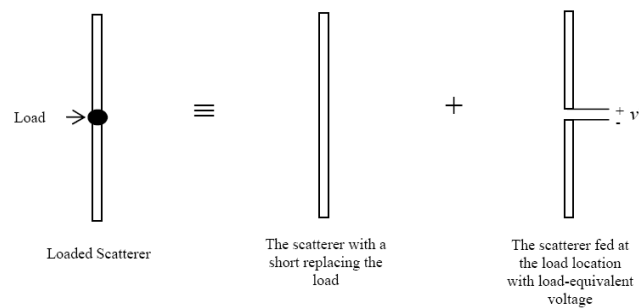
Figure 2.3. Loaded scatterer problem as superposition of two sub-problems.

The port currents and voltages are related by the short-circuit parameters as,

$$
\begin{bmatrix} Y_{11} & Y_{12} \\ Y_{21} & Y_{22} \end{bmatrix} \begin{bmatrix} V_1 \\ V_2 \end{bmatrix} = \begin{bmatrix} I_1 \\ I_2 \end{bmatrix},
\tag{20}
$$

where Y_{ii} and Y_{ij} are the self- and transfer-admittances, respectively. The short-circuit parameters are defined as [36],

$$
Y_{ii} = \frac{I_i}{V_i}, \ \text{with} \ V_k = 0, \ k \neq i,
\tag{21}
$$

$$
Y_{ij} = \frac{I_i^{sc}}{V_j}, \ \text{with} \ V_k = 0, \ k \neq j,
\tag{22}
$$

where I_i^{sc} is the current passing through the ith short-circuited port when j^{th} port is driven by a voltage V_j.

In both radiation and scattering problems, the load imposes the following condition on the port voltage,

$$
V_1 = -I_1/Y_L.
\tag{23}
$$

The load-equivalent voltage is found by solving (20) and (23) for V_1, which yields [35],

$$
v^e \triangleq V_1 = \frac{-Y_{12}}{Y_{11} + Y_L} V_2 = \frac{-I_1^{sc}}{Y_{11} + Y_L} = \frac{-I^{sc}(z_L)}{Y_{11} + Y_L},
\tag{24}
$$

where $I_1^{sc} = I^{sc}(z_L)$ is the current passing through the load port located at z_L when the load is short-circuited. This term is henceforth referred to as the load short-circuit current.

When the illuminating source is far from the scatterer, i.e., the presence of the source does not change the shape of the current distribution on the scatterer and vice-versa, Y_{11} represents the wire input admittance when it is fed at the load location. This parameter can be calculated using arbitrary non-zero voltage-based delta-gap excitation with Pocklington's equation. The load short-current, $I^{sc}(z_L)$, is obtained from the induced current distribution on the short-circuited scatterer due to the incident field, i.e., the solution to the first sub-problem. Let this current be,

$$
\mathbf{I}^{sc} = [I^{sc}(z_1), I^{sc}(z_2), \ldots, I^{sc}(z_N)]^T,
\tag{25}
$$

the total current induced on the loaded scatterer can be written as,

$$\mathbf{I} = \mathbf{I}^{sc} + \left(\frac{-4\pi jk}{\eta l_s} \right) \mathbf{Y} \mathbf{v}^e, \tag{26}$$

where $\mathbf{v}^e$ is a vector of dimension $N \times 1$ with all zeros except at the nth position which corresponds to the load location along the wire where it is set to v^e. The above analysis is general and can be applied to scatterers and antennas loaded with multiple loads.

To illustrate the superposition concept, Figure 2.4 shows the magnitude and phase distributions of the current induced on a wire scatterer of length $L = \lambda$ and radius $a = 0.001\lambda$ loaded at $z = \lambda/2$ with $Z_L = \infty$ (open circuited) due to an incident broadside uniform plane wave.
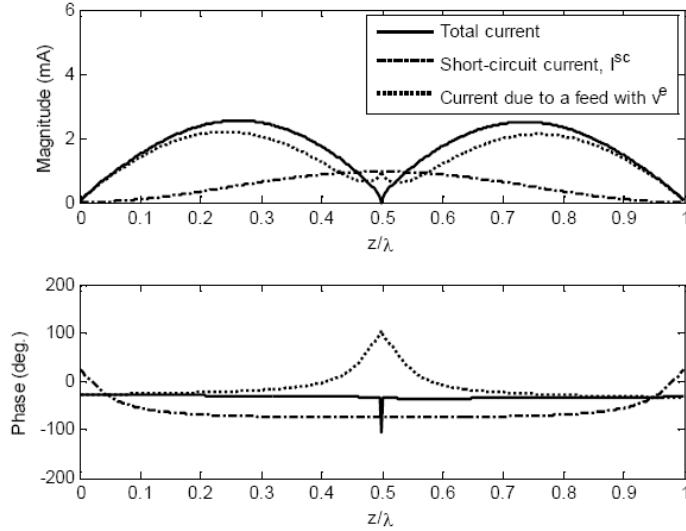
Figure 2.4. Magnitude and phase distributions of the current induced on a wire scatterer of length $L = \lambda$ and radius $a = 0.001\lambda$ due to an incident broadside uniform plane wave.

The short-circuit current and the current induced due to feeding with v^e (as calculated) are also shown in Figure 2.4. At the load location, open-circuited in this

case, the short-circuit current and the current due to the load equivalent voltage cancel each other (they are of the same magnitude and 180° out of phase). Consequently, the obtained total current distribution is similar to the typical current distribution on a center-fed $\lambda-$long dipole antenna.

The normalized backscattering radar cross-section (RCS) was computed for a center-loaded wire scatterer of variable length with fixed length-to-diameter ratio $L/2a = 74.2$ subject to an incident broadside uniform plane wave. Figure 2.5 shows the computed normalized RCS for different loading cases (some considered in [35]). The normalized RCS was computed as [32],

$$\sigma/\lambda^2 = 14400\pi^3 \left| \int_0^L I(z')dz' \right|^2.$$ (27)
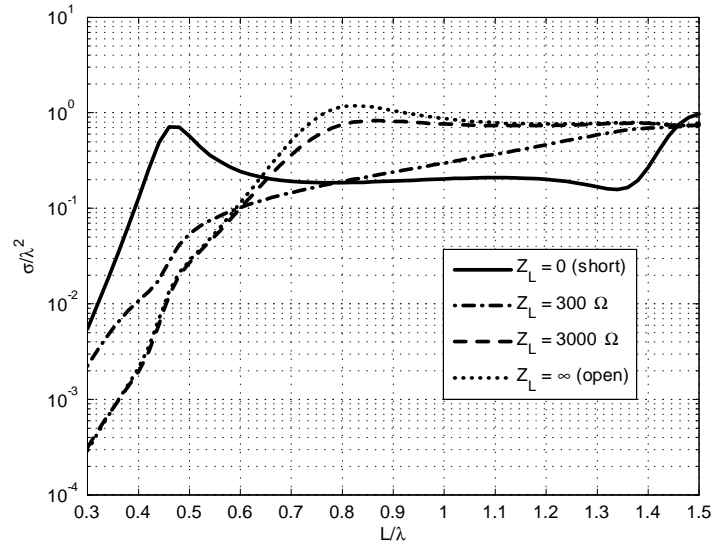
Figure 2.5. Normalized radar cross-section of a center loaded λ-long wire scatterer as a function of its normalized length for different loads.

The obtained results shown in Figure 2.5 are in good agreement with the results of [35] considering the same loading scenarios.

2.2. MAXWELLIAN CIRCUIT (MC) BASED ANALYSIS

The recently proposed theory of Maxwellian circuit (MC) [37] has provided solutions identical to integral equation solutions describing radiation and scattering from thin wire structures. The Maxwellian circuits are equivalent circuit models, e.g., RLC circuits, which provide valid solutions to Maxwell's equations describing radiation and scattering from thin wire structures. They are not low frequency or quasi-static models which fail to predict the performance at high frequencies. As of now, MCs were developed only for wire antennas and scatterers, e.g., dipoles, printed bends, etc. Although the MC theory has been subsequently used to analyze various linear wire antennas and scatterers [37]-[39], its application for analyzing loaded wire structures has yet to be demonstrated [40].

Here, the use of the MC theory for the problem of loaded wire antennas and scatterers is investigated. Unlike the solution method presented in [37]-[39] which is based on Euler forward formula and requires solving for the voltages and currents simultaneously (in essence doubling the number of unknowns), the solution developed here is based on the Finite Element Method (FEM). When linear elements are used for the FEM solution, the number of unknowns is reduced to half of those required for the Euler forward formula. Furthermore, with the proposed model, the load can be placed virtually anywhere along the wire and more than one load can be modeled simultaneously. The utility of the FEM to solve the MC model differential equations and handling the load condition is demonstrated by considering various radiation and scattering scenarios.

2.2.1. MC Model. In [37]-[39], it has been shown that the solution of the Pocklington's IE describing scattering from a wire similar to the one shown in Figure 2.1 is identical to the solution obtained from the following ordinary differential

equation describing an equivalent transmission line (TL) model for the wire,

$$\frac{dV(z)}{dz} = -Z(z)I(z) + \alpha(z)V(z) + E_z^i(z), \tag{28}$$

$$\frac{dI(z)}{dz} = -Y(z)V(z) + \beta(z)I(z), \tag{29}$$

$$I(0) = I(L) = 0 \quad \text{(current boundary condition)}, \tag{30}$$

with the per-unit parameters $Z(z) = R(z) + j\omega L(z)$ and $Y(z) = G(z) + j\omega C(z)$. For scatterers and antennas made of perfect electric conductors, the resistance $R(z)$ can be interpreted as the per-unit (distributed) radiation resistance, and the per-unit conductance $G(z)$ is zero [40]. In this model, radiation and scattering are accounted for by introducing the dependent current and voltage sources, through the parameters $\alpha(z)$ and $\beta(z)$, to the conventional TL equations. The salient feature of the MC is that the model parameters are said to be dependent only upon the geometry of the problem, i.e., they are independent of the excitation and terminal boundary conditions.

2.2.2. MC Parameter Extraction. The MC parameters $Z(z)$, $\alpha(z)$, $Y(z)$, and $\beta(z)$ are determined from two independent solutions, say $I_1(z)$ and $I_2(z)$, of the homogenous form of the Pocklington's IE obtained by enforcing two boundary conditions as outlined in [37]-[39]. Basically, these two current solutions are obtained by solving,

$$\int_0^L I_1(z')K(z, z')dz' = 0, \quad I_1(0) = A, \tag{31}$$

and,

$$\int_0^L I_2(z')K(z, z')dz' = 0, \quad I_2(L) = B, \tag{32}$$

such that A and B can not be both set to zero.

Equations (31) and (32) are solved for $I_1(z)$ and $I_2(z)$, respectively, using the MoM as before. Subsequently, the voltage corresponding to each solution is found using (8) as,

$$V_j(z) = \frac{j\eta}{k} \int_0^L I_j(z')\frac{dG(z, z')}{dz}dz', \quad j = 1, 2. \tag{33}$$

Using the obtained current and voltages in (29) and the homogenous form of (28)), and then segmenting the wire into N segments as used with the MoM with segment centers z_n, the following two systems of equations are obtained,

$$
\begin{bmatrix} V_1(z_n) & -I_1(z_n) \\ V_2(z_n) & -I_2(z_n) \end{bmatrix} \begin{bmatrix} \alpha(z_n) \\ Z(z_n) \end{bmatrix} = \begin{bmatrix} \frac{dV_1(z)}{dz}\big|_{z_n} \\ \frac{dV_2(z)}{dz}\big|_{z_n} \end{bmatrix},
\tag{34}
$$

$$
\begin{bmatrix} -V_1(z_n) & I_1(z_n) \\ -V_2(z_n) & I_2(z_n) \end{bmatrix} \begin{bmatrix} Y(z_n) \\ \beta(z_n) \end{bmatrix} = \begin{bmatrix} \frac{dI_{z1}(z)}{dz}\big|_{z_n} \\ \frac{dI_{z2}(z)}{dz}\big|_{z_n} \end{bmatrix}.
\tag{35}
$$

These systems of equations can be solved for the MC parameters at the segment centers $Z(z_n)$, $\alpha(z_n)$, $Y(z_n)$, and $\beta(z_n)$. The distributions of these parameters are approximated from their corresponding values found at the segment centers.

For wire antennas, the excitation $E_z^i(z)$ is replaced by feeding voltage as it was described for Pocklington's IE. From the above development, it is remarked that the MC parameters depend only on the frequency of operation and the geometry of the scatterer/antenna. Since the MC parameters are extracted from the homogenous form of the Pocklington's IE, they don't depend on the feed location in the case of an antenna or the incident electric field in the case of a scatterer. Hence, the MC parameters found at a certain frequency can be essentially used to find the current solution for wide range of excitations, i.e., different feed locations, different incidence angles, etc.

2.2.3. Finite Element Method (FEM) Formulation. The FEM [41] can be used to solve the MC TL model once the model parameters are extracted. To this end, the weak-form of the MC differential equations should be developed. Equation (29) can be written as,

$$
\begin{aligned}
V(z) &= \frac{-1}{Y(z)} \frac{dI(z)}{dz} + \frac{\beta(z)}{Y(z)} I(z) \\
&= \frac{-1}{Y(z)} \frac{dI(z)}{dz} + C(z)I(z),
\end{aligned}
\tag{36}
$$

where $C(z) = \frac{\beta(z)}{Y(z)}$. Using (36) into (28),

$$-\frac{d}{dz}\left[\frac{1}{Y(z)}\frac{dI(z)}{dz}\right] + \frac{d}{dz}\left[C(z)I(z)\right] = -Z(z)I(z)$$

$$-\frac{\alpha(z)}{Y(z)}\frac{dI(z)}{dz} + \alpha(z)C(z)I(z) + E_z^i(z), \qquad (37)$$

the TL wave equation can be now written as,

$$-\frac{d}{dz}\left[\frac{1}{Y(z)}\frac{dI(z)}{dz}\right] + \frac{d}{dz}\left[C(z)I(z)\right] + \left[Z(z) - \alpha(z)C(z)\right]I(z)$$

$$+\frac{\alpha(z)}{Y(z)}\frac{dI(z)}{dz} - E_z^i(z) = 0, \qquad (38)$$

using $\frac{d}{dz}\left[C(z)I(z)\right] = C(z)\frac{dI(z)}{dz} + C'(z)I(z)$, $C'(z) = \frac{dC(z)}{dz}$, and making the z dependence implicit, the TL wave equation can be written compactly as,

$$-\frac{d}{dz}\left[\frac{1}{Y}\frac{dI}{dz}\right] + \frac{1}{Y}\left[\alpha + \beta\right]\frac{dI}{dz} + \left[Z - \alpha C + C'\right]I - E_z^i = 0. \qquad (39)$$

Notice that the above equation reduces to the conventional TL equation when the parameters α and β are set to zero. This differential equation is linear and hence it admits a quadratic form , i.e., weak form [40]. To develop the weak-form, let the weighting function be $\Phi(z)$ (as defined later). Multiplying (39) by $\Phi(z)$ and integrating over the domain $[0, L]$,

$$\int_0^L \left(-\Phi\frac{d}{dz}\left[\frac{1}{Y}\frac{dI}{dz}\right] + \frac{1}{Y}\left[\alpha + \beta\right]\Phi\frac{dI}{dz} + \right.$$

$$\left. \left[Z - \alpha C + C'\right]\Phi I - \Phi E_z^i\right) dz = 0. \qquad (40)$$

Integrating the first term in the integrand by parts results in,

$$-\int_0^L \Phi\frac{d}{dz}\left[\frac{1}{Y}\frac{dI}{dz}\right] dz = -\left[\Phi\frac{1}{Y}\frac{dI}{dz}\right]_0^L + \int_0^L \frac{1}{Y}\frac{d\Phi}{dz}\frac{dI}{dz}dz$$

Using this result, the weak-form becomes,

$$
\int\limits_0^L \left(\frac{1}{Y} \frac{d\Phi}{dz} \frac{dI}{dz} + \frac{1}{Y} \left[\alpha + \beta \right] \Phi \frac{dI}{dz} + \left[Z - \alpha C + C' \right] \Phi I - \Phi E_z^i \right) dz
$$

$$
- \left[\Phi \frac{1}{Y} \frac{dI}{dz} \right]_0^L = 0, \quad (41)
$$

such that,

$$
I(z) \quad : \quad \begin{cases} \text{Primary variable} \\ \text{Essential boundary condition on } I(z) \end{cases}
$$

$$
\frac{1}{Y} \frac{dI}{dz} \quad : \quad \begin{cases} \text{Secondary variable (element boundary term)} \\ \text{Natural boundary condition on } V(z) \end{cases}
$$

Using (36), the secondary variable is found as,

$$
\Phi \frac{1}{Y} \frac{dI}{dz} = -\Phi V + \Phi C I. \quad (42)
$$

The weak-form can be solved for the current using FEM, i.e., using linear elements [41]. Let the domain $[0, L]$ be divided into N equal elements each of length l. The nth element support (subdomain) is $\Omega^n = [z_1^n, z_2^n]$, where z_1^n and z_2^n are the z-coordinates (global) of the 1st and 2nd nodes of the nth element, $n = 1, 2, ..., N$. The current over the nth element is approximated in terms of the node currents I_j^n, $j = 1, 2$, using linear normalized (local) interpolation functions,

$$
I^n(\bar{z}) = \sum_{j=1}^2 \bar{\Phi}_j^n(\bar{z}) I_j^n, \quad \bar{z} \in [0, l], \quad (43)
$$

where the linear interpolation functions are,

$$
\bar{\Phi}_1^n(\bar{z}) = 1 - \bar{z}/l, \bar{\Phi}_2^n(\bar{z}) = \bar{z}/l.
$$

Over the nth element support, the weak-form is written as,

$$\int_0^l \left(\frac{1}{Y^n} \frac{d\Phi}{d\bar{z}} \frac{dI^n}{d\bar{z}} + \frac{1}{Y^n} \left[\alpha^n + \beta^n\right] \Phi \frac{dI^n}{d\bar{z}} + \right.$$

$$\left. \left[Z^n - \alpha^n C^n + C'^n\right] \Phi I^n - \Phi E_z^i \right) d\bar{z} - \left[-\Phi V^n + \Phi C^n I^n\right]_0^l = 0, \qquad (44)$$

where Y^n, α^n, β^n, Z^n, C^n, and C'^n are the corresponding TL parameters over the nth element support (assumed to be constant over the element). Using (43) into ((44)), and using the weighting function $\Phi = \bar{\Phi}_i^n$, the weak-form is for given i and j, becomes,

$$\int_{z_1^n}^{z_2^n} \left(I_j^n \frac{1}{Y^n} \frac{d\bar{\Phi}_i^n}{d\bar{z}} \frac{d\bar{\Phi}_j^n}{d\bar{z}} + I_j^n \frac{1}{Y^n} \left[\alpha^n + \beta^n\right] \bar{\Phi}_i^n \frac{d\bar{\Phi}_j^n}{d\bar{z}} + \right.$$

$$\left. I_j^n \left[Z^n - \alpha^n C^n + C'^n\right] \bar{\Phi}_i^n \bar{\Phi}_j^n - \bar{\Phi}_i^n E_z^i \right) d\bar{z} - \left[-\bar{\Phi}_i^n V^n + C^n \bar{\Phi}_i^n \bar{\Phi}_j^n I_j^n\right]_0^l = 0. \ (45)$$

After expanding the boundary term, and performing the integration analytically, the weak-form over the nth element support can be written using matrix notation as,

$$\mathbf{Z}^n \mathbf{I}^n = \mathbf{g}^n + \mathbf{b}^n, \qquad (46)$$

where, $\mathbf{I}^n = [I_1^n, I_2^n]^T$ is the unknown node currents, $\mathbf{g}^n = [g_1^n, g_2^n]^T$ is the excitation vector, $\mathbf{b}^n = [b_1^n, b]^T$ is the boundary term, and $\mathbf{Z}^n$ is the nth element impedance matrix given by,

$$\mathbf{Z}^n = \frac{1}{lY^n} \begin{bmatrix} 1 & -1 \\ -1 & 1 \end{bmatrix} + \frac{1}{2Y^n} \left[\alpha^n + \beta^n\right] \begin{bmatrix} -1 & 1 \\ -1 & 1 \end{bmatrix}$$

$$+ \frac{l}{6} \left[Z^n - \alpha^n C^n + C'^n\right] \begin{bmatrix} 2 & 1 \\ 1 & 2 \end{bmatrix} - \begin{bmatrix} -C_1^n & 0 \\ 0 & C_2^n \end{bmatrix}. \qquad (47)$$

The elements of the excitation vector $\mathbf{g}$ are given by,

$$g_1^n = \frac{l}{2} E_{zn}^i, g_2^n = \frac{l}{2} E_{zn}^i. \qquad (48)$$

Finally, the elements of the boundary terms vector are given as,

$$b_1^n = V_1^n \text{ and } b_2^n = -V_2^n. \tag{49}$$

To assemble the global finite element impedance matrix $\mathbf{Z}_{FEM}$, i.e., connecting all elements, the following the boundary conditions must be enforced,

$$I_2^n = I_1^{n+1} = I_{n+1} \text{ (current continuity)},$$

$$-V_2^n + V_1^{n+1} = 0 \text{ (voltage continuity, no external voltage source is impressed}$$

$$\text{between the } n\text{th and the } (n+1) \text{ elements)},$$

$$I_1^1 = I_2^N = 0.$$

The voltage continuity calls for,

$$b_1 = b_1^1 \rightarrow Z_{11} = Z_{11}^1,$$

$$b_2 = b_2^1 + b_1^2 \rightarrow Z_{22} = Z_{11}^2 + Z_{22}^1,$$

$$\text{and so on, until,}$$

$$b_{N+1} = b_N^2 \rightarrow Z_{(N+1)(N+1)} = Z_{22}^N.$$

Thus, the global impedance matrix becomes,

$$\mathbf{Z}_{FEM} = \begin{bmatrix} Z_{11}^1 & Z_{12}^1 & 0 & \cdots & 0 \\ Z_{21}^1 & (Z_{22}^1 + Z_{11}^2) & Z_{12}^2 & 0 & \cdots \\ 0 & Z_{21}^2 & (Z_{22}^2 + Z_{11}^3) & Z_{12}^3 & \cdots \\ \vdots & 0 & Z_{21}^3 & \ddots & \ddots \\ 0 & \vdots & 0 & \ddots & Z_{22}^N \end{bmatrix}. \tag{50}$$

Using this matrix, the current over the scatterer is given by,

$$\mathbf{I} = \mathbf{Z}_{FEM}^{-1}(\mathbf{g}_{FEM} + \mathbf{b}). \tag{51}$$

where $\mathbf{I} = [I_1, I_2, \ldots, I_{N+1}]^T$ is the unknown current vector,

$$\begin{aligned} \mathbf{b} &= \left[b_1^1, b_2^1 + b_1^2, \ldots, b_2^{N-1} + b_1^N, b_2^N \right]^T \\ &= \left[V_1^1, 0, \ldots, 0, V_2^N \right]^T, \end{aligned} \tag{52}$$

is the voltage boundary vector, and,

$$\mathbf{g}_{FEM} = \left[g_1^1, g_2^1 + g_1^2, \ldots, g_2^{N-1} + g_1^N, g_2^N \right]^T. \tag{53}$$

The voltage (secondary variable) boundary conditions $V_1^{n+1} - V_2^n = 0$ is used since no external source is introduced over the nth element. It is not necessary to solve the 1st and last equations in this system since it is already known that $I(0) = I(L) = 0$. Thus, only the remaining $N - 1$ equations are needed. To solve for the voltage, one can use the obtained current directly into (29). In line with the observation made earlier about the wave equation, it is remarked that the obtained FEM matrix reduces to the conventional TL FEM matrix as well when the parameters α and β are set to zero.

The above FEM solution was validated by comparison to the MoM solution for different scattering and radiation scenarios. For example, Figure 2.6 shows the magnitude and phase of the current on a dipole antenna of length $L = \lambda$ and radius 0.001λ fed at $z = \lambda/4$ as obtained by solving Pocklington's IE with MoM and the MC model with FEM ($N = 400$). It is clear that both methods provided similar results.

The extracted MC parameters for the wire used in the above example are shown in Figure 2.7. Note that these parameters are distributed (as opposed to lumped) parameters.

The per-unit parameter $G(z)$ (real part of $Y(z)$) is shown to be very close to zero (with small numerical errors) since a PEC wire was considered. The per-unit radiation resistance $R(z)$ is around 280 Ω/m at the center of the wire, reduces to 130 Ω/m toward the ends and actually becomes zero at the open ends. The imaginary part of $Z(z)$ (per unit inductance) is shown to be much larger than the imaginary part of $Y(z)$ (per unit capacitance). This result is further confirmed by the well-known fact that wire antennas which are longer than the resonant length ($\lambda/2$) are
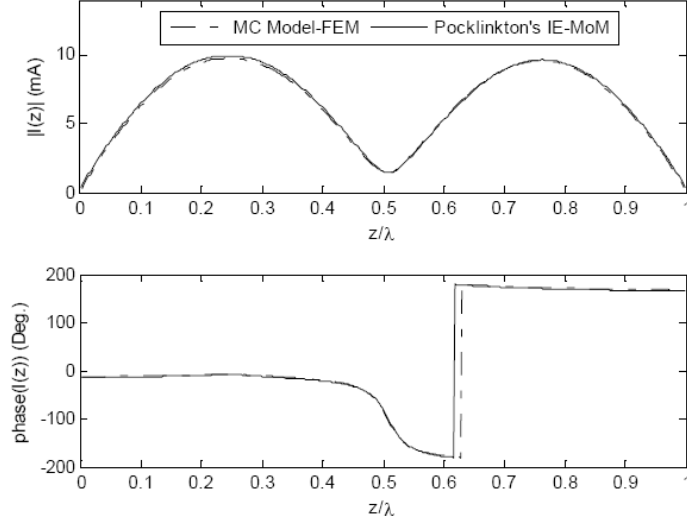
Figure 2.6. Magnitude and phase of the current distribution on a dipole antenna of length $L = \lambda$ and radius 0.001λ fed at $z = \lambda/4$.

inductive in general. Both $\alpha(z)$ and $\beta(z)$ go to zero at the center of the dipole and they reverse polarity toward the ends. The radiation is shown to be "initiated" at the wire ends (the dependent source factors α and β are large at the ends). Since the radiation resistance is zero at the open ends, no radiation takes place at that location (reactive energy is stored in that region). Around the center region, the wire may be regarded as a lossy transmission line (in this case, the loss comes from radiation). These observations are actually in-line with general theory of wire antennas. The only difference here is that these physical observations were made by examining simple equivalent circuit parameters.

2.2.4. MC Analysis of Loaded Antennas and Scatterers. The addition of the load has no bearing on the MC model parameter extraction. Furthermore, the FEM development is not changed except for the additional boundary condition on the voltage. The load boundary condition can be handled effectively as follows. Assuming the load is inserted between two elements, say the n_Lth and $(n_L + 1)$th elements, the voltage drop across the load is given as,

$$-V_2^{n_L} + V_1^{n_L+1} = v^e, \tag{54}$$
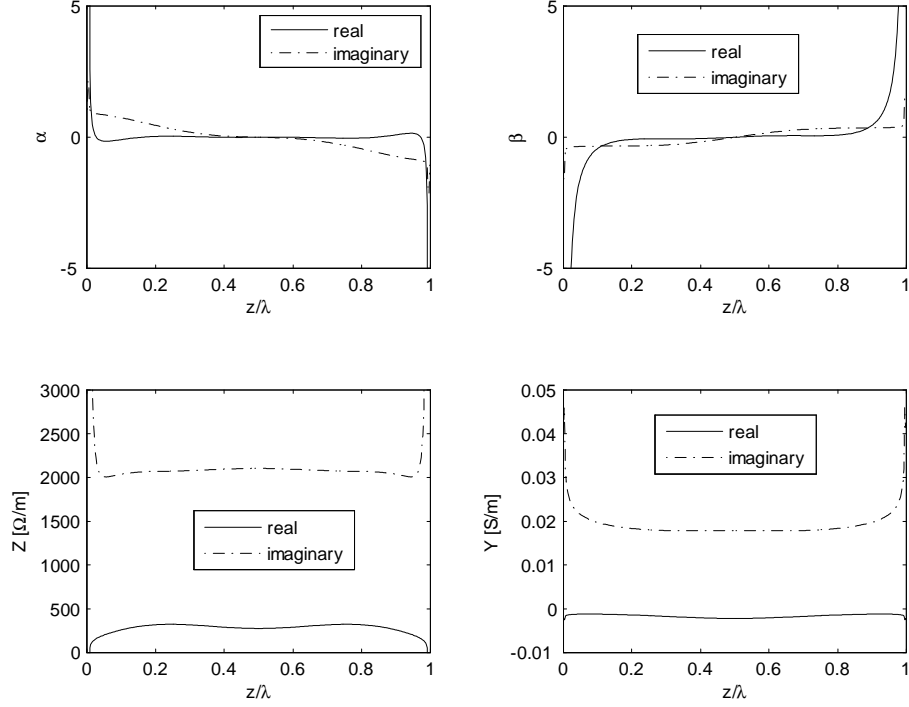
Figure 2.7. The MC parameters of λ-long wire of radius 0.001λ fed at $z = \lambda/4$.

where v^e is the load-equivalent voltage given in (24). The load boundary condition can be incorporated into the FEM solution of (51) by inserting the equivalent voltage v^e in the appropriate location (row) in the boundary vector $\mathbf{b}$. Multiple linear loads can be treated by following the same procedure after obtaining their equivalent voltages [40].

To demonstrate the validity of the MC approach, a loaded dipole antenna of length $L = \lambda$ and length-diameter ratio $L/2a = 74.2$ is considered here. The dipole is fed at $z = L/4$ and loaded at $z = L/2$ with the impedance, $Z_L = \infty$. Figure 2.8 shows the current distributions obtained using both methods. These results compare well to their counterparts in Fig. 9(b) of [35].

The backscattering RCS was also computed for a center-loaded wire scatterer of varying length and length-diameter ratio $L/2a = 74.2$ in response to a broadside plane wave illumination. Figure 2.9 shows the RCS for different loading cases. As
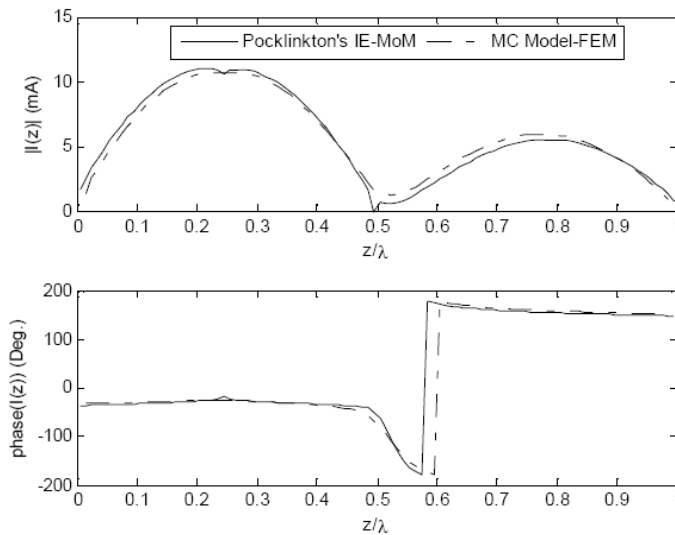
Figure 2.8. The current distribution on a dipole of length $L = \lambda$ and $L/2a = 74.2$ fed at $z = L/4$ and loaded at the center with $Z_L = \infty$.

shown in Figure 2.9, the results obtained using the MC model with the FEM solution are in good agreement with the results of the IE solution [35].

Since the MC models can be obtained for other type of wire antennas or scatterers, e.g., wire bends [38] and spiral antennas [39], the approach presented in here is applicable to such problems as well. It must be noted that the MC TL model, by itself, is not a problem solving method like the MoM (the MC parameters are extracted using the MoM). The MC model "repackages" or recasts the MoM solution using a simple RLC circuit model. Such circuit representation of wire antennas and scatterers may be easier to understand. Furthermore, the MC model can give better insight into wire antenna and scatterer behavior based on simple circuit calculations using the MC model parameters.

2.3. SUMMARY

Analyzing loaded wire antennas and scatterers was considered in this section. The well-established solution method based on Pocklington's integrodifferential equation and method-of-moments was presented. Based on the Maxwellian Circuit theory,
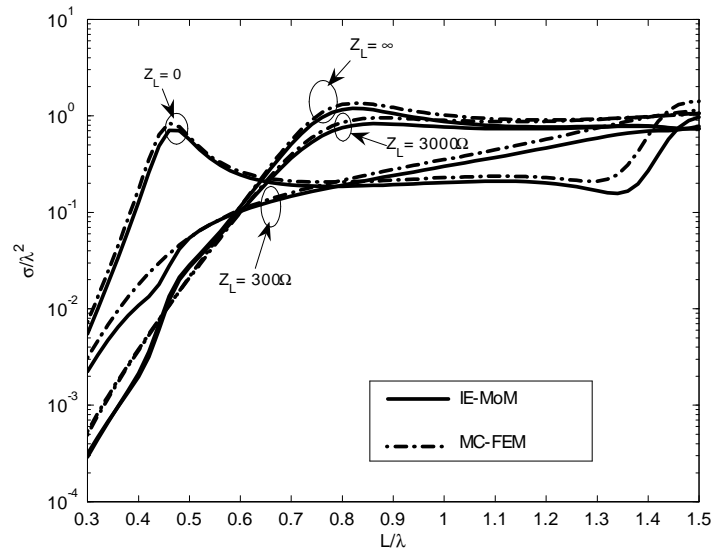
Figure 2.9. Backscattering RCS of wire scatterer loaded at the center with different loads.

a new method to analyze wire antennas and scatterers loaded with linear lumped elements was demonstrated. The Maxwellian circuit model was solved using the FEM whereby the load boundary condition is incorporated as an equivalent voltage source. It was shown that the developed method yields accurate results for both radiation and scattering scenarios. The analysis considered in this section laid the foundation needed to develop the multiple-loaded scatterer method (MLS) as it will be presented in the next section.

3. MULTIPLE LOADED SCATTERER METHOD

Measuring relative electric field spatial distributions at microwave and millimeter wave frequencies is of great importance for design verification, optimization and diagnosis purposes in a wide variety of applications including antenna design, electromagnetic compatibility (EMC), nondestructive testing (NDT) and imaging. Basically, a probe (a single antenna or array of antennas) sensitive to the electric field component of interest is used to measure the electric field in a specified spatial domain, i.e., mapping the field. A conventional probe used for this purpose is based on modulated scatterer technique (MST) which was first proposed in [28]. Since its introduction, the MST with scanned single modulated scatterer, i.e., loaded dipole, and array of scatterers, has been widely used for electric field mapping and imaging applications [14], [42]-[43].

Modulating the scatterer enhances measurement sensitivity, i.e., reduces the effect of unmodulated noise through coherent averaging over many modulation cycles. Furthermore, modulation allows for simple spatial signal multiplexing when an array of scatterers is used to map the electric field, and consequently a single receiver may be used rendering low overall system cost and complexity [14].

A new electric field distribution measurement method employing multiple loaded linear scatterer (MLS) instead of the conventional MST arrays has been recently introduced in [44] and [45]. The MLS method was conceived to overcome many of the practical limitations associated with the conventional MST, as will be described later. To this end, the MLS method utilizes a linear scatterer loaded with PIN diodes, at multiple discrete locations over its length, while placed in the field of interest. Using multiple loads allows for loading the scatterer structure with distinct modulation states, or *loading conditions.* As an intermediate step towards recovering the field of interest, the MLS method reconstructs the current distribution induced on the scatterer when all of its loads are short-circuited. This is founded on the fact that the scattered electric field from a loaded scatterer is the superposition of the field scattered when the load is short-circuited and the radiated field form the scatterer when it is fed at the load location with an equivalent load voltage as it was discussed in the previous section. The equivalent load voltage itself is a function of

the current passing through the load location when it is short-circuited as per (24). This short-circuit current, while related to the incident electric field of interest, is independent of the loading conditions . Hence, by measuring the scattered electric field at a single observation point under each loading condition, it is possible to form a system of linear equations which can be solved to give the current over the length of the scatterer when the loads are all short-circuited. This current is subsequently used to recover the electric field of interest.

Multiple and continuous loading of linear wire scatterers and antennas are well-established concepts used for antenna pattern synthesis [46], radar cross-section (RCS) control [47], and bandwidth extension purposes [48]. However, the utility of multiple loaded scatterer for the purpose of measuring unknown electric field distribution is yet to be fully investigated. The pertinent background on the conventional MST electric field measuring single probes and arrays is provided first. Then, the MLS method is presented and its unique aspects are compared to the conventional MST. Finally, the performance of the MLS method is demonstrated and compared to the conventional MST via numerical simulations.

3.1. THE MST PROBE

Typically, the single probe uses a short dipole scatterer loaded with a PIN diode. The spatial distribution of the electric field of interest is measured by scanning the probe in that field while switching the PIN diode between ON and OFF states. Modulation changes the scattering cross-section of the dipole and this in turn results in a modulated scattered field [28]-[29].

3.1.1. Basic Concept. To illustrate the basic idea behind the MST, consider Figure 2.2 and assume the task of measuring the electric field incident on the scatterer location due to the source. This can be accomplished by measuring the voltage across the source terminals, V_2, as follows.

The port currents and voltages are related by the open-circuit parameters as [36],

$$\begin{bmatrix} Z_{11} & Z_{12} \\ Z_{21} & Z_{22} \end{bmatrix} \begin{bmatrix} I_1 \\ I_2 \end{bmatrix} = \begin{bmatrix} V_1 \\ V_2 \end{bmatrix}, \tag{55}$$

where Z_{ii} and Z_{ij} are the self and transfer impedances, respectively. The load boundary condition is written as,

$$I_1 = -V_1/Z_L. \tag{56}$$

The total voltage across the source terminals can be related to the incident field at the dipole and the load impedance by solving (55) and (56) for V_2, that yields,

$$V_2 = Z_{11}I_2 - \frac{Z_{12}Z_{21}}{Z_{11} + Z_L}I_2. \tag{57}$$

For reciprocal media, the transfer impedances $Z_{12} = Z_{21}$ are given by [36],

$$Z_{12} = Z_{21} = -\frac{1}{I_2 I_1} \int_0^L E_z^i(z) I_1(z) dz. \tag{58}$$

When the dipole is small, i.e., $L << \lambda$, the current distribution over the dipole, $I_1(z)$, is approximately constant and equals to the port current I_1, that is $I_1(z) = I_1$. The incident electric field distribution is locally constant over the dipole in this case as well. Let $E_z^i(z) = E_z^i = |E_z^i| e^{j\phi_e}$ represents the local field of interest at the dipole location (with magnitude $|E_z^i|$ and phase ϕ_e). Using these approximations in (58) yields,

$$Z_{12} = Z_{21} = -\frac{LE_z^i}{I_2} \ (L << \lambda). \tag{59}$$

Using (59) in (57), the voltage across the source terminals is written in terms of the electric field of interest as [29],

$$\begin{aligned} V_2 &= Z_{11}I_2 - \frac{L^2}{I_2}\frac{(E_z^i)^2}{Z_{11} + Z_L} \\ &= V_o - K_o \frac{(E_z^i)^2}{Z_{11} + Z_L} \end{aligned} \tag{60}$$

Let's assume that the presence of the loaded dipole does not change (perturb) the current distribution over the source, e.g., the dipole is in the far-field of the source. In this case, the term $Z_{11}I_2 = V_o$ and $L^2/I_2 = K_o$ are constants, i.e., do not change as a function of the load impedance, Z_L. The total voltage as given in (60) has two terms; V_o which bears no information about the field of interest and a second term that is proportional to the square of the electric field incident on the dipole, $(E_z^i)^2$. Only

the second term is of interest here since it carries the information about the field of interest. In practice, these two terms are measured collectively as V_2. To differentiate between these two terms in the total measured voltage, the component of interest should be "tagged" in a way to allow isolation or extraction the relevant information from V_2 . To this end, the dipole is modulated by changing the value of loading impedance, Z_L, over time, and consequently modulating the component of interest only. Thereupon, extracting the information carried by the modulated component of V_2 can be accomplished using a detector that is sensitive to the modulated waveform, i.e., matched filter/lock-in amplifier [14].

Figure 3.1(a) illustrate the basic MST concept using loaded small dipole. The modulated responses in the time and frequency domains are depicted in Figure 3.1(a) as well. Figure 3.1(b) shows a typical measured magnitude and phase response, i.e., the reflection coefficient seen at the source terminals, Γ, from a PIN diode-loaded dipole scatterer of length $L = \lambda/4$ at 24 GHz.

(a)   (b)
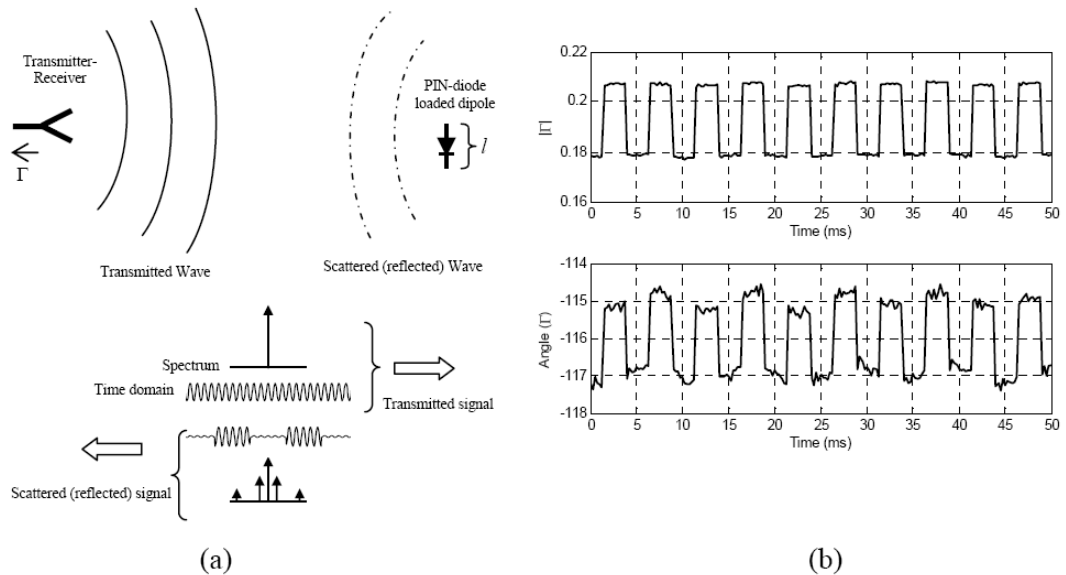
Figure 3.1. (a) MST concept in monostatic setup, and (b) actual modulated response measurement of PIN-loaded dipole scatterer of length $L = \lambda/4$, at 24 GHz.

3.1.2. Modulation Characteristics. So far, the time-dependence, $j\omega$, was implicit. Retaining the time-dependence in (60) gives,

$$
\begin{aligned}
V_2(t) &= \text{Re}\{V_o e^{-j\omega t}\} - \text{Re}\{K_o m_p(t)(E_z^i)^2 e^{-j\omega t}\} \\
&= |V_o| \cos\left(\omega t + \phi_{V_o} + \phi_o\right) \\
&\quad - |K_o| \left|E_z^i\right|^2 |m_p(t)| \cos\left(\omega t + \phi_{K_o} + 2\phi_e + \phi_{m_p}(t) + \phi_o\right)
\end{aligned}
\tag{61}
$$

where ω is the angular wave frequency, ϕ_{V_o} and ϕ_{K_o} are constant phase terms corresponding to V_o and K_o, respectively, ϕ_o is initial constant phase term, $m_p(t)$ is the "physical" modulating signal given by,

$$
m_p(t) = \left|\frac{1}{Z_{11} + Z_L(t)}\right| e^{j\phi_{m_p}(t)},
\tag{62}
$$

and $\phi_{m_p}(t)$ is a phase modulation term due to the temporal change in the phase of $1/(Z_{11} + Z_L(t))$.

When a PIN diode is used to load the dipole, modulation can be a achieved by turning the diode ON and OFF via the application of a dc voltage across its terminal. In the ON state (forward-biased), the diode represents a resistive load of small value $Z_L = R_f$, e.g., almost a short-circuit. In the OFF state (reverse-biased), the diode has a high capacitive impedance $Z_L = 1/j\omega C_r$, i.e., almost an open-circuit. The PIN diode voltage modulating signal, $m(t)$, is a sequence of pulses alternating between 0 (OFF state) and the voltage required to turn the diode ON, e.g., 1.45 V. The physical modulating sequence changes accordingly in response to the change in the PIN diode impedance as it switches between the ON and OFF states. Figure 3.2 shows typical PIN-diode modulating sequence (50% duty cycle) and the corresponding physical modulating signal for a quarter-wave long loaded dipole. Practical PIN diode load values, $R_f = 5\ \Omega$, and $C_r = 25$ fF [49], at 24 GHz were used to compute the results shown in Figure 3.2. Notice that the change in $|m_p(t)|$ and $\phi_{m_p}(t)$ in response to the PIN-diode modulating sequence is actually small. The change in $m_p(t)$ is related to the modulated signal power appearing at the output of the receiver. This power, which is related to how well the scatterer is being modulated, i.e., the modulation-depth, is the "useful" power corresponding to

the signal containing the information about the electric field of interest. The signal-to-noise ratio (SNR) at the receiver is then determined from this power. The SNR in turn determines the system sensitivity; i.e., higher SNR results in higher sensitivity. Sensitivity is defined here as the minimum detectable change in the measurement parameter of interest, i.e., the real and imaginary parts of the electric field.
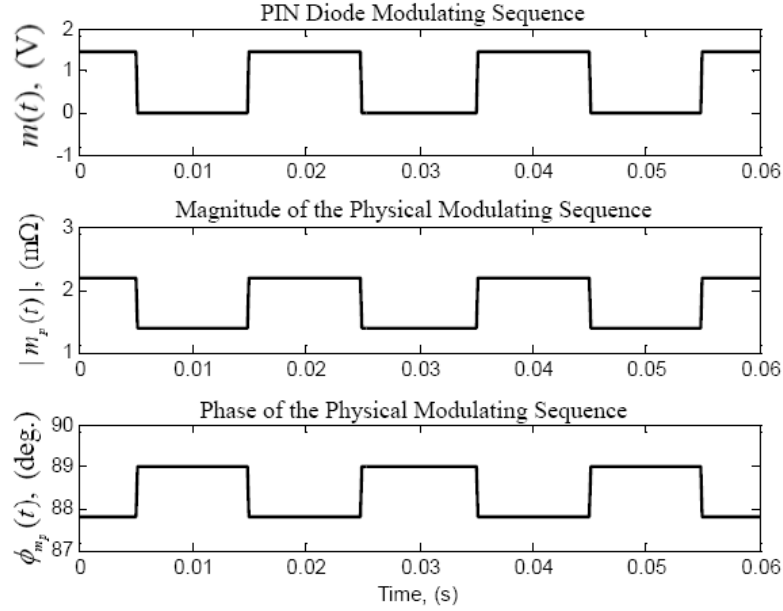
Figure 3.2. PIN-diode modulating sequence and magnitude and phase of the corresponding physical modulating signal for a quarter-wave long loaded dipole.

In the general MST case, the modulation is regarded as Complex or Vector Modulation since both magnitude and phase of the carrier signal are modulated as per (61). As shown Figure 3.2, for a $\lambda/4$ dipole, there is a small phase change in the term $\phi_{m_p}(t)$ due to modulating the impedance of the PIN diode. This is a typical behavior for relatively short scatterers, and hence, for such scatterers, the phase modulation term can be neglected, i.e., the modulation reduces to Amplitude Modulation (AM) scheme (double-sideband). The first term of (61), $|V_o| \cos\left(\omega t + \phi_{V_o} + \phi_o\right)$, is regarded as the *residual carrier*. The relative amplitude relationship between the carrier and the modulated signal component is generally referred to as the *modulation*

depth. In MST, the modulation depth is an indication of how well the signal incident on the scatterer is being modulated; high modulation depth means strong scatterer modulation and vice-versa.

The above development was focused on basic monostatic MST setups; the transmitting antenna is also used to receive the signal scattered from the loaded dipole. In this setup, as it was shown above, the modulated back-scattered signal component is proportional the square of the electric field incident on the dipole. Such non-linear dependency reduces the measurement system dynamic range, and consequently the monostatic setup is not preferred in imaging applications [14]. Instead, bistatic setups are implemented in most imaging systems [14]. In the bistatic case, separate transmitter and receiver antennas are used to illuminate the scene including the scatterer and receive the scattered signal, respectively. In this case, the received modulated signal is proportional to the electric field at the dipole location. The received signal in the bistatic setup follows the same general form of (61) where $(E_z^i)^2$ is replaced with E_z^i [14].

Although short dipoles were considered above to illustrate the general concept, MST can be applied with long scatterers as well. For example, longer scatterers can be used in imaging applications where the non-perturbing nature of probes is less important of an issue compared to obtaining higher sensitivity [14]. With long scatterers, the received modulated signal is proportional to the integral of the electric field over the scatterer length [14]. For imaging applications this is acceptable since the relative field distribution is of interest and probe calibration procedures are typically used [14].

When long (strong) scatterer, such as a resonant $\lambda/2$ dipole is used, higher level of modulation in both magnitude and phase of $m_p(t)$ is obtained (higher modulation depth). Higher measurement sensitivity may be achieved with resonant dipoles. Due to space and mutual coupling limitations however, using $\lambda/2$ dipoles might not be feasible in imaging arrays where the interspacing between the array elements, center-to-center, should be less than $\lambda/2$ for proper field sampling.

3.1.3. Sensitivity Analysis. Within the MST area, little work has been done to actually relate the "useful" signal power at the receiver to the magnitude and phase of the modulating signal. Most of the previous SNR and sensitivity related

analyses considered the signal to be amplitude-modulated only. As we showed above, this is not the general case. Here, a simple and general approach is developed to derive a meaningful expression for the SNR and consequently analyze the sensitivity of the MST probe. The sought expression should explicitly include the change in the characteristics of the loaded scatterer due to modulation.

In any given "static" MST measurement setup, e.g., without scanning, the total unmodulated residual carrier power is constant. The residual carrier might appear at the receiver due to different internal and external coupling factors such as direct transmitter-receiver propagation path, parasitic reflections, signal leakage in the high frequency receiver circuitry, etc. Not all of these factors were included explicitly in the above development (they are lumped together in the term V_0). The unmodulated residual carrier can be reduced to a large extent by coherent detection, e.g. , lock-in amplifier, at the receiver if and only if it does not saturate the front-end components in the receiver (more on this later). The residual carrier is eliminated simply by subtracting the voltages measured under the ON and OFF states. Ideally, the lock-in amplifier/matched filter works towards this end and provides averaging over many modulation cycles.

After the receiver subsystem is designed, the receiver noise floor remains fairly constant. As far as the modulated signal is concerned, the only remaining design parameter which affects the performance directly is the physical magnitude and phase modulation.

The difference in the voltages, v_d, measured at the receiver side due to the scatterer only when the PIN diode is turned ON and OFF is given by,

$$
\begin{aligned}
v_d &= V_{ON} - V_{OFF} \\
&= (E_z^i)^2 K_o \left(\frac{1}{Z_{11} + Z_{L,OFF}} - \frac{1}{Z_{11} + Z_{L,ON}} \right) + w_n \qquad (63) \\
&= \left(\frac{Z_{L,ON} + Z_{L,OFF}}{Z_{11} + Z_{L,OFF}} \right) K_o (E_z^i)^2 + w_n, \qquad (64)
\end{aligned}
$$

where $Z_{L,ON}$ and $Z_{L,OFF}$ are the PIN diode load impedance in the ON and OFF states, respectively, and w_n is a complex Gaussian noise with zero mean and standard deviation $\sigma/\sqrt{2}$ per dimension (representing the receiver effective root-mean-squared (RMS) noise value, or in other words, the noise floor of the receiver).

Using (64), the SNR is then defined as,

$$SNR \triangleq \frac{\text{Signal Power}}{\text{Noise Power}} = \frac{|E_z^i|^4 K_o^2}{\sigma^2} \left| \frac{Z_{L,ON} - Z_{L,OFF}}{Z_{11} + Z_{L,OFF}} \right|^2 \tag{65}$$

In measurements, there is limited, if any, control over the term $|E_z^i|^4$ since it is related to the magnitude of the field of interest. Also, the control over K_o^2 is limited. The important result here is that,

$$SNR \propto \rho = \left| \frac{Z_{L,ON} - Z_{L,OFF}}{Z_{11} + Z_{L,OFF}} \right|^2, \tag{66}$$

from which we can make the following observations:

- For the ideal PIN-diode case, $Z_{L,ON} = 0$ (short-circuit), $Z_{L,OFF} = \infty$ (open-circuit), and in the limit, the SNR becomes proportional to,

$$SNR \propto \lim_{Z_{L,OFF} \longrightarrow \infty} \left| \frac{Z_{L,ON} - Z_{L,OFF}}{Z_{11} + Z_{L,OFF}} \right|^2 = 1,$$

  and, hence, the SNR becomes independent of the scatterer loading.

- The SNR is proportional to the square of the difference between $Z_{L,ON}$ and $Z_{L,OFF}$. The SNR decreases rapidly as $Z_{L,ON} - Z_{L,OFF}$ decreases. The limiting case here is $Z_{L,ON} = Z_{L,OFF}$ for which the SNR goes to zero (no modulation).

- The SNR decreases as the magnitude of Z_{11} increases.

- The sensitivity in electric field measurements is scaled by the factor $\sqrt{\rho}$. In the monostatic setup, the parameter of interest in measurement is $(E_z^i)^2$. Changes in $(E_z^i)^2$ are scaled by $\sqrt{\rho}$.

The obtained expression in fact follows the general intuition that, in order to get a strong enough modulation and high sensitivity, the scattering characteristics of the loaded dipole should change appreciably in modulation. From the obtained relation, two fundamental limitations of the MST based on small dipoles can be highlighted:

- Since MST typically uses sub-resonant dipoles, $L < \lambda/2$, which have high capacitive input impedances, Z_{11}, the obtained SNR is very small. Furthermore, since practical PIN diodes have capacitive $Z_{L,OFF}$, the input impedance Z_{11} and $Z_{L,OFF}$ will add up toward even greater denominator for the scaling factor, ρ. This is low-freqeuncy limit, e.g., given a certain probe length, working at lower frequencies reduces the SNR and sensitivity because Z_{11} becomes larger.

- For high-frequencies, the PIN diode reverse-bias impedance $Z_{L,OFF} = 1/j\omega C_r$ becomes relatively small (C_r is in the range of tens of femto-Farads for state-of-the-art PIN diodes [49]). In the limit, the SNR will become proportional to $|Z_{L,ON}/Z_{11}|^2$. Given that $Z_{L,ON}$ is small for practical PIN diodes (ideally zero), the SNR approaches zero in the limit (no modulation). This is a high-frequency limit on the MST method.

As an example, consider a $\lambda/4$ dipole center-loaded with a practical PIN diode at 24 GHz as before. With dipole input impedance being $Z_{11} \simeq 12 - j453\Omega$, $Z_{L,ON} = 5\Omega$, and $Z_{L,OFF} = -j265$, the SNR becomes proportional to,

$$SNR \propto \left| \frac{5 + j265}{12 - j453 - j265} \right|^2 \simeq 0.13.$$

By using $\lambda/4$ dipole at 2.4 GHz while keeping the same PIN diode load, the SNR becomes proportional to 0.73 ($Z_{L,OFF}$ increased by a factor of ten). Lowering the frequency to 2.4 GHz translates in this case to 7.5 dB gain in SNR (the signal level is five times higher).

Compared to the $\lambda/4$ dipole, a gain of around 9 dB in SNR can be achieved with $\lambda/2$ dipole at 24 GHz (the signal level is almost ten times higher). The proportionality factor approaches 1 for the resonant $\lambda/2$ dipole and decreases after that for longer dipoles. These estimates match well with the measurements. For example consider spectrum measurement results of the modulated signals received from $\lambda/4$ and $\lambda/2$ dipoles loaded with PIN diode in identical MST bistatic setups at 24 GHz (the PIN diode is similar to the one considered in simulations). Figure 3.3 shows the spectrum (normalized to the carrier power) of the signal measured at the receiver while modulating the $\lambda/4$ dipole with a modulating frequency $f_m = 20$ kHz ($f_c = 24$

GHz). As shown in Figure 3.3, the modulated signal component due to the scatterer is 50 dB below the carrier (the carrier power was around -50 dBm). The noise floor of the measurement system was around -120 dBm (70 dB below the carrier in this case).
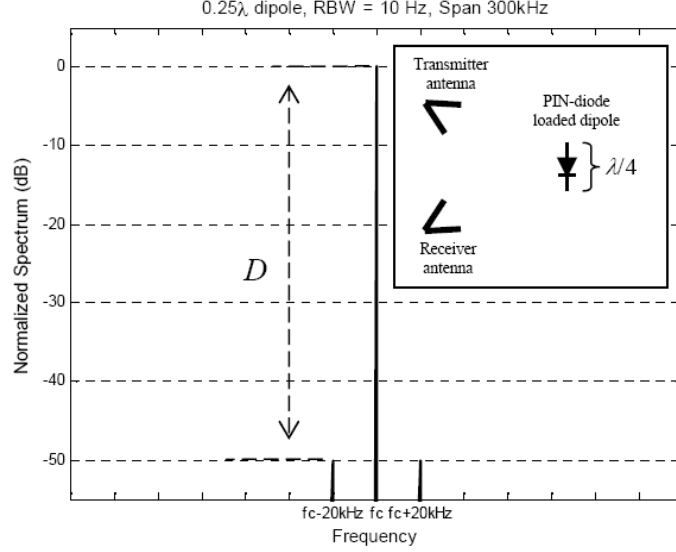
Figure 3.3. Measured normalized spectrum of the received signal in bistatic MST setup using a $\lambda/4$ modulated dipole, $f_c = 24$ GHz.

The modulation depth can be calculated from the spectrum analyzer measurements using [50],

$$\text{Modulation Depth} = 200 \times 10^{-D/20} \ (\%) \tag{67}$$

where D is the absolute difference in the measured power (in dB) between the carrier and the fundamental harmonic in one of the sidebands as indicated in Figure 3.3. The value of D is generally expressed in dBc (dB below carrier). The modulation depth can reach up to 100%. Theoretically speaking, the modulation depth can exceed 100%. Such case, however, has not been encountered in direct antenna/scatterer modulation. Using this relation, the modulation depth resulting from modulating the $\lambda/4$ dipole is around 0.63% only.

Using the $\lambda/2$ dipole increases the modulated signal level by almost 9 dB as shown Figure 3.4 (the modulated signal level increases from 50 dB to around 41 dB below the carrier). Consequently, the modulation depth becomes ~1.8% for the $\lambda/2$ dipole. These results are in-line with the theoretical analysis presented above. In both cases considered in measurements, the dipoles were at equal distances from the transmitter and receiver, i.e., around 6 cm.
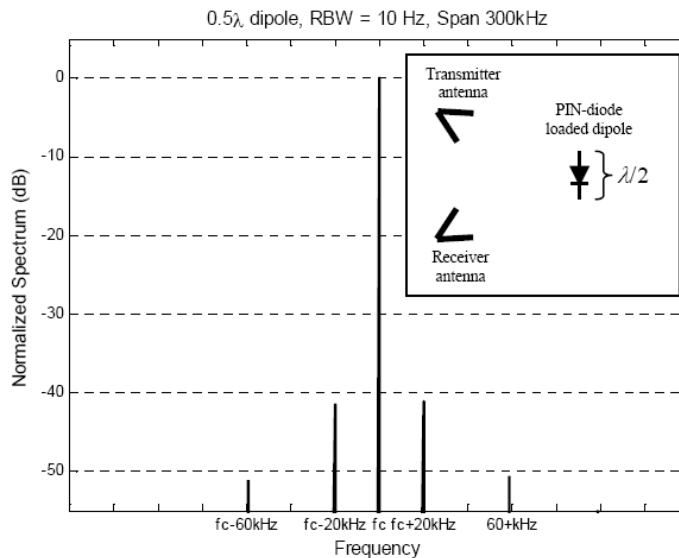
Figure 3.4. Measured normalized spectrum of the received signal in bistatic MST setup using a $\lambda/2$ modulated dipole, $f_c = 24$ GHz.

3.1.4. Practical Limitations. The spectrum measurement results shown above clearly highlight a major practical limitation of the MST using short loaded dipoles; namely very low modulation depth. Not only the modulated signal level is very small (-100 dBm with $\lambda/4$ dipole), the received signal in most cases is dominated by the residual carrier. To detect the modulated signal using custom made receivers, the signal has to be amplified at the receiver front-end such that the modulated signal level (the "useful" power) is increased to an adequate level for reliable detection, say the middle of the receiver's linear dynamic range. By reliable detection it is meant a

coherent detection which yields accurate phase and magnitude measurements. This can be accomplished using direct-conversion (IQ/homodyne) or heterodyne receivers.

With most homodyne and heterodyne receivers, detecting the modulated signal reliably requires very high gain/amplification in the receiver front-end and subsequent stages. Since amplification is applied to the composite signal (not the modulated signal alone), the carrier signal gets amplified with the same factor as well, and subsequently reaches a level where it actually saturates the receiver components (front-end and beyond). When the front-end is saturated, undesirable signal harmonics are generated (the signal becomes distorted) and passed through to the next stage of the receiver, i.e., lock-in amplifier. Consequently, these harmonics will degrade the detection of the modulated signal of interest. This is a major difficultly with MST imaging systems especially with direct-conversion (IQ/homodyne) receivers as discussed in [14]. The problem becomes compounded in imaging arrays since the presence of other array structures increase the carrier level. To avoid the residual carrier problem with direct-conversion receivers, the carrier signal must be suppressed before the front-end amplification stage using tuned-signal cancellation procedures [14]. These procedures need to be reapplied whenever the measurement setup changes. The need for such routine tuning largely undermines the robustness of the conventional MST-based imaging arrays. Heterodyne receivers (with one or multiple IF stages) may be used, in lieu of a direct-conversion receiver, to partially solve the residual carrier problem (provided that proper IF filters and amplifiers are implemented). Even with such a sophisticated and expensive receiver, the carrier might still saturate the IF amplifiers.

Finally, with receivers built to work at frequencies in or near the millimeter wave range, the residual carrier coupling in the receiver circuitry can be relatively high compared to the case of receivers designed to work at lower frequencies (shielding and signal decoupling techniques are easier and more effective at lower frequencies). Thus, the residual carrier problem imposes further practical limitations on the application of the MST for imaging systems intended to work at frequencies in or near the millimeter wave range.

To realize high sensitivity MST-based electric field measuring systems, more efficient loaded scatterers should be designed and used such that the resultant modulation depth in their signals is increased beyond the depth obtained with short dipoles. This is one of the primary objectives of this research. To achieve that; the multiple loaded scatterer (MLS) method (presented later in this section) and the loaded elliptical slot (Section 4) are introduced. Before describing the MLS method, a brief overview of the conventional MST arrays based on dipoles is given next.

3.2. MST ARRAYS

With a single scatterer, it takes a long time to complete the electric field distribution mapping process, which is undesirable in many applications where real-/pseudo-real time mapping is desired. To speed up this process, one- or two-dimensional arrays of small loaded scatterers may be used [14]. In most applications, a compact array of closely-spaced scatterers is needed in order to construct a representative map of the field of interest. In this configuration, the interaction between the array elements not only limits the system sensitivity and dynamic range, but it must also be compensated for in order to obtain an accurate and representative field distribution (see [51] and the references therein). As stated earlier, MST can be applied in monostatic or bistatic configurations depending on the application requirements. The development in this work is focused on the general bistatic configuration.

A typical MST-based bistatic electric field measurement setup using a 1D array of PIN diode-loaded diploes each of length l is depicted in Figure 3.5. The loaded dipoles are interspaced by d_z and the total length of the array is L. The array is used to measure an unknown incident electric field, $E_z^i(z)$, radiated by a source under test, by measuring the scattered field, $E_z^s(Q)$, at a point $Q(x, y, z)$, while modulating the dipoles. Modulation is performed by turning a single given PIN diode ON and OFF while all remaining diodes are turned OFF. This process is repeated for all diodes sequentially (parallel modulation using orthogonal codes is also possible in some cases). Ideally, the ON and OFF states of the PIN diode approximate open- and short-circuit loads, respectively. When the dipole length, l, is small relative to the wavelength, λ, the scattered field from the shorted-dipole is proportional to the incident field at the dipole location. Hence, modulation allows for

tagging the scattered field as a function of the location of the modulated dipole while the measurements are taken at a single receiving point, i.e., one receiver is needed. The dipole interspacing, d_z, should be at most $\lambda/2$ in order to achieve proper sampling of the incident field [14]. Applying the MST involves calibrating the system, e.g., the array and receiver, with a known field distribution such as a uniform plane-wave [14].
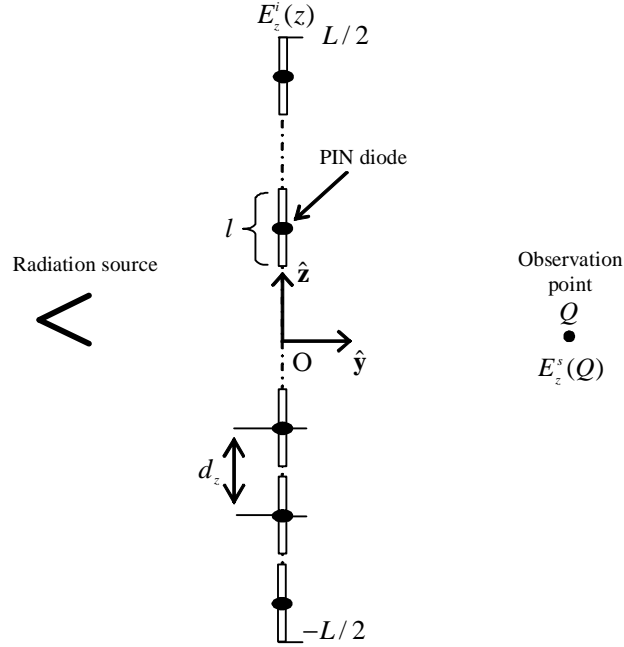
Figure 3.5. Typical MST bistatic electric field measurement configuration using a 1D array of PIN diode-loaded short dipoles.

Aside from the fundamental limitations of the single MST probe as mentioned earlier, the performance of the MST-based arrays when used for electric field distribution measurement depends on many factors. As stated in [51]; "Six basic factors that can have an impact on measurement system performances are as follows: 1) dynamic range, 2) interelement mutual coupling, 3) interaction between the MST array and test antenna, 4) parasitic signals (modulated and/or unmodulated), 5) dispersion of element scattering characteristics, and 6) probe correction." These factors impose many trade-off considerations that need to be resolved on per-application basis. For

instance, the interelement mutual coupling combined with the fact that the utilized elements are commonly small scatterers, i.e., short dipoles, can adversely impact the system sensitivity, and hence reduce the overall system dynamic range. On the other hand, using stronger scatterers, e.g., resonant scatterers as suggested in [52], can enhance the sensitivity when effective probe correction and compensation techniques are employed. Such a trade-off was investigated in [53] where it was articulated that "For practical reasons, instead of trying to build noninterfering (and therefore more complicated and perhaps less sensitive) sensors, one can use common sensors (simpler, inexpensive, and possibly more sensitive) and include them in the reconstruction formulism itself."

At high frequencies such as those in or near the millimeter wave region, the implementation of conventional MST-based systems, using an array of dipoles, becomes more challenging due the factors mentioned above. At these frequencies, the factors pertaining to parasitic loads which are difficult to characterize, and element dispersion become a significant issue in the system design. Furthermore, the measured response of the weakly modulated array dipole to small variations in the incident field is likely to be masked by the signals arising from the interaction among the array dipoles (these are modulated signals). The multiple loaded scatterer (MLS) method presented next is expected to effectively overcome most of the abovementioned issues and challenges.

3.3. MULTIPLE LOADED SCATTERER (MLS) METHOD

The current induced on a linear wire scatterer of length L and radius a aligned with the z-axis due to an incident electric field, $E_z^i(z)$, can be found using Pocklington's integral equation using the Method-of-Moment (MoM) as it was outlined in the previous section. The induced current solution is given by,

$$\mathbf{I}^{sc} = \mathbf{Y}\mathbf{e}, \tag{68}$$

where $\mathbf{I}^{sc}$ is the "short-circuit" current induced on the scatterer as given by (25), $\mathbf{Y} = \mathbf{Z}^{-1}$ is the scatterer admittance matrix obtained after applying the MoM, $\mathbf{e}$ is

the excitation vector as given by (17), k is the wavenumber, and η is the intrinsic impedance of the medium as defined in the previous section.

The z-component of the scattered electric field can be written as,

$$E_z^s(x, y, z) = \frac{-j\eta l_s}{4\pi k}\mathbf{g}\mathbf{I}^{sc},\tag{69}$$

where $\mathbf{g} = [G(z_1),\, G(z_2),\, \ldots,\, G(z_N)]$ such that,

$$G(z_i) = [G_1(z_i) + (z - z_i)^2 G_2(z_i)]e^{-jk\sqrt{x^2+y^2+(z-z_i)^2}}.\tag{70}$$

The functions $G_1(z)$ and $G_2(z)$ are given in [31, pp. 284].

The MLS method is based on using a single linear scatterer loaded with M controllable loads, e.g., lumped active elements such as PIN diodes, with general admittances of $\{Y_m : m = 1, 2, \ldots, M\}$, located at $\{z_{Lm} : m = 1,\, 2,\, \ldots,\, M\}$, as shown in Figure 3.6. The scatterer is illuminated by an unknown incident field, $E_z^i(z)$, produced by a radiation source. The objective is to measure the incident electric field distribution, $E_z^i(z)$, over the length of the the scatterer using the measured scattered field, $E_z^s(Q)$, obtained at an arbitrary observation point, Q. The development of the MLS method starts with explicitly expressing the scattered electric field in terms of the load admittances, as outlined next.

The general analysis of straight wire scatterers loaded with lumped linear elements was considered in Section 1. An equivalent approach based on Maxwellian Circuits theory was also developed [40]. The MLS considered here can be analyzed by finding the current induced along its length using linear network theory whereby the scatterer can be treated as a $(M + 1)$-port network (M load terminals plus the illuminating source terminals). In this treatment, each load is represented by an equivalent voltage source at its location along the scatterer. An expression for the load equivalent voltages can be obtained from the short-circuit parameters relating the port currents and voltages in addition to the load boundary conditions. The port currents and voltages are related by,

$$\mathbf{I} = \mathbf{Y}_t\mathbf{V},\tag{71}$$
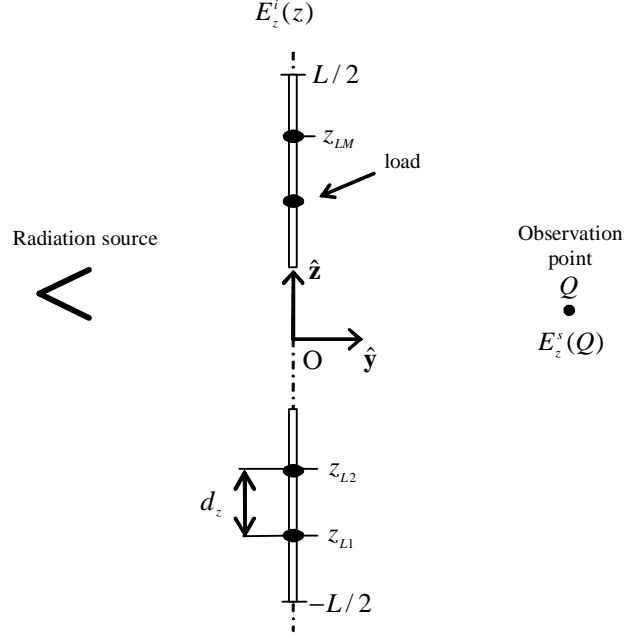
Figure 3.6. MLS-based electric field distribution measurement configuration.

where $\mathbf{Y}_t$ is the transfer admittance matrix of size $(M+1) \times (M+1)$, $\mathbf{I} = [\ I_1,\ I_2,$ $\ldots,\ I_{M+1}]^T$ and $\mathbf{V} = [V_1,\ V_2,\ \ldots,\ V_{M+1}]^T$ are the port current and voltage vectors, respectively. Here, the voltage across the source terminals is represented by V_{M+1}. The load conditions on the port voltages are,

$$I_m = -Y_m V_m, m = 1, 2, ..., M. \tag{72}$$

Solving (71) and (72) for the load equivalent voltages yields,

$$v^e_{Loads} = -\left[\mathbf{Y}_s + \mathbf{Y}_L\right]^{-1} \mathbf{I}^{sc}_{loads}, \tag{73}$$

where,

$$\mathbf{v}^e_{Loads} \quad = \quad [v^e_1,\ v^e_2, \ldots, v^e_M]^T \text{ , and} \tag{74}$$

$$\mathbf{I}^{sc}_{Loads} \quad = \quad [I^{sc}(z_{L1}), I^{sc}(z_{L2}), \ldots,\ I^{sc}(z_{LM})]^T , \tag{75}$$

are the load-equivalent voltage and short-circuit current vectors, respectively, $\mathbf{Y}_L = diag\{Y_1, Y_2, \ldots, Y_M\}$ is the load matrix, and $\mathbf{Y}_s$ is the transfer admittance matrix of size $M \times M$ defined between the load ports. Note that $\mathbf{I}^{sc}_{Loads}$ represents samples of $\mathbf{I}^{sc}$ taken at the load locations.

The total current along the scatterer is the superposition of the short-circuit current induced when all loads are short-circuited, as given in (68), and the current induced due to the equivalent load voltages as it was explained for a single load in the previous section. Let v^e be a vector of dimension $N \times 1$ with all zeros except at the M load locations where it is populated with the corresponding elements of v^e_{Loads}, then the solution for the total current can be found from (26) which is repeated here as,

$$\mathbf{I} = \mathbf{I}^{sc} + \left(\frac{-4\pi jk}{\eta l_s} \right) \mathbf{Y}\mathbf{v}^e. \tag{76}$$

It is remarked here that an equivalent solution for the current over the multiple-loaded scatterer can be obtained using the Maxwellian Circuit (MC) model developed in the previous section. In this case, using (51), the total current is given by,

$$\mathbf{I} = \mathbf{Z}_{FEM}^{-1}(\mathbf{g}_{FEM} + \mathbf{v}^e). \tag{77}$$

where $\mathbf{Z}_{FEM}$ and $\mathbf{g}_{FEM}$ are the global Finite-Element impedance matrix and the excitation vector, respectively. $\mathbf{Z}_{FEM}$ and $\mathbf{g}_{FEM}$ can be computed using the procedure outlined in the previous section while considering the short-circuited MLS described here, i.e., length and number of segments.

Using (76), the total scattered field at point Q is now given by,

$$E_z^s(Q) = \frac{-j\eta l_s}{4\pi k}\mathbf{g}\mathbf{I}^{sc} - \mathbf{g}\mathbf{Y}\mathbf{v}^e. \tag{78}$$

Note that the first term in (78), i.e., the scattered field when all ports are short-circuited, is not a function of the load matrix, $\mathbf{Y}_L$. This fact will be used later in the MLS formulation.

The premise of the MLS method is based on the ability to obtain the short-circuit current, $\mathbf{I}^{sc}$, induced along the scatterer by using different sets of load values

$\{Y_1, Y_2, \ldots, Y_M\}$, e.g., realizing different loading conditions, and measuring the scattered field under each loading condition at the observation point, Q. Given this current, the field of interest, $E_z^i(z)$, can be uniquely determined from (68). For this purpose, P distinct loading conditions are realized by electronically changing the load values such that the pth loading condition corresponds to a unique load matrix denoted by $\mathbf{Y}_L^p$, and results in load voltage vectors $\mathbf{v}_{Loads}^{ep}$ and $\mathbf{v}^{ep}$ (evaluated from (73) using $\mathbf{Y}_L^p$ in lieu of $\mathbf{Y}_L$). Let's designate one of the loading conditions as the *reference condition*, for example the 1st loading condition ($p = 0$). Under this condition, let the measured field be $E_z^{s0}(Q)$. Using (78), the difference between the field scattered due to the reference and the pth loading conditions is written as,

$$
\begin{aligned}
\delta^p &= E_z^{sp}(Q) - E_z^{s0}(Q) \\
&= \mathbf{gY}\left[\mathbf{v}^{e0} - \mathbf{v}^{ep}\right], \ p = 1, 2, ..., P-1.
\end{aligned}
\tag{79}
$$

Since the vectors $\mathbf{v}^{e0}$ and $\mathbf{v}^{ep}$ and have non-zero components only at the load locations, the corresponding M positions only in the $1 \times N$ vector $\mathbf{gY}$ contribute to δ^p. Define a $1 \times M$ vector $\mathbf{b}$ which is populated with these components. The field difference in (79) can now be written as,

$$
\begin{aligned}
\delta^p &= \mathbf{b}\left[\mathbf{v}_{loads}^{e0} - \mathbf{v}_{loads}^{ep}\right] \\
&= \mathbf{b}\left(\left[\mathbf{Y}_s + \mathbf{Y}_L^p\right]^{-1} - \left[\mathbf{Y}_s + \mathbf{Y}_L^0\right]^{-1}\right)\mathbf{I}_{loads}^{sc}.
\end{aligned}
\tag{80}
$$

Given the scatterer geometry, frequency of operation, and the load values for the different loading conditions, the above equation has everything known except the load short-circuit current vector which represents the M unknown loads short-circuit currents. To solve for this current, M equations are formed using $P = M + 1$ loading conditions. Thus, by measuring the scattered field for all loading conditions and using the first loading condition as the reference, the load short-circuit current vector is determined as,

$$
\mathbf{I}_{loads}^{sc} = \mathbf{W}^{-1}\boldsymbol{\Delta},
\tag{81}
$$

where,

$$\mathbf{\Delta} = \left[\delta^1, \delta^2, \ldots, \delta^M\right]^T, \tag{82}$$

is the vector of scattered field differences, and,

$$\mathbf{W} = \left[w^1; \ w^2; \ldots; \ w^M\right], \tag{83}$$

such that,

$$w^p = \mathbf{b}\left(\left[\mathbf{Y}_s + \mathbf{Y}_L^p\right]^{-1} - \left[\mathbf{Y}_s + \mathbf{Y}_L^0\right]^{-1}\right), \ p = 1, 2, \ldots, M. \tag{84}$$

The loading conditions should result in linearly independent current distributions over the length of the scatterer in order to uniquely determine $\mathbf{I}_{loads}^{sc}$, as per (81). Simulation results have shown that $\mathbf{W}$ is always of rank M, i.e., full rank, when such current distributions are realized. As it will be shown later, PIN diode loads are used to obtain the required loading conditions.

Before the incident electric field can be recovered using the computed short-circuit current, this current must be interpolated over the length of the scatterer, e.g., approximating $\mathbf{I}^{sc}$. Let $\tilde{\mathbf{I}}^{sc}$ be the interpolated short-circuit current obtained from $\mathbf{I}_{loads}^{sc}$. When there are no loads placed close to the ends of the scatterer, the boundary conditions, i.e., vanishing current at both ends of the scatterer in this case, can be enforced to obtain a better estimate of the short-circuit current. The incident electric field over the length of the scatterer is found as,

$$\hat{\mathbf{E}}_z^i = (j\eta/4\pi k)\mathbf{Z}\tilde{\mathbf{I}}^{sc}. \tag{85}$$

The functional procedure of the MLS method can now be summarized as follows,

1. activate the reference loading condition and measure $E_z^{s0}(Q)$,

2. activate the rest of the loading conditions and measure $E_z^{sp}(Q)$, $p = 1, 2, \ldots, M$,

3. from the obtained measurements, compute the field difference vector $\mathbf{\Delta}$ (off-line),

4. compute $\mathbf{W}$ (no measurement is required),

5. solve for $\mathbf{I}^{sc}_{loads}$ and interpolate it,

6. finally, solve for the incident electric field using (85).

The salient feature of the MLS method is the inherent differential field measurements, i.e., subtracting reference measurement from all subsequent measurements, which are used to construct the incident electric field. With this feature, the effects of clutter and distributed parasitics are significantly reduced. Unintentional parasitics and other "static" loads needed for biasing, such as decoupling capacitors, do not change with modulation and they result in a constant term being added to (78). Since the MLS method is not based on discrete elements, the limiting factors associated with conventional MST which are related to array element dispersion and interelement coupling do not limit its performance. Furthermore, the modulated scattered signal level in the MLS implementation, which is based on modulating a strong scatterer, is expected to be much higher than that in the conventional MST case. In practice, this fact translates to higher measurement sensitivity. This point can be illustrated by spectrum measurements. Consider modulating a $\lambda/4$ dipole loaded with PIN diode and an MLS of length λ loaded with four PIN diodes in a bistatic experiment performed at $f_c = 3$ GHz . The dipole and MLS were both modulated with pulse sequence of freqeuncy $f_m = 20$ kHz and placed 30 cm (12 in) from the transmitting antenna. The MLS was modulated by turning all diodes ON and OFF in response to the modulating sequence. The measured spectrum of the received signal normalized to the carrier power with the $\lambda/4$ dipole is shown in Figure 3.7. As indicated by the measurements shown in Figure 3.7, the modulated signal is totally masked by the receiver noise when the dipole is placed 30 cm from the transmitter (the modulated signal will show-up in the measured spectrum if the dipole is placed closer to the transmitter).

The normalized spectrum of the received modulated signal from the MLS is shown in Figure 3.8. By comparing Figure 3.7 to the MLS response shown in Figure 3.8, it becomes evident that the modulated MLS signal is much stronger compared to that of the $\lambda/4$ dipole. It is also interesting to notice that, with the MLS, the modulated signal is only around 23 dB below the carrier (dBc), i.e., modulation depth of 14.2% . Consequently, amplifying the signal is not as problematic as in the short

dipole case (in which the carrier might saturate the front-end as discussed before). With the MLS, the modulated signal harmonics are high rendering effective matched filter/lock-in amplifier detection (these schemes collects the signal power from these harmonics, and consequently, increase the SNR at the output of the receiver).
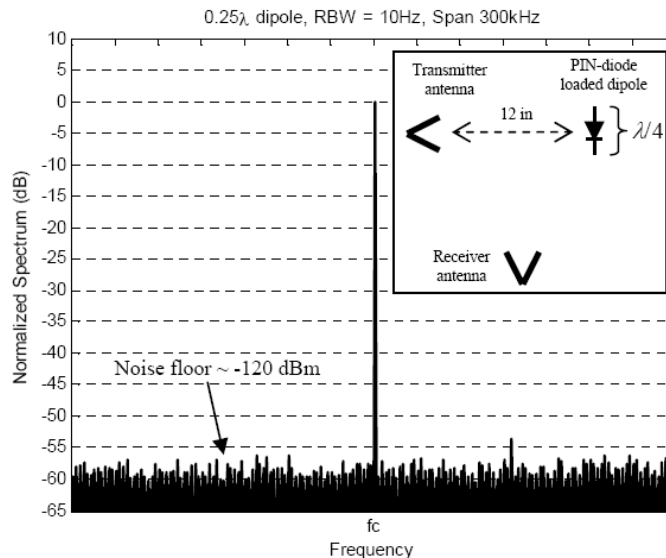
Figure 3.7. Measured normalized spectrum of the received signal in bistatic MST setup using a $\lambda/4$ modulated dipole placed 30 cm (12 in) from the transmitting antenna, $f_c = 3$ GHz.

Finally, no probe correction is needed with the MLS method since the presence of the scatterer is accounted for in recovering the incident field. Various attributes of the MLS method will be examined further in the following.

3.4. NUMERICAL RESULTS AND DISCUSSION

A linear wire scatterer representing an MLS of radius 0.001λ was considered to illustrate the method. Uniformly interspaced ideal PIN diodes were used to load the MLS, as shown in Figure 3.6. With M PIN diodes, there are 2^M different possible loading conditions. The $(M + 1)$ loading conditions needed in the MLS method are
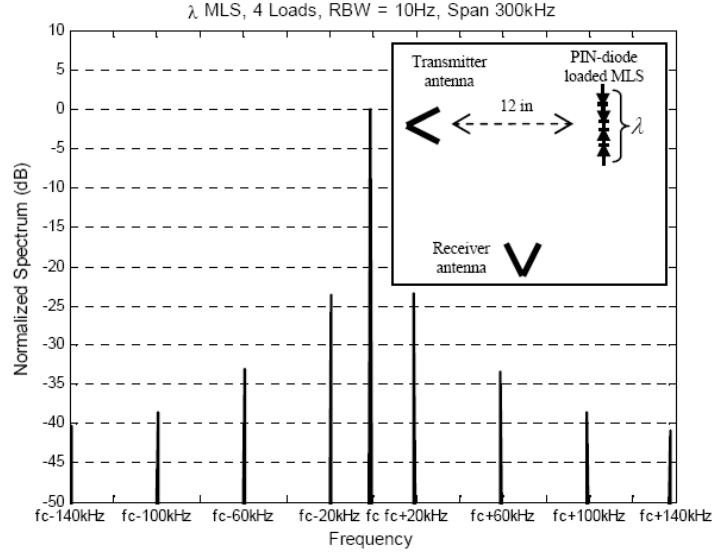
Figure 3.8. Measured normalized spectrum of the received signal from a modulated λ long MLS loaded with 4 PIN diodes placed 30 cm (12 in) from the transmitting antenna, $f_c = 3$ GHz.

a subset of the total possible loading conditions and should result in linearly independent current distributions over the length of the scatterer. The loading condition which consists of all diodes being turned ON is always used as the reference condition. Turning one diode OFF at a time while the rest are ON represents the remaining M loading conditions. This set of loading conditions was verified to meet the requirement mentioned above. For example, consider an MLS with $L = \lambda$ which is loaded with $M = 3$ PIN diodes. Figure 3.9 shows the magnitude and phase of the current induced on the MLS due to an incident uniform plane-wave for the selected 4 loading conditions. Namely; all diodes are ON, only the first diode is turned OFF, only the second diode is turned OFF, and only the third diode is turned OFF. The current distributions shown in Figure 3.9 are linearly independent and the matrix $\mathbf{W}$ is of rank 3.

When the loading conditions result in linearly dependent current distributions, the matrix $\mathbf{W}$ becomes rank-deficient. For instance, let's replace the third loading condition from the selected set, i.e., only the third diode is turned OFF, with the
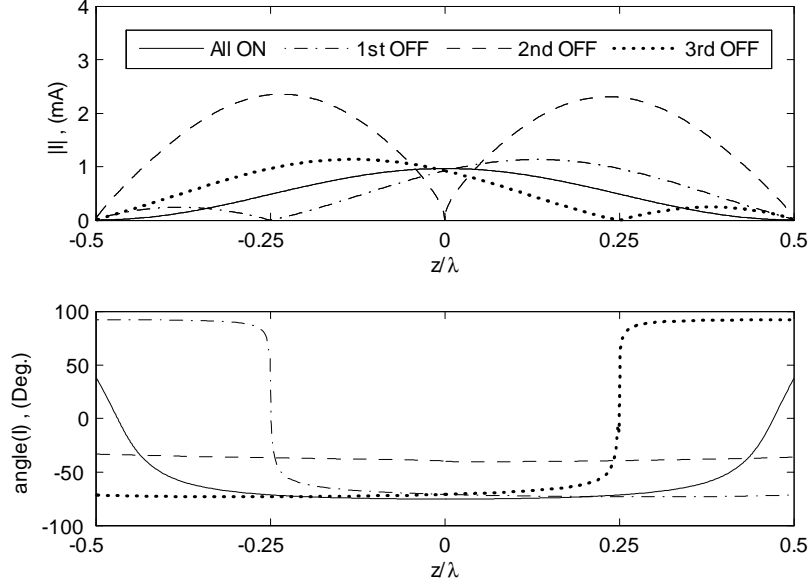
Figure 3.9. Magnitude and phase of the current induced on the MLS ($L = \lambda$, $M = 3$) due to an incident uniform plane-wave for the selected 4 loading conditions.

condition where the first and second diodes are turned OFF at the same time while the third diode is turned ON. Figure 3.10 shows the magnitude and phase of the current induced on the MLS for the new set of loading conditions. In this case, the obtained current distributions are linearly dependent (cf. the current distributions in the interval $[-0.5\lambda, -0.25\lambda]$ in Figure 3.10) and the matrix $\mathbf{W}$ is now of rank 2, i.e., it can not be used to determine $\mathbf{I}^{sc}_{loads}$ uniquely.

3.4.1. Short-Circuit Current Estimation. The procedure outlined above using an MLS of length 5λ and $M = 20$ PIN diodes was used to solve for the short-circuit current induced on the scatterer due to an incident uniform plane-wave while the scattered electric field observations were made $Q(0, 100\lambda, 0)$. Figure 3.11 shows the induced short-circuit current distribution (real and imaginary) of the actual computed current $\mathbf{I}^{sc}$, the load short-circuit current $\mathbf{I}^{sc}_{loads}$ found using the MLS, and the interpolated short-circuit current $\tilde{\mathbf{I}}^{sc}$. Cubic spline interpolation was used to find $\tilde{\mathbf{I}}^{sc}$ from $\mathbf{I}^{sc}_{loads}$. Other interpolation methods such as ideal low-pass filtering, i.e., using
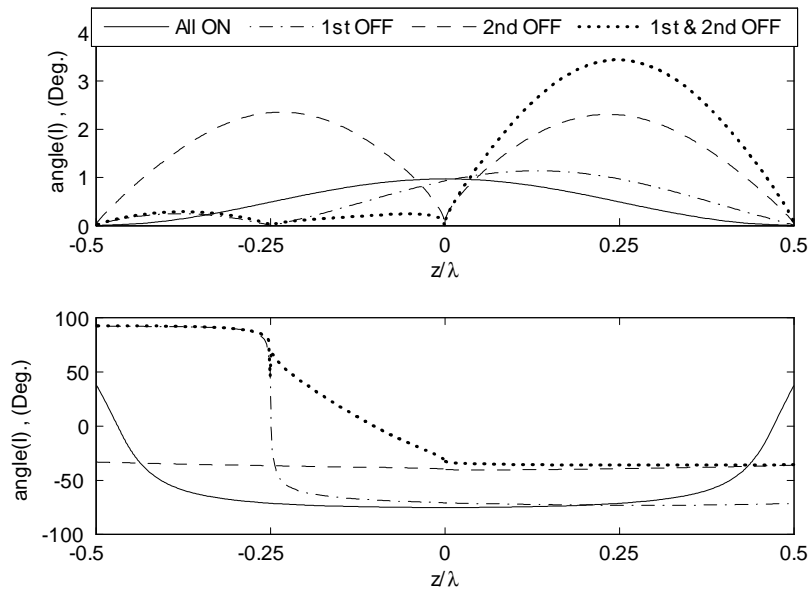
Figure 3.10. Example of linearly dependent current distributions induced on the MLS ($L = \lambda$, $M = 3$).

sink functions, were also considered. The cubic spline interpolation, however, provided the best results especially near both ends of the MLS. It is evident from Figure 3.11 that the recovered current using the MLS closely matches the actual induced current.

In general, the accuracy associated with recovering the load short-circuit current is not a function of the number of the loads per wavelength (the formulation used to obtain the short-circuit at the load locations as given in (81) is exact). The overall accuracy of the interpolated current $\tilde{\mathbf{I}}^{sc}$, however, depends on this number. For accurate interpolation, the Sampling Theorem dictates that the loads, i.e., the samples in $\mathbf{I}^{sc}_{loads}$, should be less than $\lambda/2$ apart [54]. For instance, Figure 3.12 shows the recovered short-circuit current using the MLS method with 5 loads only. Although the load short-circuits were recovered accurately, the interpolated current was not representative of the actual short-circuit current since the sampling criteria was not satisfied in this case.
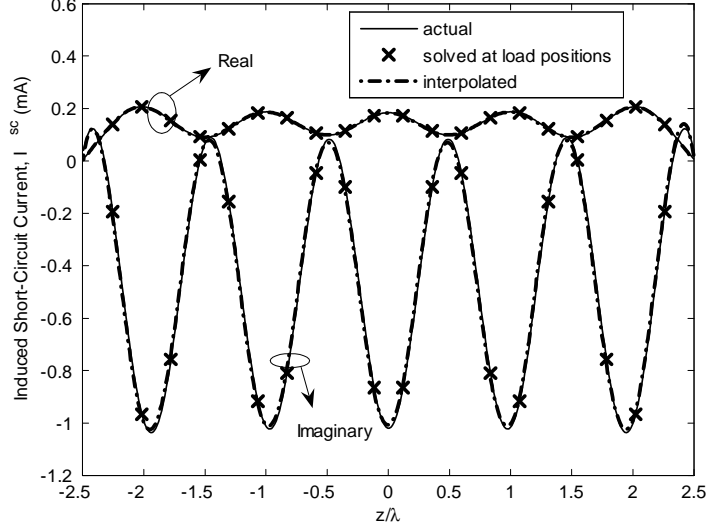
Figure 3.11. Real and imaginary parts of the short-circuit current induced on the MLS due to an incident uniform plane-wave compared to recovered currents using the MLS method with $M = 20$.

Figure 3.13 shows the root-mean-squared error (RMSE) in estimating $\mathbf{I}^{sc}$ normalized to current dynamic range as a function of the number of loads. With $L = 5\lambda$, the sampling theorem is satisfied with $M = 10$. As shown in Fig. 3.13, the interpolation error decreases rapidly as M increases beyond 10. The error floor shown for $M > 20$ is attributed to the numerical interpolation error.

3.4.2. Electric Field Mapping. To demonstrate the efficacy of the MLS method for recovering an unknown electric field distribution, the following incident electric field was considered as an example,

$$E_z^i(z) = \cos^2(0.7z)e^{jkz\cos\theta}, \, \theta = \pi/3 \tag{86}$$

The incident field in this case is a plane-wave with angle of incidence, θ, and it represents more than 100 dB of electric field magnitude dynamic range and more than two phase cycles over the length of the wire. The MLS method as described above was used to recover the incident electric field from the scattered field measurement taken at $Q(0, 100\lambda, 0)$. Figure 3.14 illustrates the effectiveness of the MLS method (with
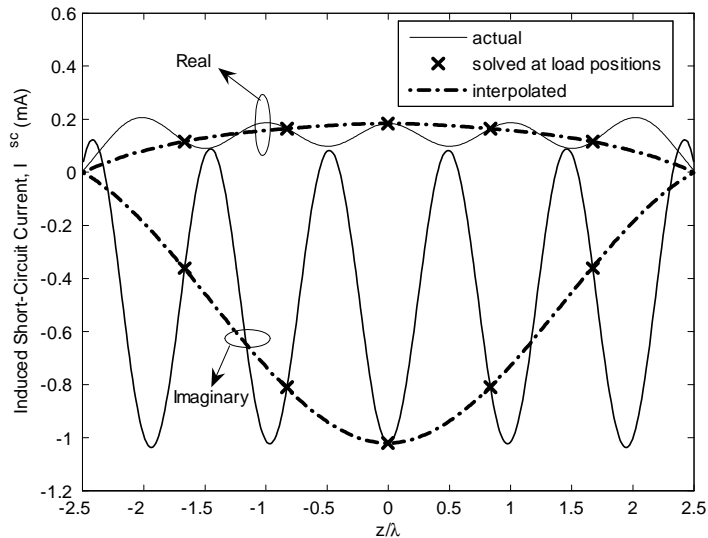
Figure 3.12. Real and imaginary parts of the short-circuit current induced on the MLS due to an incident uniform plane-wave compared to recovered currents using the MLS method with $M = 5$.

$M = 20$) for measuring the incident electric field distribution (real and imaginary) by comparing its result with the actual field given in (86). The MLS method yielded very accurate results in recovering the electric field over the whole length of the scatterer except toward the ends. The errors at the end of the wire were encountered in other simulations performed using different incident field distributions. This is thought to be due to the numerical errors associated with applying the MoM.

3.4.3. Comparison with Conventional MST. Since the MLS method is based on modulating long scatterer as opposed to several electrically small dipoles, the corresponding scattered signal level and consequently the signal-to-noise ratio at the receiver is higher compared to the conventional MST. To compare these two methods, one may use the RCS as an appropriate *figure-of-merit* which is directly related to the scattered signal level. RCS of an MST array of PIN diode-loaded dipoles, similar to the one shown in Figure 3.5, was computed and compared to the RCS of an MLS of the same length and number of loads. The MST array was 5λ long consisting of 10 identical loaded dipoles of length $\lambda/4$ interspaced by $d_z = \lambda/2$. Figure 3.15 shows
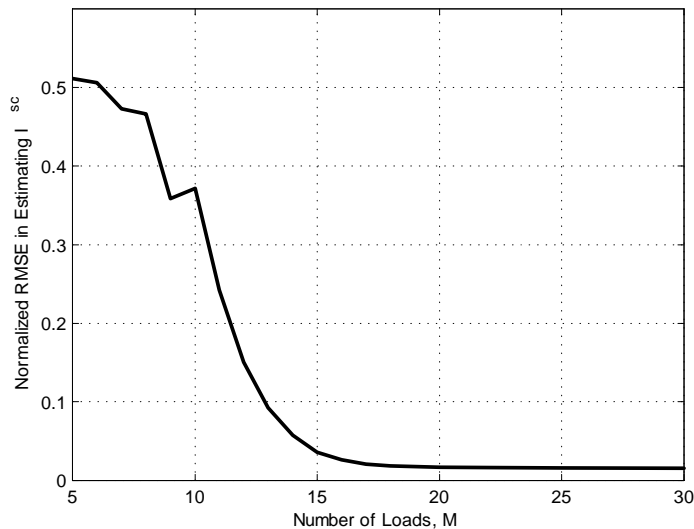
Figure 3.13. Normalized RMSE in estimating the short-circuit current induced on the MLS as a function of the number of loads, $L = 5\lambda$.

the RCS (normalized to λ^2) of the MST array and the MLS as a function of the loading/modulation conditions. For the MST, the first modulation condition is when all diodes are OFF and the remaining ten conditions, i.e., conditions $2 - 11$, consist of one diode being turned ON at a time while the rest are turned OFF. Figure 3.15 shows that the RCS of the MLS for all loading conditions is at least two orders of magnitude higher than the conventional MST.

To highlight the practical implication of the difference in scattered signal levels between the conventional MST and the MLS method on the accuracy of the estimated electric field distribution, both methods were used to recover the incident field (86) with the consideration of the receiver noise presence, i.e., uncertainty in the measured scattered field at $Q(0, 100\lambda, 0)$. Complex Gaussian uncertainty with zero mean and standard deviation of 1×10^{-4} was added to the computed scattered field observations before they were processed by both methods. In this experiment, the MST method was given the advantage of perfect calibration using a uniform plane-wave. Figure 3.16 shows the magnitude of the actual incident field and the estimated magnitude distributions obtained using the MST and the MLS method after coherent averaging
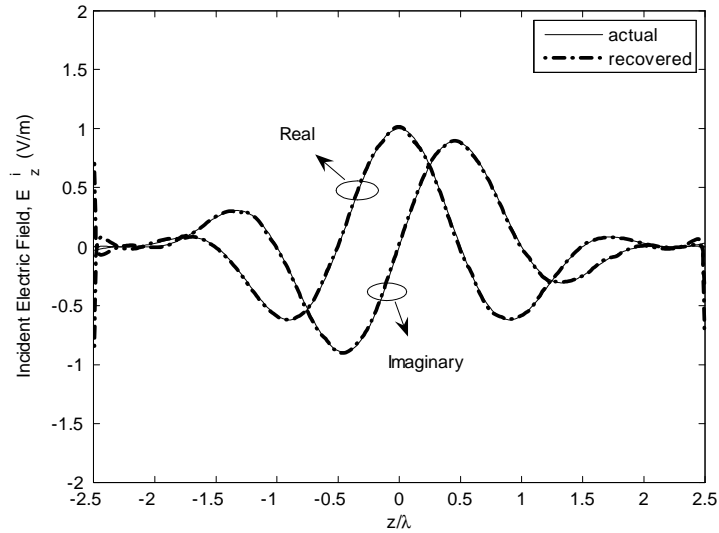
Figure 3.14. Real and imaginary parts of the actual incident field (86) and the recovered field using the MLS method with $M = 20$.

over 100 modulation cycles. The results in Figure 3.16 show that the MLS method is more immune to measurement uncertainty due to the its relatively high RCS as expected.

As mentioned earlier, the effects of static loads, i.e., fixed loads, that are not controlled dynamically in the measurement process such as dc-block capacitors and load biasing structures do not impact the accuracy of the MLS method since the differential scattered field is used in recovering the field of interest. This point was verified via simulation and is considered as an advantage of the MLS method since the effect of any fixed unintentional parasitic loads, e.g., due to component mounting, is nulled out in the process.

In the simulation results presented here, the PIN diodes were assumed to have ideal load values in both ON and OFF states, i.e., short and open, respectively. The sensitivity of the MLS method to non-ideal load values was studied via simulations as well by considering practical PIN diode loads. Theoretically, using non-ideal load values do not affect the performance of MLS method as long as these values are known. In practice, however, the non-ideal loads might decrease the sensitivity of
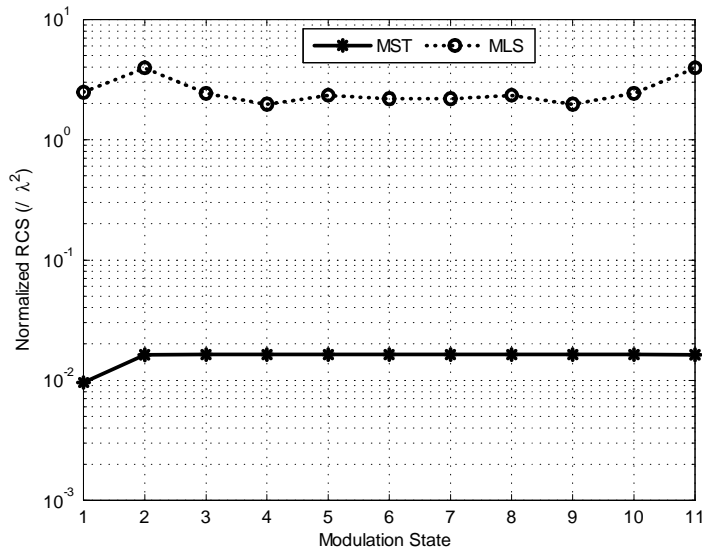
Figure 3.15. RCS of 1D MST array and the corresponding MLS of the same length $L = 10\lambda$ with 10 PIN diode loads as a function of the loading/modulation conditions.

the MLS method in the presence measurement uncertainty. With a non-ideal PIN diode which represents relatively high forward- and low reverse-bias impedances, the change in the MLS RCS between the reference condition and some of the remaining conditions might be reduced. Typical high frequency PIN diodes have forward-bias resistance less than 6 Ohm and reverse-bias capacitance in the order of 0.02 pF [49]. Consequently, the non-ideal PIN diode admittance in the ON and OFF states can be represented by $Y_{L,ON} = 0.2$ and $Y_{L,OFF} = j0.0015$ around 10 GHz, respectively. Figure 3.17 shows the modulated RCS of the MLS with $M = 10$ as a function of the loading condition when ideal and practical load values are used. The modulated RCS was computed as the absolute difference between RCS of the first loading condition and all other conditions. The reduction in the modulated MLS RCS due to the non-ideal loads is apparent in Figure 3.17. It is remarked that the modulated RCS of the MLS with non-ideal loads considered here is still higher than that of the conventional MST with ideal loads as shown in Figure 3.17.
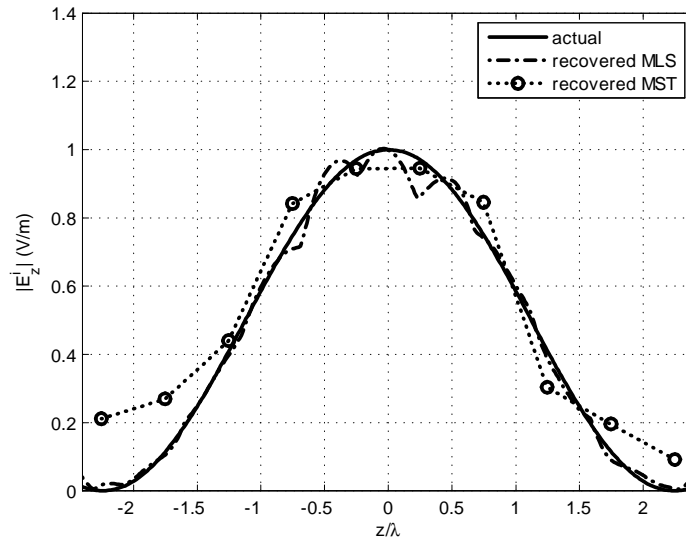
Figure 3.16. Magnitude of the estimated electric field distribution in the presence of measurement uncertainty obtained using conventional MST array and the MLS of the same length $L = 10\lambda$ and 10 PIN diodes.

It is emphasized that the load values should be known *a priori* in order to implement the MLS method. Furthermore, the scatterer structure should be modeled accurately. These are not hard-limiting factors since the load values can be measured experimentally and the structure can be modeled using available numerical techniques with high accuracy over a wide range of frequencies.

3.5. SUMMARY

To improve upon the limitations associated with the conventional modulated scatterer technique (MST), a new electric field distribution measurement method based on modulated multiple loaded linear scatterer (MLS) was developed and analyzed. The MLS method is shown to overcome most of the challenges encountered when using the conventional MST-based array of dipoles. The developed MLS method estimates the short-circuit current distribution induced over the length of the scatterer from multiple scattered field observations taken at a single point using different modulation conditions. Consequently, the estimated current distribution is used to
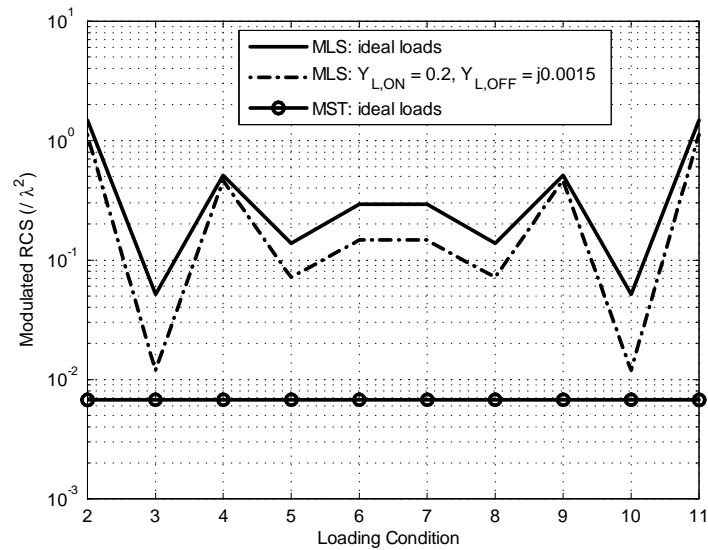
Figure 3.17. Modulated RCS as a function of the loading condition for ideal and typical non-ideal load values with $M = 10$.

recover the incident electric field distribution of interest. The operation of the MLS method was verified via numerical simulations and its performance was compared to that of the conventional MST. It was shown that the MLS method offers distinct advantage over the conventional MST as it relates to the accuracy of the recovered field distributions from noisy scattered field observations.

Future work will consider constructing a prototype MLS-based electric field measurement system. Other MLS configurations and geometries will also be subject of future research.

4. MODULATED ELLIPTICAL SLOT

Cost effective near- and far-field high-resolution microwave and millimeter wave imaging systems can be implemented using array of modulated elements [14]. As discussed in the previous section, modulating the array elements in time, facilitates spatial tagging of the incident electromagnetic field on the array spatial region, and hence, a 2D map of that field can be obtained using a single receiver (which simplifies the design considerably) [14]. Basically, modulation allows the array element to "tag" its own signal, and that not only provides a mean for the receiver to identify the location from which the signal was received, i.e., spatial multiplexing, but also enhances signal detection. This is true since from the detection point of view modulated signals are distinct from the non-coherent clutter in the environment and receiver noise. The higher the modulation depth is, i.e., how well the array elements can modulate the incident electric field, the higher is the sensitivity of the imaging system to small variations in the measured field.

As pointed out earlier, since the conventional MST uses small loaded dipoles, which result in compact array for better field sampling, they suffer from major drawbacks. The inefficiency of small dipoles limits the modulation depth and the SNR (less than 2% modulation depth was observed in Section 3). Since the modulated scattered signal level from an MST array dipole is typically very small, the robustness of the conventional MST system is undermined by the residual carrier problem (carrier suppression through tuning is needed each time the measurement setup changes). Furthermore, the mutual coupling among the array dipoles can significantly limit the system dynamic range. At high frequency, these problems render the implementation of such MST imaging array very challenging, i.e., the SNR/sensitivity factor derived in the previous section becomes very small.

From the previous analysis, it was concluded that, in order to improve upon the conventional MST, an efficient array element should be used instead of the short dipole. To this end, a modulated slot may be utilized in the imaging array. The selection of the slot is justified by the fact that microwave and millimeter wave signals can pass though a slot with minimum attenuation if the slot is properly designed. In its simplest form, once MST is applied to slots, it implies that the required modulation

is achieved by opening and closing the slot (allowing the signal to pass or not pass through the slot, respectively). Modulation depth close to 100% can be achieved when the slot is modulated between open- and close-states. Therefore, with modulated slots, the imaging system sensitivity can be considerably enhanced compared to the MST arrays based on dipoles.

To illustrate the basic idea behind using modulated slots in imaging systems, consider Figure 4.1 which shows a generic implementation of such system based on array of modulated slots [18]. The slots shown in Figure 4.1 are cut into a conducting screen (non-transparent to EM fields) and the receiver is placed behind that screen. The electric field distribution of interest is measured by opening and closing the slots via controlling their loads. At the initial state, all slots are closed and no signal passes through to the receiver. When any given slot is opened, while the rest are closed, the respective electric field at the particular location of the open slot only is coupled into that slot and subsequently, re-radiated into the opposite side of the screen where it is picked up by the receiver. Each slot is modulated, by opening and closing it, at a certain modulation rate. In this way, the electric field due to each slot can be individually discriminated and measured using a single receiver.

In imaging applications, the effect of the reflection from the array due to the conducting screen should be accounted for properly, i.e., through calibration. When all slots are open, the array becomes transparent to the EM waves at the frequencies where the slots are efficient (spatial band-pass filter) [55]. When most of the slots are closed, the reflected waves from the array might interact with the source of the incident field, i.e., the object to be imaged. Multiple reflections between the array and the source may change the field distribution of interest. This situation can be resolved in practice by increasing the distance between the array and the source. Measuring the field of interest at multiple array-source distances can reduce the effect of multiple reflections considerably. Using absorbing material to cover the exposed conductor on the array can also reduce these reflections to a large extent. Similar remedies are typically used with the conventional MST arrays of dipoles and can be applied to the array of slots [51].

In order for the imaging scheme described above to work, the slot should be designed such that it can be opened and closed completely and respond very quickly
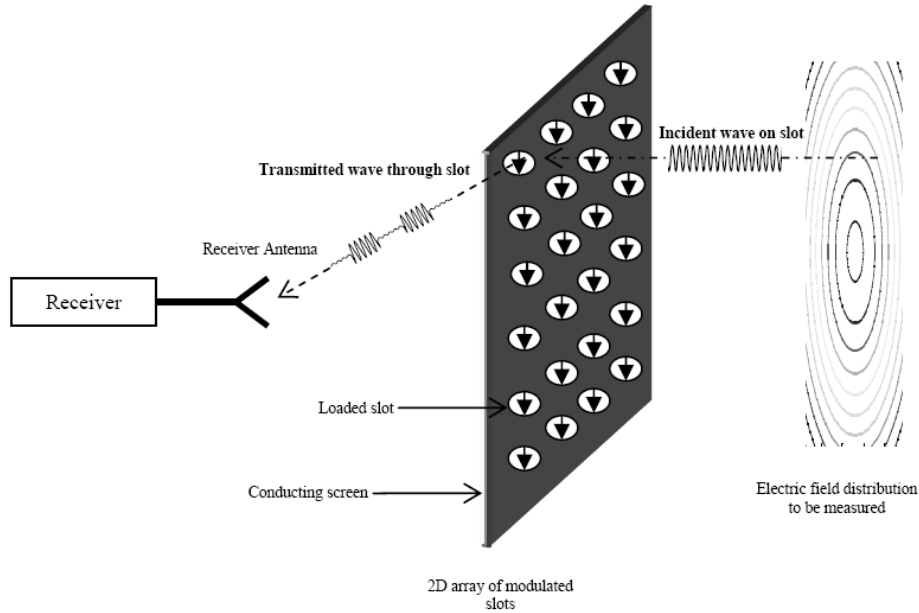
Figure 4.1. Generic implementation of an imaging system based on array of modulated slots.

to an electronic control signal. The dimensions of the slot (in both directions) should be less than $\lambda/2$ for proper electric field sampling (to prevent aliasing as dictated by the Sampling Theorem [54]). A design of a slot which meets these requirements will be presented next.

4.1. MODULATED SLOT DESIGN

Since they are relatively easy to manufacture and possess a low profile as flush-mounted antennas, slots in conducting ground planes are used extensively in many applications [56]. Recently printed elliptical and circular slot designs have received considerable attention for realizing ultra-wideband antennas for wireless communication systems (comprehensive reviews of the most recent designs can be found in [57] and [58]). Here, the design of a novel, compact and resonant slot for imaging system realizations is presented. The advantages of using resonant slots are multifold. First, the resonant slot can have, through special loading, a small form-factor. Second, with

small resonant slots, the mutual coupling between various array slots can be significantly reduced (see [59] and the references therein). Furthermore, once the resonant slot is used as a modulated element, the modulation depth can be maximized toward enhancing the sensitivity of the imaging system. These advantages working together not only make the imaging system highly sensitive, but also promote high-resolution imaging [18].

Figure 4.2(a) shows the schematic of the designed modulated resonant slot. The designed slot has an elliptical shape with major and minor radii r_1 and r_2, respectively, cut into a conducting plane. This slot is linearly polarized along the direction of the ellipse's minor axis, i.e., y-axis, and it has a broadside radiation pattern with wide beamwidth. For imaging purposes, it is advantageous to have a wide radiation beam pattern. Slots with wide-beam radiation pattern posses very low spatial selectivity and thus insure detection from all directions. Furthermore, for synthetic array processing, e.g., SAFT, wide-beam patterns are also desirable in order to attain the maximum possible spatial resolution.

In order to realize a compact array, the largest dimension of the slot must be less than half-wavelength. Hence, the elliptical slot by itself will be a sub-resonant inductive slot. To make the slot resonates at a certain frequency, it is loaded by a conductive circular load of radius r_L, as shown in Figure 4.2(a). In essence, the gap of length L_g, shown in Figure 4.2(a) between the circular load and the edge of the elliptical slot, adds capacitance to the overall slot structure. Consequently, the inductive elliptical slot and the capacitive gap element result in a single resonant structure. This is true even though the largest linear dimension in the overall slot structure is less than half-wavelength. Such concept is typically followed to design resonant waveguide irises [59].

The resonance frequency of the elliptical slot structure shown in Figure 4.2(a) is function of the slot dimensions; namely r_1, r_2, and L_g ($L_g = r_2 - r_L - s$). Thus, one can control/change the resonance frequency by changing these (interdependent) dimensions. Primarily, reducing r_1 and r_2 increases the resonance frequency. Increasing L_g makes the slot resonate at lower frequencies. The obtained bandwidth around the resonance freqeuncy is a function of the slot axial ratio r_2/r_1. On the other hand, since the resonance frequency is a function of the slot capacitance, this frequency
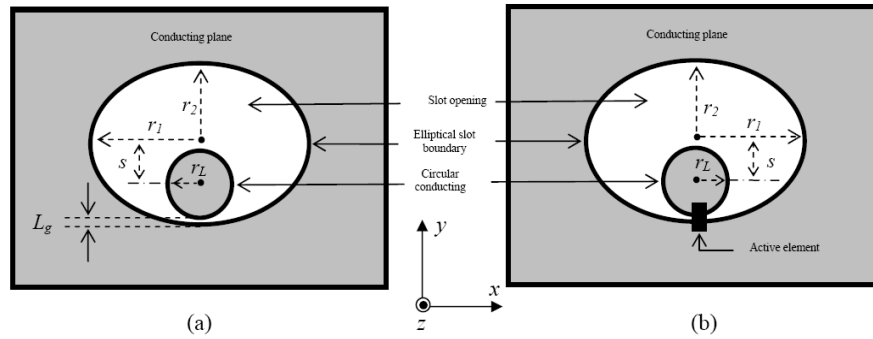
Figure 4.2. Schematic of the designed elliptical slot (a) with, and (b) without the active element load.

can be controlled electronically via loading the slot with an active element, e.g., PIN diode, varactor diode, etc., as shown in Figure 4.2(b). Changing the properties, e.g., capacitance, of the active element, causes the resonance frequency to change. In general, when the active element is capacitive, its capacitance is added to the gap capacitance, and consequently the resonance frequency decreases compared to the unloaded slot case shown in Figure 4.2(a). The properties of the active element can be controlled electronically, e.g., by a dc control voltage applied across the element. This effect is used to modulate the slot in time, i.e., opening and closing it.

Near or in the millimeter wave region, the capacitance of typical active elements available nowadays in the market might not change sufficiently in response to their control signal. Thus, such elements cannot be arbitrarily selected and placed to load the slot because they might not produce the desired change in the resonance frequency of the slot. Therefore, in order to attain an efficient control over the slot properties, the active element should be placed in high-intensity electric field region where it can cause maximum field perturbation. Consequently, the slot resonance frequency changes as desired in response to a change the in the electrical properties of the active element. In order to realize this concept, the electric field is "forced" to concentrate in one region between the elliptical slot boundary and the circular load. This is the main reason behind offsetting the circular load center from the elliptical slot center by certain amount, s, toward one of the boundaries (basically forming a small gap with high field density). This offset has the effect of "trapping" the electric

field in the region between the elliptical slot boundary and the circular load. Thus, the slot capacitance is primarily determined by the gap and whatever else placed near that gap, i.e., the active element. Consequently, the resonance frequency of the slot can be properly controlled with commercially available active loads.

It must be mentioned here that the desired capacitance change can be synthesized using combination of active elements and distributed loads, i.e., transmission line stubs. Such an option, however, is not always feasible for compact array designs since it requires additional space around the slot area. For compact array design used for high resolution imaging, the array spatial area is typically cramped by the slots themselves and the control bias lines routed to each slot.

Loading the slot with a PIN diode is of particular interest here since it allows the desired rapid control effect (switching time in order of few nanoseconds) and consumes relatively small amount of power. When the diode is forward-biased (turned ON), its resistive impedance "shorts" the gap between the circular load and the elliptical slot edge, and consequently, the slot (actually its dominant field mode) does not resonate in the band, i.e., at the frequency of interest where the receiver is expecting a signal. In this state, the slot does not allow any signal to pass through, i.e., the slot is "closed". When the diode is forward biased, it represents a capacitive load which adds to the gap capacitance and makes the slot resonate at the design frequency of interest, and hence, signals at that frequency pass through the slot, i.e., the slot is "open". Consequently, maximum modulation depth can be achieved. In practice however, the modulation depth may be reduced due to signal leakages (when the slot is closed) and losses (when the slot is open).

4.1.1. Field Distributions. Studying the electric field and the current distributions in and around the slot area, respectively, is vital for proper slot design as well as for understanding its behavior, i.e., mutual coupling, when it is placed near another slot in an array. For imaging applications where the objective is to measure the relative electric field in a certain spatial domain, it is important to make sure the slot is sensitive to the field component of interest (proper polarization) and that it provides a response proportional to the local incident field on it (obtaining localized field measurements).

Numerical electromagnetic simulations were performed to investigate various attributes of the designed PIN-diode loaded elliptical slot. To this end, CST Microwave Studio® commercial simulation package was used [60]. Although many idealistic simulation models were considered in the early stages of slot prototyping, i.e., using perfect electric conductors, PIN diode with zero-ohm forward resistance, etc., the results presented here are obtained from simulating a practical 24 GHz elliptical slot on a printed circuit made of a lossy conductor, i.e., copper. The PIN diode in the ON and OFF states was modeled as a lumped element with impedance of 5 Ohm and $-j265$ Ohm (at 24 GHz), respectively. In simulation, the slot was fed by a K-band rectangular waveguide aperture with finite flange of size 21 mm $\times$ 21 mm, i.e., the slot was mounted on the flange. Table 4.1 lists the dimensions of the simulated slot. The design specifics of this slot will be described later in this section.

Table 4.1. K-band resonant elliptical slot dimensions (Resonance frequency: 24 GHz).

Parameter	Dimension (mm), [mils]
r_1	2.36, [93]
r_2	1.78, [70]
r_L	0.78, [31]
s	0.58, [23]

Figures 4.3 and 4.4 show typical normalized spatial distributions of the electric and magnetic field components (in the x, y, and z directions) for the simulated resonant elliptical loaded slot at 24 GHz (the PIN diode is not shown in the figures). The field distributions for both the ON and OFF PIN diode states are provided in Figures 4.3 and 4.4. As shown in these figures, when the diode is in the OFF state (slot is open), the field components E_y and H_z are much higher than the rest of their respective components. This indicates that the slot fields are mainly linearly polarized. The slot is shown to be mostly sensitive to electric fields polarized along the y-axis. It is also shown that the fields are more concentrated around the circular load and the gap area between that load and edge of the elliptical slot when the slot is open. Consequently, the integral of the field over the slot area is largely determined by the

fields distributed in the small area around the circular load. This basically means that the slot is more sensitive to the local incident fields on that small area rendering localized field measurements as desired. It is also interesting to note that, the signal couples into the slot when it is open primarily via the magnetic field component H_z (slots in general provide higher magnetic coupling).
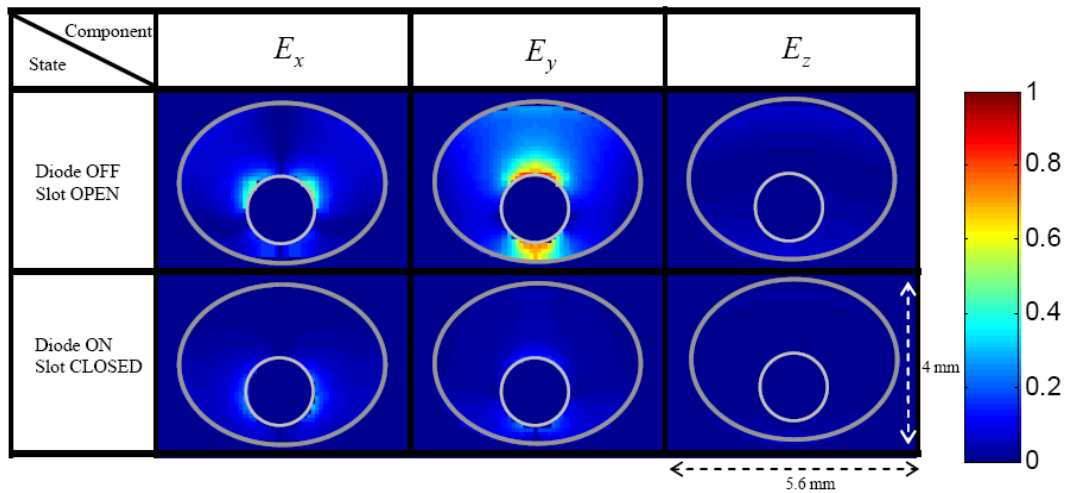
Figure 4.3. Distributions of the three electric field components in the slot area for both ON and OFF diode states.

When the PIN diode is turned ON, Figures 4.3 and 4.4 show that the electric and magnetic fields reduce significantly compared to the OFF PIN-diode state. This is especially true in the electric field case shown in Figure 4.3 where the magnitudes of the three field components become almost zero in the slot area when the diode is turned ON. Hence, in the ON PIN-diode state, the slot blocks the signal and does not allow it to pass through; that is, the slot is closed.

When the PIN diode is turned ON (slot is closed), the magnetic field component H_z remains relatively high around the area where the PIN diode is located as shown in 4.4. The coupled energy into the slot due to this component when the diode is turned ON (slot is closed) is not totally radiated by the slot. Large portion of this energy is dissipated in the forward-bias resistance of the PIN diode. However, the
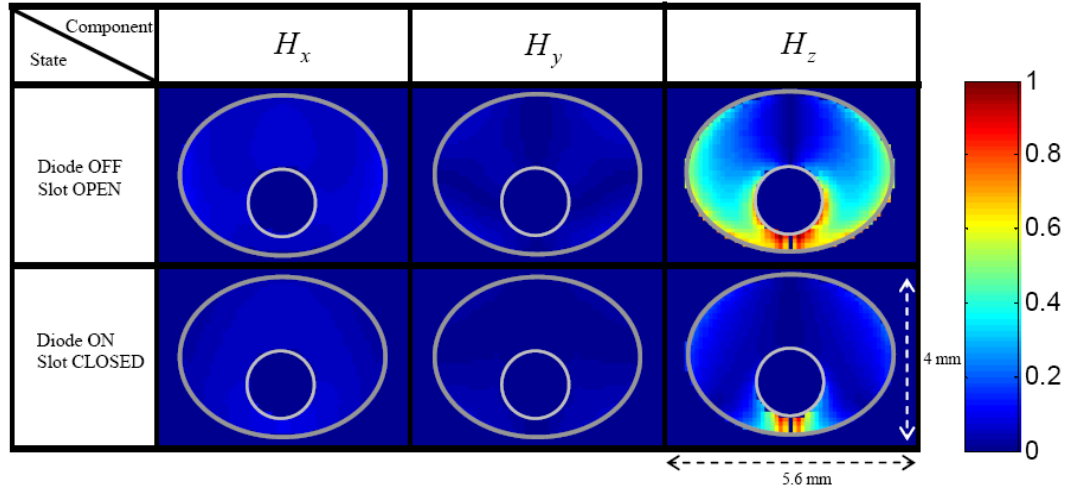
Figure 4.4. Distributions of the three magnetic field components in the slot area for both ON and OFF diode states.

remaining small portion actually gets radiated, i.e., it induces a current on the slot structure. Consequently, the slot can not be completely closed, and this in turn, may reduce the obtained modulation depth slightly compared to the ideal zero-ohm PIN diode case as it will be shown later.

Examining the surface current distribution on the slot structure gives valuable insight about its behavior when it is open and closed. The surface current distribution follows the distribution of the tangential components of the magnetic field. Figures 4.5(a)-(b) show the magnitude distribution of the tangential components (x and y) of the magnetic field around the slot area in the ON and OFF PIN diode states, respectively (note that Figures 4.5(a)-(b) have different scales/color-bars). When the slot is open, the 24 GHz signal induces a current density on the metallic structure around the slot as shown in Figure 4.5(a). In this case, the slot radiates efficiently. The high current density around the diode location indicates that most of the current actually passes through that point.

When the diode is turned ON (the slot is closed), small amount of energy is coupled into the slot and this energy hardly induces any radiating currents around the slot as shown in Figure 4.5(b). In this case, high current density is observed again around the diode. As pointed out before, in this state, the diode represents a

resistive load, and consequently, most of the energy coupled into the slot (due to H_z) is dissipated in the diode.
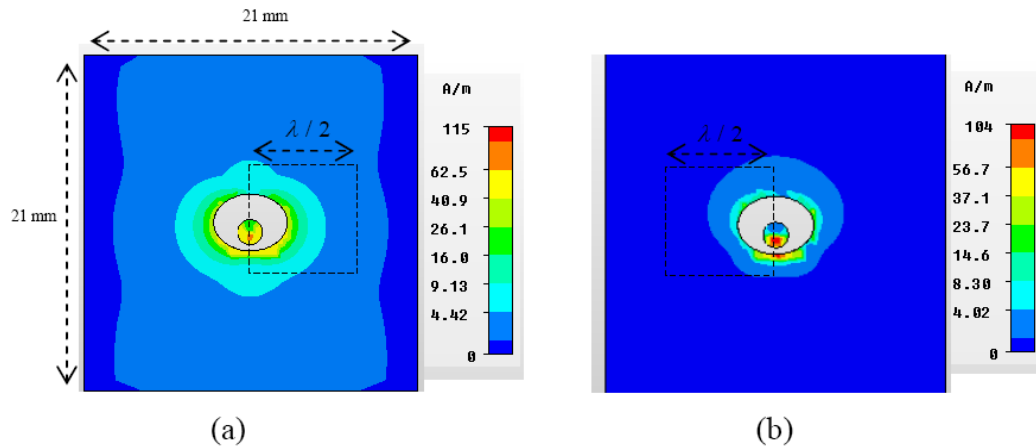
Figure 4.5. Tangential magnetic field distributions ($\propto$ surface current density) around the slot for (a) OFF and (b) ON diode states.

In 2D imaging arrays, the slots will be placed near one another within $\lambda/2$ side-by-side along the x-axis (H-plane) and in a collinear arrangement along the y-axis (E-Plane). Typically and as described before, one of the slots will be open while the rest in the array are closed at any given time. The interaction (transfer of energy) between the open slot and remaining closed slots constitutes the so called "mutual coupling". From results presented in Figure 4.5(a)-(b), it can be seen when two slots are placed in a collinear arrangement along the y-axis, they will interact more than when they are placed side-by-side along the x-axis (the surface current in the former case extends and reaches out further than the latter). Mutual coupling between similar resonant slots (similar current distributions) was studied thoroughly via numerical simulation as well as experiments in the past by Abou-Khousa and *et al* [59]. It was found that the mutual coupling between such slots is actually very small (less than -20 dB for a typical $\lambda/2$ interspacing).

4.1.2. Far-Field Radiation Pattern. Figures 4.6(a)-(b) shows typical far-field pattern of the designed loaded elliptical slot (diode OFF) presented in 3D

and rectangular plots, respectively. As shown in Figure 4.6(b), the 3-dB beamwidths in both principle planes (E- and H-planes) are around 50 and 60 degrees, respectively. Such wide beams in both planes are suitable for the imaging applications of interest as discussed before.

(a)   (b)
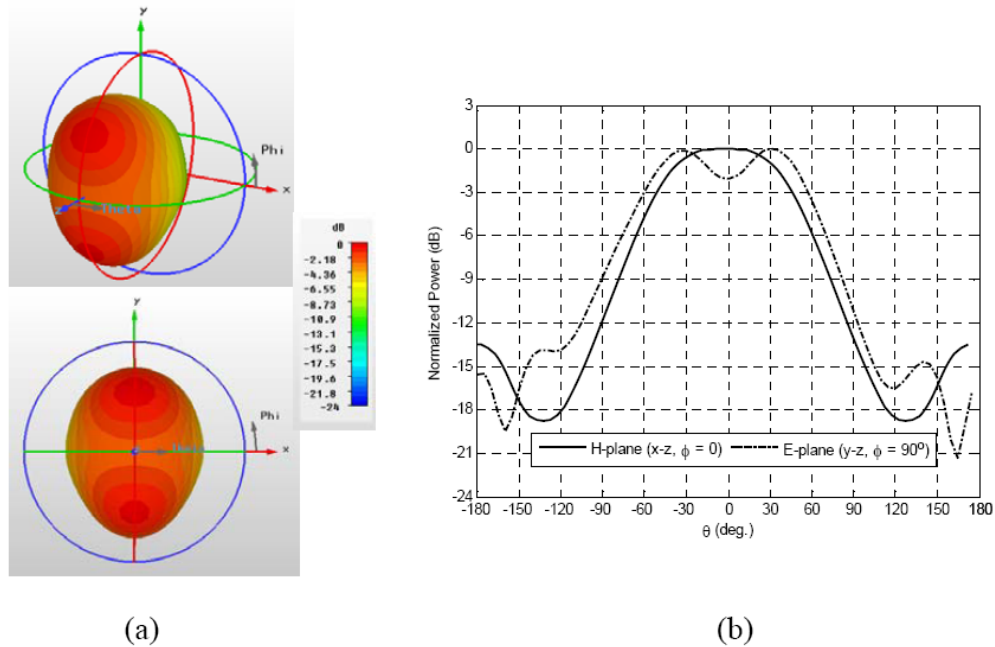
Figure 4.6. Typical far-field pattern of the loaded elliptical slot (diode OFF) presented in: (a) 3D, and (b) rectangular plots.

The radiation efficiency of this slot is high as desired for sensitive field measurements (around 97%). Note that the ripple in the main beam of the E-plane pattern is mainly attributed to the finite ground plane effect [36], i.e., the flange size

was 21 × 21 mm (the surface current reaches the edge of the flange in that plane as shown in Figure 4.5(b)). This effect was confirmed via simulations.

4.2. K-BAND SLOT

To demonstrate the operation of the proposed resonant slot, an elliptical slot was designed to resonate at 24 GHz in the K-band (18-26.5 GHz) when loaded with a PIN diode.

4.2.1. Slot Design. Table 4.1 lists the pertinent dimensions of the designed slot. A magnified picture of the slot is given in Figure 4.7. The slot was manufactured using standard photolithographic printed circuit board (PCB) manufacturing technique on a Rogers4350 board of 0.020" (0.5 mm) thickness. Note that the free-space wavelength is around 12.5 mm (492 mils) at 24 GHz. The largest slot dimension, $2r_1 = 4.72$ mm, is a bit larger than one-third of the free-space wavelength. In fact, it is challenging to realize a resonant slot with these dimensions without special loading as in the case of this novel design.
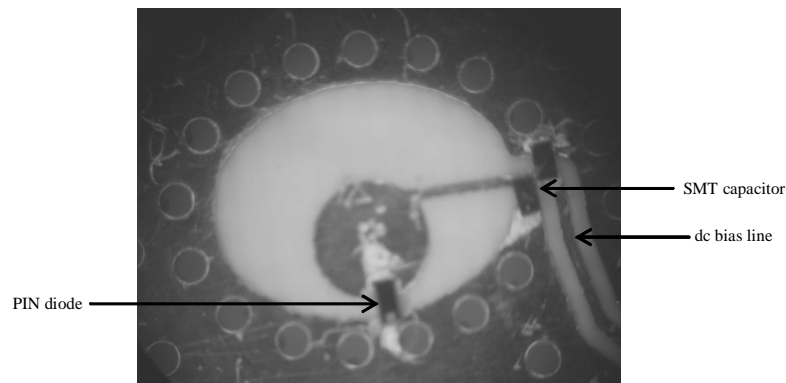
Figure 4.7. A magnified picture of the manufactured K-band slot and biasing structure.

Ma-com MA4GP907 flip-chip high frequency flip-chip PIN diode (0.63 mm × 0.38 mm) was used to load the slot [49]. The PIN diode was controlled by dc bias line (0.25 mm wide) routed to the circular load location, as shown in Figure 4.7.

In the slot opening region, the bias line was routed such that it was orthogonal to the dominant mode electric field polarization, and hence, its perturbing effect was minimized. The used PIN diode needed 1.45V to switch between the reverse the forward states. When reverse biased, the diode represents a capacitive load of ~ 25 (fF), and in the forward state it is equivalent to 5-Ohm resistive load. Additionally, 5-pF small surface-mount (SMT) capacitors (0.5 mm $\times$ 0.25 mm) were used to realize an RF return path to ground (short-circuit) for any signal that might couple into the dc bias lines, and thus preventing any spurious radiation or resonances that could result from such coupling.

4.2.2. Reflection Measurements. The slot was fed by a K-band rectangular waveguide and the input reflection coefficient, S_{11}, was measured using HP8510C Vector Network Analyzer (VNA), e.g., the waveguide was connected to port 1 of the VNA. Figure 4.8 shows a schematic of the measurement setup and the magnitude of the measured reflection coefficient, S_{11}, for the cases when no diode is used for loading, the diode is OFF and the diode is ON. Figure 4.8 also compares the experimental and numerical simulation results. From the measurement results, it is observed that when the slot is not loaded with the diode, it resonates at around 25.5 GHz (the point of minimum reflection).

Loading the slot with the reverse biased PIN diode (i.e. OFF) increases the overall capacitance and consequently shifts the resonant frequency to around 23.82 GHz as shown in Figure 4.8. This shift is expected since the diode is in parallel with the offset gap between the circular load and the edge of the elliptical slot. It is observed that the developed resonant slot has a 20 dB-return-loss bandwidth of 530 MHz centered around 23.8 GHz as indicated in Figure 4.8. At 24 GHz, when the diode is switched ON, the reflection is high indicating no signal is passing through the slot (reflection around -0.7 dB and the slot is closed). On the other hand, when the diode is switched OFF, the reflection coefficient at 24 GHz is very small indicating that most of the signal couples into the slot (around -22.8 dB and the slot is open). Thus, the modulation depth is maximized as it will be examined further later. It is also observed that the difference between the ON and OFF state over the 20 dB-return-loss bandwidth is larger than 19 dB. This will result in high modulation depth
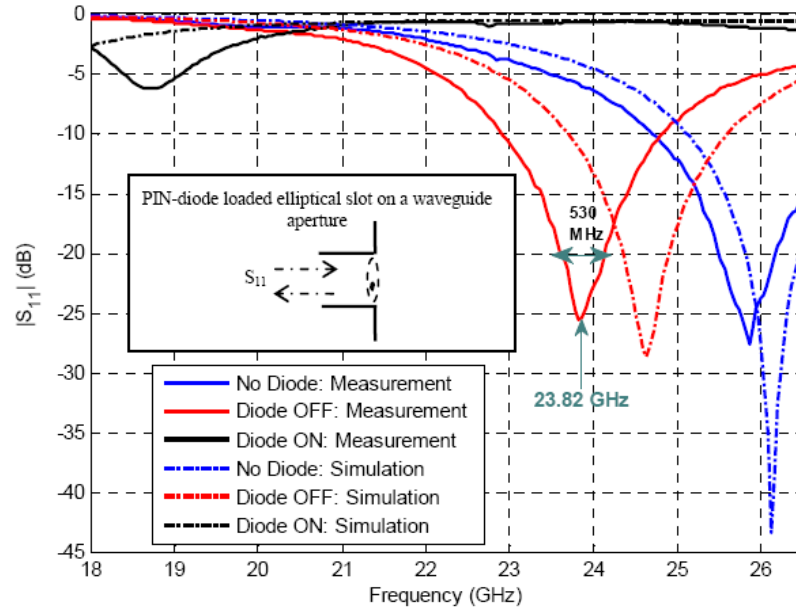
Figure 4.8. Magnitude of the reflection coefficient of the designed slot fed by a rectangular waveguide.

over 530-MHz bandwidth. Consequently, using this slot, the overall system becomes more robust against signal source drifts.

In general, the simulation results are in good agreement with the measurement results. The small discrepancies such as the shift in resonance frequency may be attributed to the manufacturing tolerance margins in material and dimensions (which can not be accounted for in simulations), as well as change of diode parameters around their nominal values.

4.2.3. Transmission Measurements. Although the reflection experiments discussed above validates the basic slot design, i.e., resonance frequency, it is imperative to study the slot modulated response in a typical transmission-through setup (as it will be used in the imaging array). Figure 4.9 shows the measurement setup and results of a through transmission experiment. An antenna connected to port 1 of the HP8510C VNA was used illuminate the slot from 12.5 cm (5 in) away. The slot was mounted on the aperture a waveguide connected to port 2 of the VNA. The measured baseband complex signal, i.e., S_{21}, is shown in polar format in Figure 4.9(a). The

small transmission coefficient seen near zero when the slot is closed indicates very small signal gets transmitted through the slot. When the slot is open, maximum signal passes through the slot to the receiver of the VNA. The magnitude and phase of the complex signal **S**, the vector difference between the signals received when the slot is open and closed as depicted in Figure 4.9(a), corresponds to those of the incident signal. Just like modulated dipoles, ideal detection should consider the vector difference, **S**, between the received signals for both modulation states.

Figure 4.9(b) shows the baseband measured signal as the slot is modulated over time between the open and closed states in rectangular magnitude/phase format. The magnitude difference between signals received when the slot is open and closed is as high as 15 dB which indicates very strong modulation as it will be quantified next.
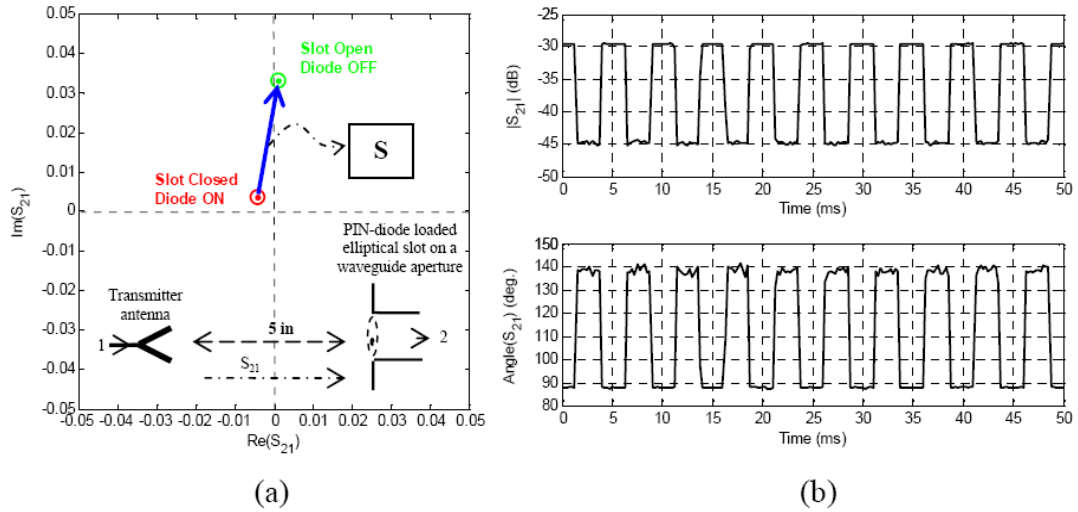
Figure 4.9. The baseband signal transmitted through the slot represented in (a) polar and (b) rectangular magnitude/phase formats.

4.2.4. Modulation Response. The modulation depth is the ultimate figure-of-merit which truly establishes the utility of the designed slot as a modulated element in an imaging array. The baseband signal measurements performed using the VNA as presented above can not be used to estimate the modulation depth accurately

(the VNA has a narrow-band tuned-receiver which cannot be used to measure the 24 GHz carrier signal and the modulation sidebands at the same time). To measure the modulation depth, the designed slot was modulated at 20 kHz and the spectrum of the received signal was measured using a spectrum analyzer. For ideal ON-OFF modulation, the modulated signal will be 6.02 dB below the carrier when the slot is completely opened and closed in modulation. As shown in Figure 4.10, with the designed slot, the fundamental signal harmonic is 6.33 dB below the carrier (dBc), i.e., 0.31 dB deviation from the ideal case. This small discrepancy arises from small signal leakage and losses when the slot closed and opened, respectively (as it can be noted from the above simulation and measurement results).
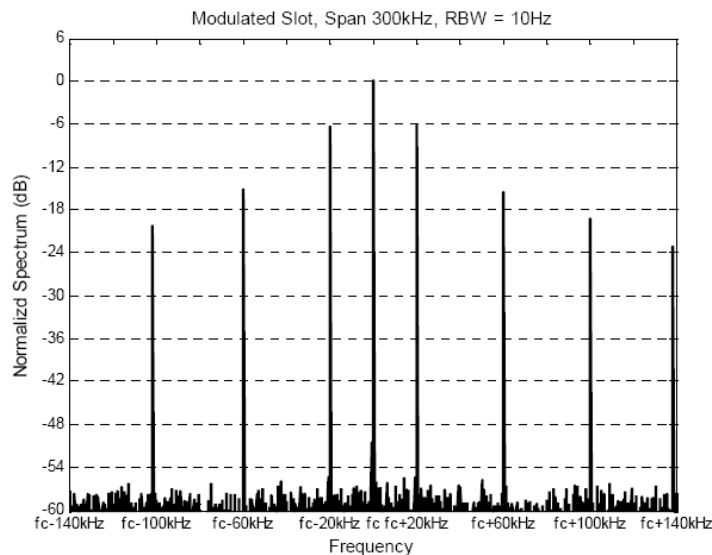
Figure 4.10. Measured normalized spectrum of the signal received through the K-band slot, $f_c = 24$ GHz.

The slot modulation depth is calculated from the spectrum measurements presented in Figure 4.10, i.e., using (67), to be 96.5%. Such a high modulation depth is attributed to the unique design of the slot where it can, almost completely, be opened and closed. At this point, it is interesting to compare the modulation

depth obtained using the designed slot with that of $\lambda/2$ (cf. Figure 3.3) and $\lambda/4$ (cf. Figure 3.4) dipole elements. Table 4.2 lists typical modulated signals level, relative to the carrier (D in dBc), as received from these loaded elements and the corresponding modulation depths in bistatic arrangements at 24 GHz. It is clear that the modulation depth using the designed slot is significantly higher compared to dipole elements case.

Table 4.2. Comparison between the measured modulation depths for four loaded elements.

Element	D (dBc)	Modulation Depth (%)
Elliptical Slot	6.33	96.5
$\lambda/2$-Dipole	41	1.8
$\lambda/4$-Dipole	50	0.63

As opposed to the conventional MST based on modulated dipole elements, detecting a modulated signal that is 6 dB below the carrier such as the one resulting from modulating the designed slot is not problematic. In this case, proper amplification can be used to boost the modulated signal level without saturating the receiver front-end as in the conventional MST systems. Besides improving the system sensitivity by the virtue of increasing the modulation depth, the residual carrier suppressing procedures routinely used with the conventional MST imaging arrays are not needed when the designed slot is utilized. This enhances the robustness of the imaging system.

4.2.5. Design Enhancement. The modulated response of the slot is affected by the signals leaking from/to biasing structure, i.e. the line used to control the PIN diode. In the design demonstrated above, small surface mount (SMT) decoupling capacitors were used to reduce this coupling (see Figure 4.7), and consequently, enhance the modulation depth. In 2D imaging arrays where hundreds of slots may be used, mounting such capacitors on each slot may be costly and time consuming. A simple remedy is to route the bias line on the bottom PCB conductor using vias. At high frequencies, a cross-layer via presents high-inductive impedance, and hence, it achieves the required signal decoupling without the need for SMT capacitors.

To illustrate the above idea, consider Figure 4.11(a) which shows schematics of the unloaded slot without biasing components, i.e., SMT capacitors, and two unloaded slot designs with different bias line routing. One of designs uses bias line components, i.e., SMT capacitors, just like the design considered earlier. The second loaded slot design does not incorporate any SMT capacitors and uses vias to route the bias line instead as shown Figure 4.11(a). The magnitude of the measured reflection coefficient for each of these three slots is shown in Figure 4.11(b).
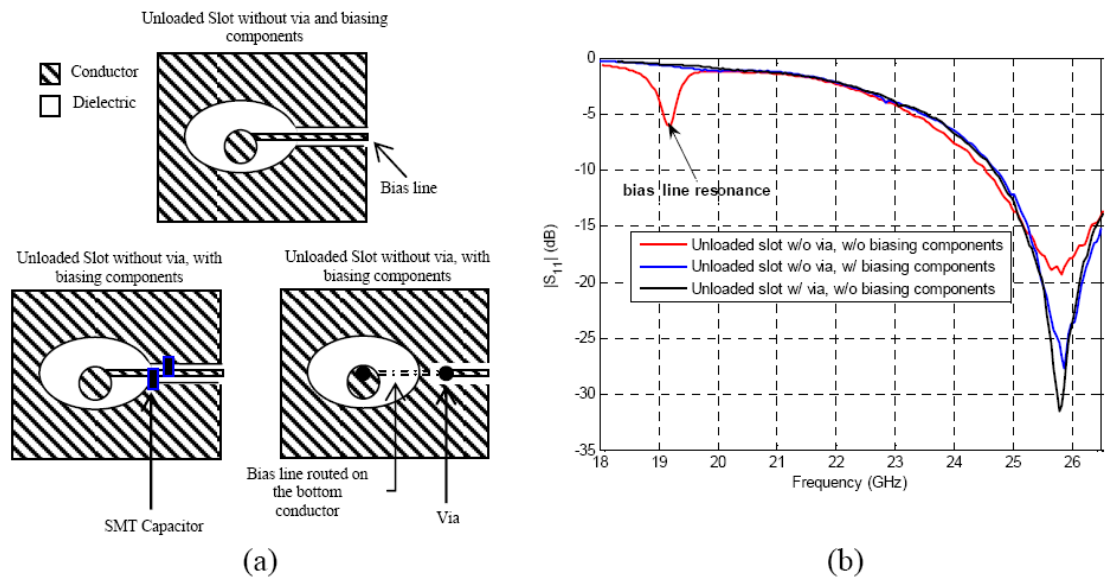
Figure 4.11. (a) Schematics of unloaded elliptical slots with different bias line routing, and (b) the measured magnitude of the reflection coefficient, S_{11}, corresponding to the slots shown in part (a).

When neither SMT capacitors nor vias are used, signals couple into the bias line and it shows up as relatively low-frequency resonance in the measured response (the resonance is due to higher-order slot mode. Generating this mode requires energy to be taken away from the dominant mode). In this case, the minimum measured response is around -19 dB. Using SMT capacitors reduces the coupling to the bias line (its resonance disappears) and causes the minimum reflection to become -27 dB

(getting better). The reflection response with vias, not only reduces the bias line coupling but also reduces the slot reflection further (-31 dB) compared to routing using SMT capacitors as shown in Figure 4.11(b). This in effect improves the slot performance (how well it opens and closes). Note that adding the SMT capacitors and vias change the resonance frequently slightly. This shift was accounted for in order to make the point about the minimum reflection in each case.

4.3. SUMMARY

A novel modulated slot design has been proposed and tested. The proposed slot is aimed to replace the inefficient small dipoles used in conventional MST-based imaging systems. The developed slot is very attractive as MST array element due to its small size and high efficiency/modulation depth. In fact, the developed slot has been successfully used to implement the first prototype of a microwave camera operating at 24 GHz. It is also being used in the design of the second generation of the camera [18].

Finally, the designed elliptical slot can be used as an electronically controlled waveguide iris for many other purposes (for instance in constructing waveguide reflective phase shifters and multiplexers/switches)

5. MODULATED APERTURE PROBE

Near-field microwave and millimeter wave non-destructive testing (NDT) and imaging techniques have shown great utility for wide range of applications. Reflectometer probes with open-ended rectangular waveguide apertures as probing antennas are commonly used for near-field NDT and imaging. The open-ended waveguide aperture is used to illuminate the structure under test (SUT) and to receive the reflected signal. The detection system is designed to produce a dc signal proportional to the phase and/or magnitude of the reflected signal. In most cases, the detection system may simply consist of a diode detector, e.g., a standing wave reflectometer. For imaging purposes, the waveguide aperture is scanned over the SUT and the measured output dc signal is mapped into a 2D intensity raster image [1].

Near-field probes are intrinsically sensitive to the variations in the distance between the probing antenna and the structure under inspection, i.e., standoff distance [1]. Such variations can potentially mask the signal of interest in an image, such as the signal due to a subsurface defect or an anomaly and hence adversely influence the detection capability of the probe. Consequently, it is imperative that the standoff distance is kept constant during the scanning process. While this is somewhat manageable for structures with relatively flat surfaces, it is rather difficult to achieve for curved surfaces or when the standoff distance changes as a result of vibrations frequently encountered in practice, i.e., imaging a conveyed material. Moreover, change in standoff distance becomes more of a problem at high frequencies at which finer spatial resolutions are possible for detecting small defects and the field properties change more significantly as a function of and in the direction of propagation [1], [31].

Several solutions have been proposed in past to eliminate or compensate for the adverse effect of standoff distance variation. These solutions can be divided into two categories; namely, non-coherent and coherent methods. Non-coherent standoff distance compensation methods involve the concurrent detection and processing of two signals non-coherently, i.e., without considering phase information. While one of the detected signals solely maps the standoff distance variation, the second signal bears the information due to standoff distance variation and the signal of interest. Thus, by special processing, the signal due only to standoff distance variation can

be used to eliminate this influence from the second signal. The methods proposed in [24] and [61] belong to this category. These methods, although modest in complexity, require special scaling, i.e., calibration, and typically offer a relatively small range of standoff distance compensation, e.g., less than quarter of the wavelength. The simplicity of these methods stems from the fact that they are based on non-coherent detection.

On the other hand, coherent compensation is based on subtracting two signals coherently using their phases and magnitudes. As in the non-coherent methods, one of processed signals carries the standoff distance information and the second contains both the signal of interest as well as the signal due to the standoff distance. To realize both signals simultaneously, two spatially-spaced waveguide apertures are incorporated in scanning the structure [62]. The probe proposed in [62] is based on two radiating apertures whereby a magic-T is used to coherently subtract the signals reflected from both apertures. This method offers a standoff distance compensation range beyond one wavelength, which is a significant distance. While such a differential probe is highly effective, its design is more complex compared to the non-coherent methods.

However, a non-coherent (simple) differential probe which can offer large compensation range compared to the previously proposed methods has not been developed yet. To this end, a near-field microwave and millimeter wave differential probe based on a novel dual-loaded modulated single waveguide aperture was recently designed and developed [63], [64]. Using this novel design the undesired influence of standoff distance variation can be eliminated, or otherwise significantly reduced by non-coherently detecting and subtracting the signals measured at two different aperture modulation states. Here, detailed analysis of the dual-loaded modulated aperture probe is presented. The probe concept is validated and its response, sensitivity, and resolution are investigated via numerical electromagnetic simulations. Such analysis

provides insight into the probe design and helps in better understanding of the probe capability in near-field millimeter wave imaging applications [64].

5.1. DUAL-LOADED APERTURE CONCEPT

The proposed probe is based on switching between two electric field distributions synthesized over a single rectangular waveguide aperture of dimensions $(a \times b)$. To illustrate this idea, consider Figure 5.1(a) showing the relative magnitude distribution of the aperture electric field when the dominant mode, TE_{10}, is incident on the aperture [31]. When a small short-circuited dipole is placed close to the aperture side-wall, as shown in Figure 5.1(b), the electric field distribution becomes skewed with its peak shifted in the opposite direction away from the shorted dipole. A mirror distribution is obtained if the shorted dipole is placed at the other side of the aperture, as shown in Figure 5.1(c).
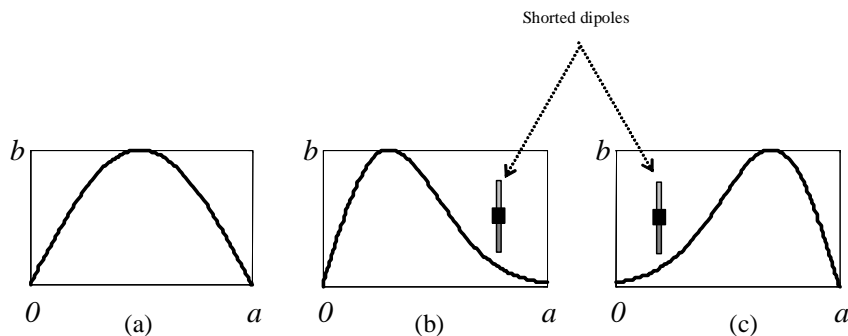
Figure 5.1. Aperture relative electric field magnitude distribution for (a) TE_{10} mode of unloaded waveguide aperture, (b) loaded aperture with shorted dipole placed toward the right aperture side, and (c) loaded aperture with shorted dipole placed toward the left aperture side.

It is important to note that the aperture fields shown in Figure 5.1 are for illustration purposes only since placing a dipole inside the aperture region not only changes the dominant mode distribution (as depicted in Figure 5.1(b) and (c)), but it might also cause higher-order modes to be generated. The actual field distribution in

the loaded aperture region will be obtained and shown later using full-wave numerical simulations.

In light of the above discussion, when two identical center-loaded dipoles are placed symmetrically inside the aperture region, two "mirror" electric field distributions can be synthesized by electronically controlling the loads of the dipoles. The dipoles, each of length l, are separated by a distance, s, along the broad aperture dimension, a, as shown in Figure 5.2(a). For the sake of explaining the idea, assume that the loads of the dipoles can be set electronically to an open or a short. The effect of these loads can be approximately realized in practice using PIN diodes to load the dipoles and turning them OFF or ON respectively [28], [65] as used in the prototype probe described later.

(a)   (b)
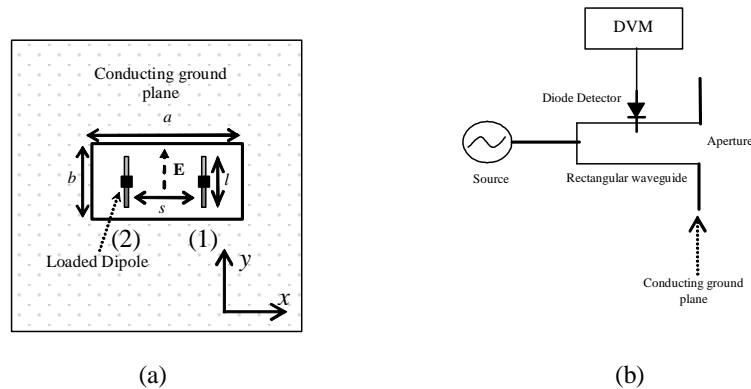
Figure 5.2. (a) A schematic of the dual-loaded aperture with two loaded dipoles, and (b) standing-wave probing device incorporating the dual-loaded aperture probe.

When one of dipoles is open-circuited and the other is short-circuited, the distribution is skewed toward the open-circuited dipole. The skew direction is reversed by the reversing the dipoles loading states. Both of the mirror distributions interact with their surroundings in a similar manner, and by switching between them during the scanning, i.e., turning one of them ON at a time through modulation, two signals

can be measured at any scan location. Effectively in this case, both aperture distributions are used to scan the SUT. Now, if the standoff distance varies along the narrow dimension of the waveguide aperture, b, the effect of this variation on the measured signal is independent of which distribution is turned "ON". This entails that the effect of standoff distance on signal measured while one of the distributions is turned "ON" is identical to its effect on the signal measured while the mirror distribution is turned "ON". Consequently, the undesired standoff variation effect can be compensated by subtracting the measured signals. It is also important to note that the scanning speed by which SUT is raster imaged is much slower than the speed by which the PIN diodes can be turned ON and OFF. Both signals are detected by a simple detector diode located at some prescribed distance along the probing waveguide and away from the aperture, as shown in Figure 5.2(b). The loaded dipoles are positioned such as to modulate the dominated mode aperture field. Due to the reflection at the aperture, a standing wave is formed inside the waveguide. The utilized diode detector produces a dc voltage proportional to the power of the total probed signal in the waveguide. The detector dc voltage is measured using typical Digital Voltmeter (DVM). Although using a standing-wave probing device makes the realization of the proposed probe simple, it is not the only implementation option. In fact, any coherent or non-coherent reflectometer-based detection system can be used in conjunction with this dual-modulated waveguide aperture probe. Similar to the differential probe proposed in [62], this method allows for 1D standoff distance compensation. However, it is possible to obtain 2D standoff compensation using the proposed method by synthesizing four aperture distributions. To this end, a different waveguide aperture shape such as a square aperture may be used [61].

5.2. SIMULATION RESULTS

Extensive electromagnetic numerical simulations were carried out to validate the concept behind the proposed probe, and to investigate various probe attributes such as the sensitivity and resolution as a function of its design parameters, i.e., the dipole inter-spacing, s, and dipole length l. For this purpose, CST Microwave Studio$^{\circledR}$ commercial simulation package was used [60]. A Ka-band (26.5-40 GHz)

probe with standard waveguide aperture ($a = 7.11$ mm, $b = 3.56$ mm) was considered for simulations.

5.2.1. Near-Field Distributions.   To validate the conceptual idea of synthesizing two mirror electric field distributions over a single aperture by using two identical loaded dipoles, the relative 2D electric field distribution (magnitude) over the waveguide aperture was computed when the waveguide is radiating into free-space at 33.5 GHz. Figure 5.3(a) shows the normalized electric field distribution for the unloaded waveguide aperture in dB. Figure 5.3(b) shows the aperture electric field distribution when it is dual-loaded with two dipoles each of length $l = 3$ mm and separated by $s = a/2$ (~ 3.56 mm) while one of them (dipole (2)) is short-circuited and the other one (dipole (1)) is open-circuited. As shown in Figure 5.3(b) the electric field distribution is skewed with its peak shifted toward the open-circuited dipole (dipole (1)). This effect is reversed when dipole (1) is short-circuited while dipole (2) is open-circuited as shown in Figure 5.3(c). Figure 5.3(d)-(f) show the electric field distribution computed 1 mm away from the aperture over an area of ~ 25 mm $\times$ 25 mm, i.e., larger than the aperture area, in the xy plane for the abovementioned loading conditions, respectively. By comparing Figure 5.3(d) to Figure 5.3(e)-(f), it is evident that the relative shift of the electric field pattern outside the aperture region follows the shift direction of the corresponding aperture fields. These results demonstrate the ability of synthesizing mirror near-field patterns using single waveguide aperture and two reversed aperture loading conditions.

5.2.2. Aperture Reflection.   In general, loading the waveguide aperture with two dipoles increases the aperture reflection compared to the unloaded aperture. To quantify this effect, the magnitude of the aperture reflection coefficient (Ka-band) when one of the dipoles was open-circuited and the other one was short-circuited is shown in Figure 5.4 for a dipole length of $l = 3$ mm and a dipole inter-spacing of $s = a/2$. Figure 5.4 reveals that the dual-loaded aperture structure behaves like a resonant circuit with very low Q-factor around the middle of the band due to the placement of the dipoles. To maximize the probe sensitivity it is desirable to operate at frequencies where the inherent aperture reflection is relatively small, e.g., in the range from 30-34 GHz for this case. Although not shown here, the aperture complex
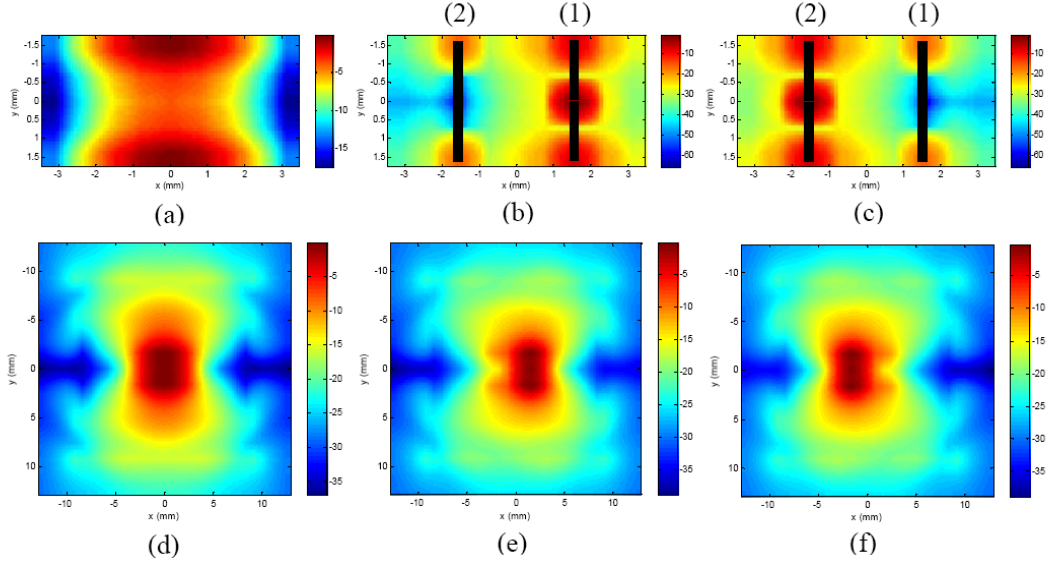
Figure 5.3. Aperture normalized electric field distribution in dB at 33.5 GHz for (a) unloaded aperture, (b) dual-loaded aperture when dipole (1) is open-circuited, (c) dual-loaded aperture when dipole (2) is open-circuited, and (d)-(f) the normalized electric field distribution 1 mm away from the apertures in (a), (b), and (c), respectively.

reflection coefficient (phase and magnitude) remains the same when the loading condition is reversed. Furthermore, the aperture reflection coefficient depends on both the length of the dipoles and their inter-spacing. Such dependency is illustrated in Figure 5.5 where the magnitude of the reflection coefficient is plotted as a function of the dipole inter-spacing (normalized to the aperture broad dimension, a, for different dipole lengths when one of the dipoles is open-circuited and the other one is short-circuited at a frequency of 33.5 GHz. As shown in Figure 5.5, the aperture reflection coefficient is relatively large for longer dipoles and smaller dipole inter-spacings. This is expected since, with small inter-spacing, the dipoles are located around the center of the aperture and consequently causes maximum field blockage and hence reflection. On the other hand, using very short dipoles results in smaller reflection coefficient with a weak dependency on the dipoles inter-spacing. Although utilizing very short dipoles seems attractive for this type of aperture design, using such small dipoles

does not cause sufficient change in the aperture reflection coefficient and the resulting signal might not be detected, as explained next.
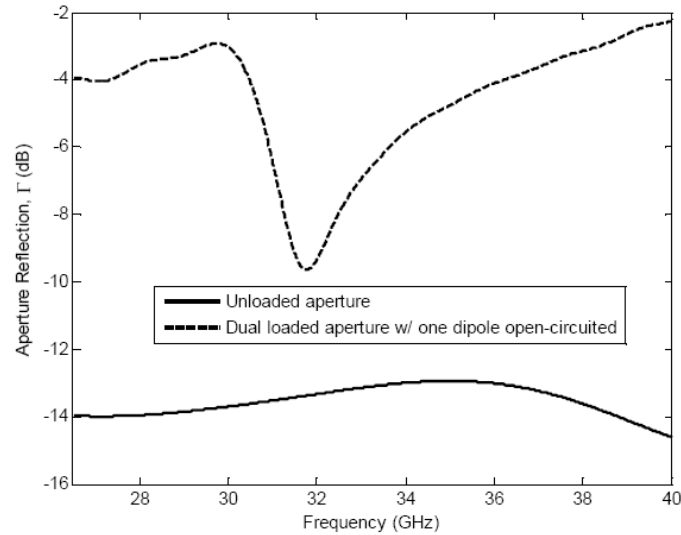
Figure 5.4. The magnitude of the aperture reflection coefficient for unloaded and dual-loaded Ka-band waveguide aperture (one dipole is open-circuited and the other is shorted).

As mentioned before, the design of the proposed probe is based on modulating the dual-loaded aperture to synthesize the required field distributions. At any given scan point; the modulation cycle is a result of applying two consecutive loading conditions. The first loading condition is when one of dipoles is open-circuited while the other one is short-circuited, and the second loading condition is when both dipoles are short-circuited. The relative change in the measured signal between these two conditions defines the so-called *reflection modulation depth*. The sensitivity of the proposed method is directly proportional to the modulation depth. Hence, it is desired to design the probe with maximum possible modulation depth. Figure 5.6 shows the reflection modulation depth as a function of dipoles inter-spacing for different dipole lengths at 33.5 GHz. In line with the above definition, the modulation depth curves shown in Figure 5.6 were computed as the absolute difference between the
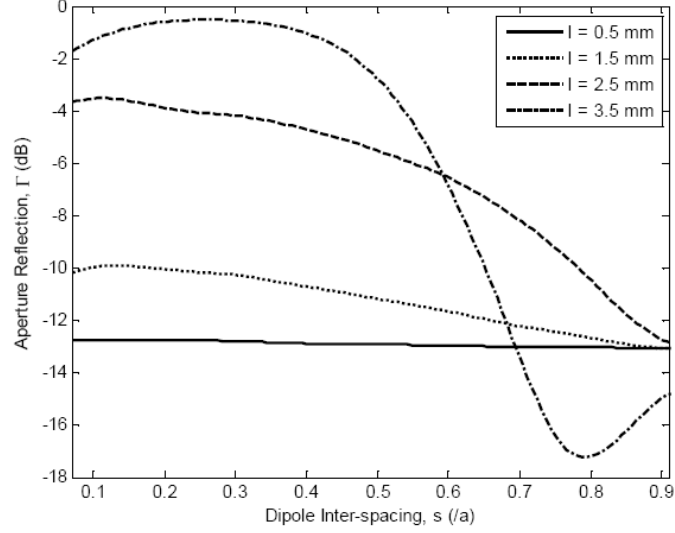
Figure 5.5. The magnitude of the aperture reflection coefficient for dual-loaded aper-
ture as a function of dipoles inter-spacing and lengths at 33.5 GHz (one
dipole is open-circuited and the other is shorted).

aperture reflections (in dB) resulting after applying the abovementioned consecutive
loading conditions while the aperture is radiating into free-space. It is evident from
Figure 5.6 that the maximum modulation depth is obtained for longer dipoles and
inter-spacing around $0.65a$. As shown in Figure 5.6, using very short dipoles results
in very small modulation depth (< 0.25 dB) and, consequently, the change in the
signal due to switching between the loading conditions might be hard to detect due
to the limited sensitivity of the typical diode detectors.

5.2.3. Differential Response. In an imaging process, the target interacts
with both of the synthesized near-field patterns/distributions. This interaction results
in two aperture reflections at any scan point. To simulate the actual probe voltage
response, each of the computed aperture reflections was converted to standing-wave
voltage via the relation, $V_i = C|1 + \Gamma_i e^{-j2\beta L}|^2$, where V_i and Γ_i ($i = 1, 2$) is the
standing-wave voltage and aperture complex reflection coefficient, respectively, when
the ith near-field pattern is switched "ON" (i.e., when the appropriate dipole is open-
circuited), is propagation constant, L is the distance between the detector location
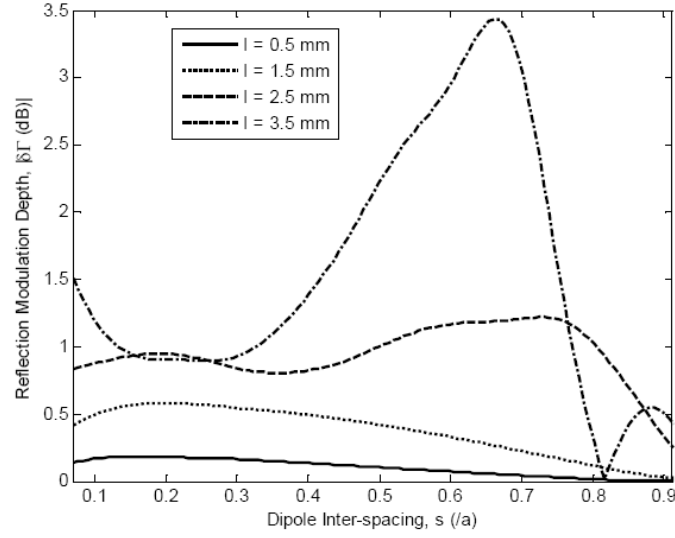
Figure 5.6. The reflection modulation depth for dual-loaded aperture as a function of dipoles inter-spacing and lengths at 33.5 GHz.

and aperture plane, C is a constant proportional to the detector diode power-voltage conversion coefficient and the source power, and β is propagation constant in the feeding transmission line, i.e., where the standing-wave is probed. The parameters L and C depend on the design of the standing-wave probing device, and they don't influence the basic operation of the proposed probe. Typical values for L and C, e.g., 30 mm and -0.035 V, respectively, were used in the simulations to predict the probe voltage response from the computed complex reflection coefficients.

To illustrate the differential probe response in imaging scenarios, a one dimensional (1D) scan of very thin and 20 mm long metallic wire aligned with the y-axis and placed at distance of 1 mm from the aperture was subsequently simulated. The diameter of the wire was set to 0.1 mm and its length was centered on the center of the aperture. The dipole lengths were 3 mm with dipoles inter-spacing of $s = 3.56$ mm. Figure 5.7 shows the probe voltage response when dipole (1) was open-circuited while dipole (2) was short-circuited, the reverse condition, and the voltage difference between these two conditions, i.e., the differential response. The results shown in Figure 5.7 were produced at 33.5 GHz. It is observed that when dipole (1) is open-circuited,

the field pattern shown in Figure 5.3(e) interacts with the target, and accordingly the target indication is shown to be shifted toward the location of dipole (1). The same applies for the case when dipole (2) is open-circuited where the field pattern shown in Figure 5.3(f) interacts with the target. Due to subtracting both responses, the differential response shows two indications for the target; high (positive) and low (negative). The distance between the highest and lowest points of the target indications is approximately equal to the dipoles inter-spacing as shown in Figure 5.7. Similar to the results reported in [62], the proposed differential probe produces target indications with odd symmetry around the center of the aperture.
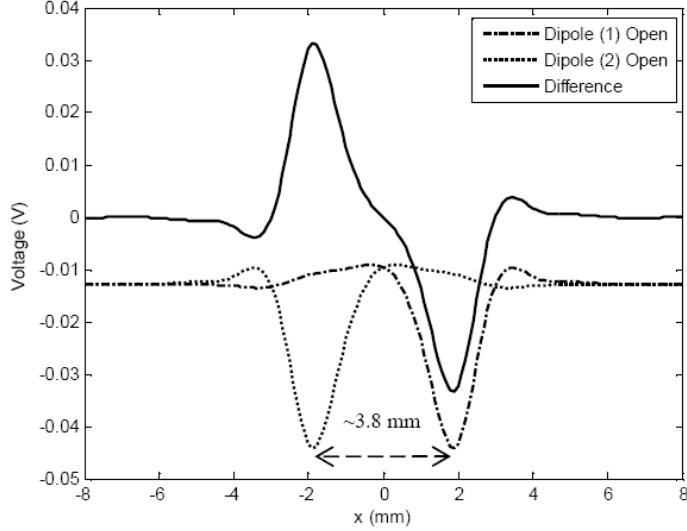
Figure 5.7. The simulated 1D scan of thin metallic wire at 33.5 GHz.

5.2.4. Probe Resolution. The probe imaging resolution is another critical attribute which was also investigated in-depth via simulations. The probe resolution is defined here as the minimum distance between two detectable targets for which the probe is capable of producing two distinct indications. Fig. 8 shows the simulated differential probe voltage response when the probe was used to scan two thin wires separated by distance $t_s = 1$ mm (Figure 5.8(a)), 2 mm (Figure 5.8(b)), and 5 mm

(Figure 5.8(c)). The wires were of diameter of 0.1 mm and a length of 20 mm, oriented along y-axis while placed 1 mm away from the aperture. The aperture dipoles, each with a length of $l = 3$ mm, were separated by $s = 3.56$ mm and the scan was produced at a frequency of 33.5 GHz as before. Again, it is observed that the probe response exhibits the typical differential odd symmetry. As shown in Figure 5.8(a), the probe was not able to individually resolve the targets when they were 1 mm apart. In fact, the obtained response for $t_s = 1$ mm is similar in shape to the response when a single target was scanned with the proposed differential probe (cf. Figure 5.7). The probe, however, started producing clear indications of the two targets when they were 2 mm apart as depicted in Figure 5.8(b). As the inter-spacing between the targets increased to 5 mm, the differential response produced two indications (high and low) for each target as shown in Figure 5.8(c).

Unlike the conventional open-ended waveguide probe near-field imaging resolution which is solely limited by the aperture broad dimension, a, the proposed differential probe resolution is a function of the two loaded dipole inter-spacing. In general, finer resolution can be obtained with small dipole inter-spacing. For illustration purposes, the proposed probe was used to scan the targets described above with $t_s = 2$ mm using dual-loaded aperture with dipoles inter-spacing $s = a/2$ and

(a)   (b)   (c)
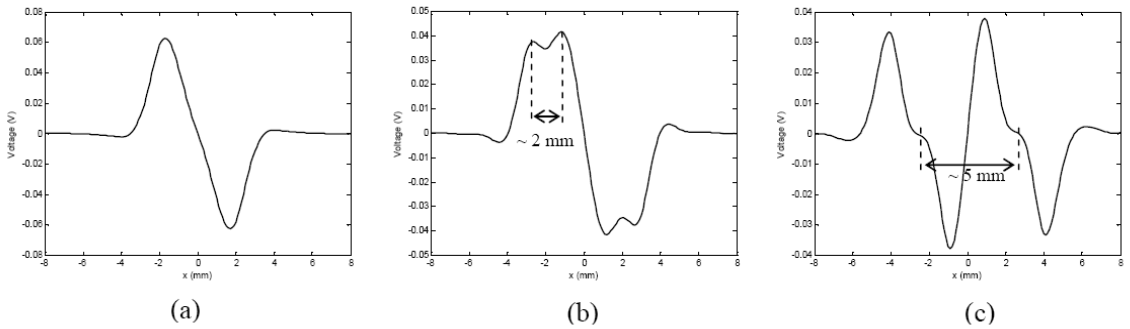
Figure 5.8. The simulated differential probe voltage response when the probe was used to scan two linear targets as function the targets inter-spacing at 33.5 GHz $(s = a/2)$.

$s = 3a/4$. Figure 5.9 shows the differential probe voltage response for these two dipoles inter-spacing.
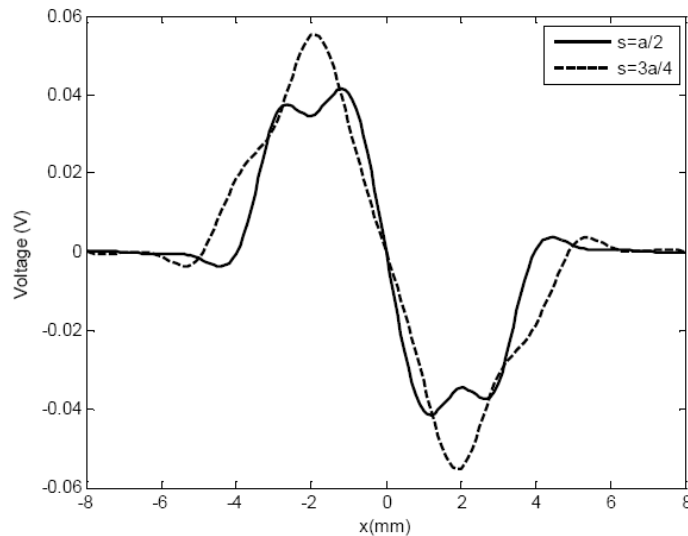
Figure 5.9. The simulated differential probe voltage response with $s = a/2$ and $s = 3a/4$ when the probe was used to scan two linear targets spaced by 2 mm at 33.5 GHz.

As shown in Figure 5.9, while the targets were not resolved when the dipoles inter-spacing was $s = 3a/4$, the probe with $s = a/2$ was capable of resolving both targets. It is important to note that the probe resolution, as opposed to its sensitivity, is not a function of the dipole length. Finally, it is also important to observe that the obtained resolution using the proposed probe as shown here is in fact finer than the one offered by the conventional open-ended waveguide probe. In the near-field, the spatial resolution obtained using open-ended waveguide imaging probes is lower bounded by half the probe aperture broad size, i.e., $a/2$ ($\sim$ 3.56 mm) [17]. On the

other hand, the proposed probe yielded a resolution of around 2 mm as indicated in the simulation results.

5.3. MEASUREMENT RESULTS AND DISCUSSION

As shown in Figure 5.2(a), the dipoles are aligned in parallel with the aperture dominant mode electric field polarization and used here as parasitic elements to synthesize the desired field distribution via controlling the loads electronically. To this end, PIN diodes are used to load the dipoles in practice. The desired distribution can be switched "ON" and "OFF" by forward and reverse biasing the appropriate diode, respectively. Typically, microwave and millimeter wave PIN diodes switch between forward and reverse states quite fast, e.g., in order of nanoseconds [49], and thus, the delay due to the switching time does not lengthen the overall scan time. With the developed probe, at least one modulation cycle is needed at each scan location to switch between the patterns. When using fast-switching millimeter PIN diodes as the ones used here, the modulation cycle width can be in the order of hundreds of nanoseconds. The total scan time can be approximated as, $T_{total} \approx N[t + t_m + t_a]$ where N is the total number of scan points, t is the time required to move the probe, t_m is the modulation cycle width, and t_a is the time required to acquire the data at each point. For typical scanning platforms and data acquisition cards, t and t_a are in orders of few milliseconds and hundreds of microseconds, respectively. Thus, the total scan time is in fact dominated by those two components and not the diode switching time.

5.3.1. Prototype Probe Construction. To demonstrate the efficacy of the proposed probe experimentally, a Ka-band prototype probe was manufactured and tested. Standard Ka-band rectangular waveguide aperture with printed dipoles was fabricated using a two-layer 0.508 mm thick printed circuit board (PCB) with Rogers-4350 substrate material ($\varepsilon_r = 3.48$ and loss-tangent of 0.004). The aperture was etched out on both sides of the PCB and the ground planes were connected by small vias around the aperture. The substrate was sufficiently thin such that it does not impact the aperture reflection significantly. The dipoles, each of length of 3 mm and width 0.25 mm, were printed on the top layer of the PCB and placed symmetrically about the center of the aperture with inter-separation distance of $s = 3a/4$ (~ 5.3

mm). The dipoles were loaded by two identical flip-chip PIN diodes (0.7 mm × 0.38 mm) [49] controlled by dc bias lines (0.25 mm wide). The bias lines were routed through the top ground plane. In the aperture region, the bias lines were routed such that they were orthogonal to the dominant mode electric field polarization, and hence their perturbing effect was minimized. The used PIN diodes needed 1.45V to switch between the reverse the forward states. When reverse biased, the diode represents a capacitive load of ∼ 25 fF, and in the forward state it is equivalent to 5-Ohm resistive load. The used PIN diodes switch in less than 5 ns, and hence the modulation frequency can be as high as 200 MHz. Additionally, 5-pF small surface-mount (SMT) capacitors (0.5 mm × 0.25 mm) were used to realize an RF return path to ground (short-circuit) for any signal that might couple into the dc bias lines, and thus preventing any spurious radiation or resonances that could result from such coupling. Figure 5.10 shows a magnified picture for the top layer and the modulated aperture components. The aperture was fed from the bottom layer side by a Ka-band rectangular waveguide with a standing-wave probing device as shown in Figure 5.2(b).
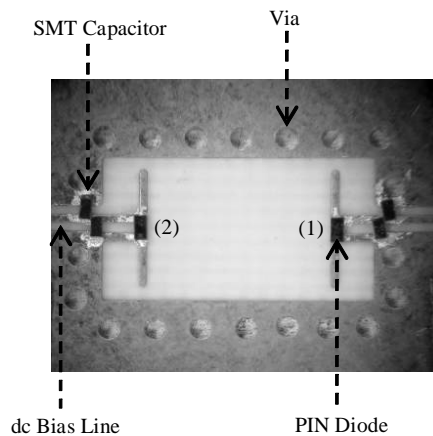
Figure 5.10. Magnified picture of the manufactured prototype Ka-band dual-loaded aperture.

5.3.2. Modulated Response. The symmetry in probe response as the diodes are switched/modulated is critical for proper probe operation. The probe

should produce identical responses for the reversed aperture loading conditions when it radiates into a medium with no lateral spatial variations. The response symmetry was tested first by measuring the aperture complex reflection coefficient using a vector network analyzer and then by modulating both diodes while the aperture is radiating into free-space. Figure 5.11 shows the measured complex reflection coefficient when diode (1) was ON while diode (2) was OFF and vice versa.
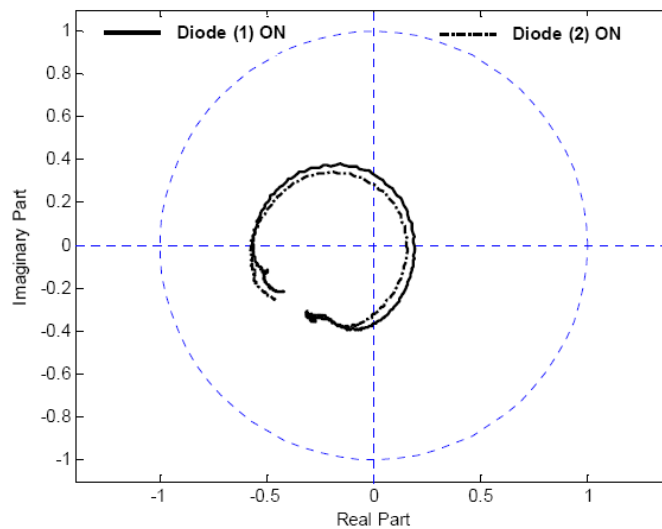
Figure 5.11. The dual-loaded aperture complex reflection coefficient over the Ka-band for both diode states.

As depicted in Figure 5.11 the reflection measurements for both states are very close. The discrepancies between the measurements for the two modulation states are mainly attributed to the physical differences of the diodes and their biasing structures. Such discrepancy is marginal and will not impact the overall probe symmetry when the standing-wave measurement device is used as shown next.

Figure 5.12 shows the measured standing-wave voltage over 5 modulation cycles for both diodes while the probe was operating at 33.5 GHz. As shown in Figure

5.12, the response in the ON and OFF states for both diodes is almost identical. This in turn validates the symmetry exhibited in the probe design.
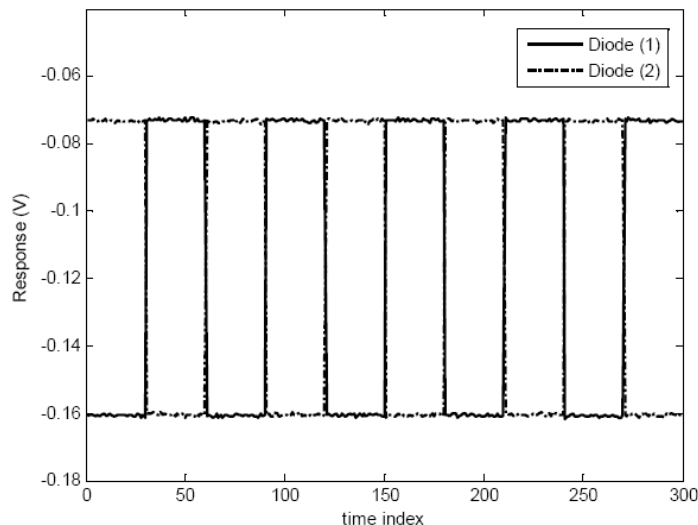
Figure 5.12. The modulated response for both diodes at 33.5 GHz.

5.3.3. Response to Standoff Distance Variations. To examine the response of the proposed probe to standoff distance variations, a conducting plate was placed flush against the aperture of the waveguide and subsequently moved away gradually in the direction normal to the aperture, as depicted schematically in Figure 5.13(a). Figure 5.13(b) shows the measured standing-wave voltage as a function of standoff distance normalized to free-space wavelength (λ) at 33.5 GHz. The three traces in Figure 5.13(b) correspond to the cases when the first diode was ON while the second diode was OFF, when the first diode was OFF while the second one was ON, and the voltage difference between these two states. The response due to the first two cases is rather typical for this type of measurements, i.e., standing-wave voltage measurements, using single aperture probe [1]. Furthermore, these two cases resulted in almost identical voltage responses, as expected. Therefore, the voltage

difference between these states, i.e. the differential response, shows minimal varia-
tions with standoff distance, e.g., around 10 mV peak-peak. It is also apparent that
the compensation range extends beyond one wavelength. The differential response
exhibits small peaks at about every $\lambda/2$ as depicted in 5.13(b). Because the dipoles
and their loads are not perfectly identical, the phases of the reflection coefficients
for both loading conditions are slightly shifted with respect to each other. Due to
this inherent phase shift, the standing wave corresponding to each loading condition
will be slightly shifted with respect to the other one. Hence, the difference between
the responses of both loading conditions will not be identically zero. This effect is
prominently manifested as peaks shown about every $\lambda/2$ in the differential response
since the phase of the reflected signal jumps around $\pm180^o$ at these points. Similar
behavior was also observed for the coherent differential probe proposed in [62].
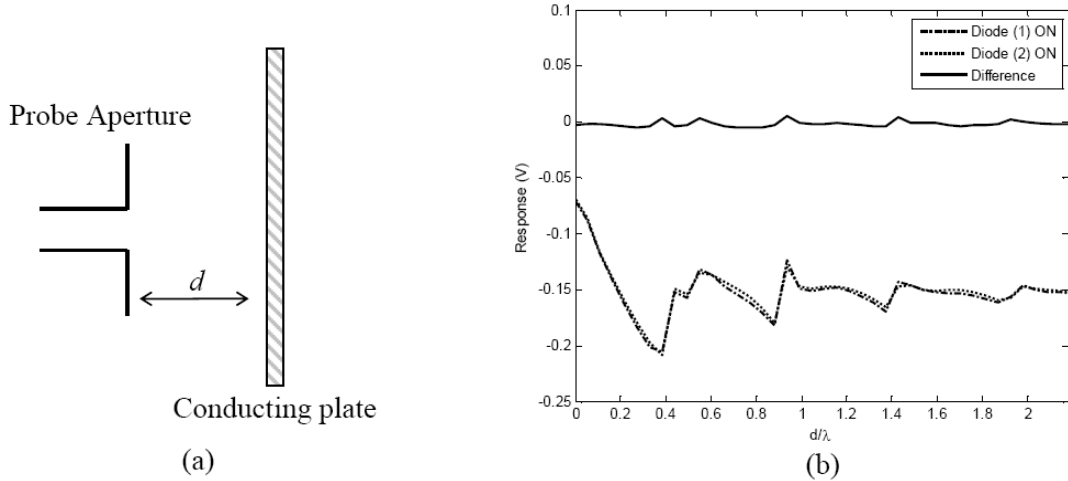
Figure 5.13. (a) Standoff distance variation experimental setup, and (b) measured
standing-wave voltage as a function of the normalized standoff distance.

5.3.4. 1D Scans. Before using the proposed probe for imaging localized
targets, it is important that the prototype probe response is well-understood. For
this purpose, the probe was used to produce linear scans of thin metallic wire at

33.5 GHz. Figure 5.14(a) shows a schematic for the cross-section of the target-probe experimental setup. The wire was much longer than the aperture narrow side b. The diameter of the wire was 0.5 mm, and it was located at fixed standoff distance of 1 mm from the aperture. Figure 5.14(b) shows the obtained linear scans. It is observed that the scans obtained with both modulation states (diode (1) was ON while diode (2) was OFF, diode (1) was OFF while diode (2) was ON) are symmetric around the aperture center (the aperture broad side center coincides with $x = 30$ mm). Each of these line scans is shifted slightly from the aperture center. This observation experimentally confirms the applicability of the approach to synthesize two symmetric field distributions by using a single aperture. In addition to the main lobe, the linear scans with both states show small side lobe near the position of the open-circuited dipole. In near-field imaging, these side lobes are expected to interact with imaged target as well. The differential linear scan shown in Figure 5.14(b) was obtained as the difference between the linear scans for both modulation states. As such, it shows odd symmetry around the aperture center. That is the target indication is two-sided; high (positive) and low (negative) as it was observed in the simulation results. Consequently, in 2D images, a target will be manifested by two colors, e.g. black and white in gray scale images as it will be shown later. It is also interesting to visualize the probe response to 2D target with width comparable to the dipoles inter-spacing. Figure 5.15 shows the linear scan obtained for a thin copper strip of width ~ 6.25 mm placed 1 mm away from the aperture with its length along the y-axis. Again, the strip was much longer than the waveguide narrow dimension. Due to the interaction of both strip edges with the probe, the target indication is not as simple as in the thin wire case. Each strip edge results in two mirror indications as shown by the differential response in Figure 5.15.

5.3.5. 2D Scans. To highlight the utility of the proposed probe for near-field imaging, it was used to image small cylindrical hole (~ 2 mm in diameter and ~ 2 mm deep) in a metallic plate while the plate was slanted with large angle (to simulate severe standoff distance variation). For comparison purposes, the same hole was imaged using a conventional single-aperture standing-wave probe [1]. Figure 5.16(a)-(b) show the obtained images at 33.5 GHz using the conventional probe and the dual-loaded differential probe, respectively. While the indication of the hole is
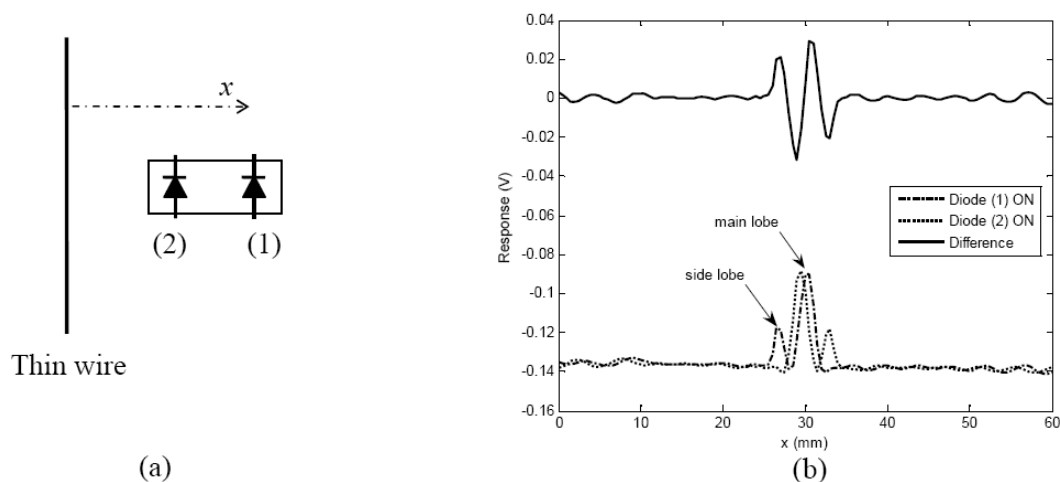
Figure 5.14. (a) A schematic for the cross-section of the target-probe experimental setup, and (b) the obtained 1D scan of thin metallic wire at 33.5 GHz.

faint and almost masked by the standoff distance variations in the image produced using the conventional probe, it is clearly visible in the differential probe image. The latter image clearly shows the utility of this approach for near-field microwave and millimeter wave imaging. The odd symmetry observed in the linear scans is also shown in the image obtained by the differential probe. Therein, the indication of the hole is both the brightest white and darkest black regions in the center of the image. The odd symmetry applies also for the probe aperture side lobes which interact with the hole as well. The side lobe effect is shown in Figure 5.16(b) as concentric rings. The odd symmetry response attributes of the proposed differential probe is in fact similar to that of the coherent differential probes [62].

Finally, to clearly define the scope of application, Table 5.1 summarizes the major advantageous and disadvantages of the proposed probe and compares between the various developed differential probes and compensation methods.

5.4. SUMMARY

Near-field millimeter wave techniques have been effectively used for nondestructive testing (NDT) and imaging applications over a decade. The interaction of
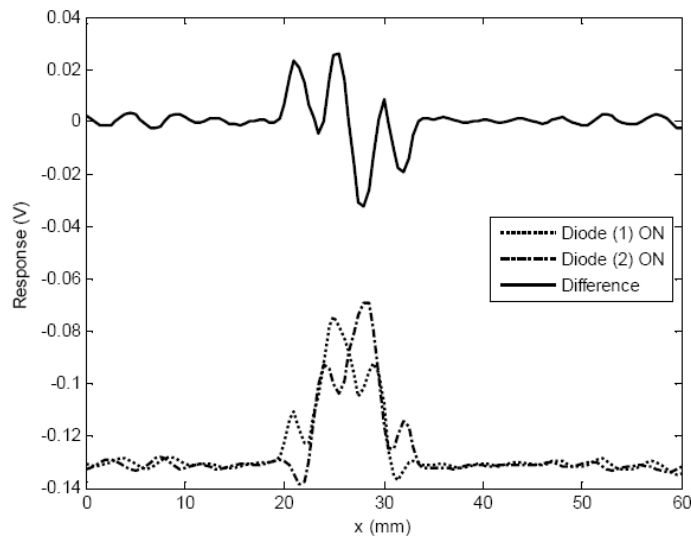
Figure 5.15. 1D scan of thin copper strip of width 6.25 mm obtained at 33.5 GHz.

Table 5.1. Comparison between various differential probes and compensation methods.

Probe	Advantages	Disadvantages
In-Contact Compensator [24]	simple, 2D compensation	needs calibration, in-contact, compensation $<\lambda/4$
Dual-Polarized Probe [61]	simple	needs calibration, special structures, compensation $<\lambda/4$
Modulated Aperture Probe (proposed)	simple, easily optimized, high-resolution, compensation$>\lambda$	switching delay
Dual-Aperture Probe [62]	compensation$>\lambda$	relatively complex

the fields and a structure under test (SUT) in the near-field of a probe is more complex than that of the far-field interaction. In the near-field, the distance between the probe and the SUT, referred to as standoff distance, is an important measurement parameter and when optimally chosen it can significantly improve detection sensitivity.
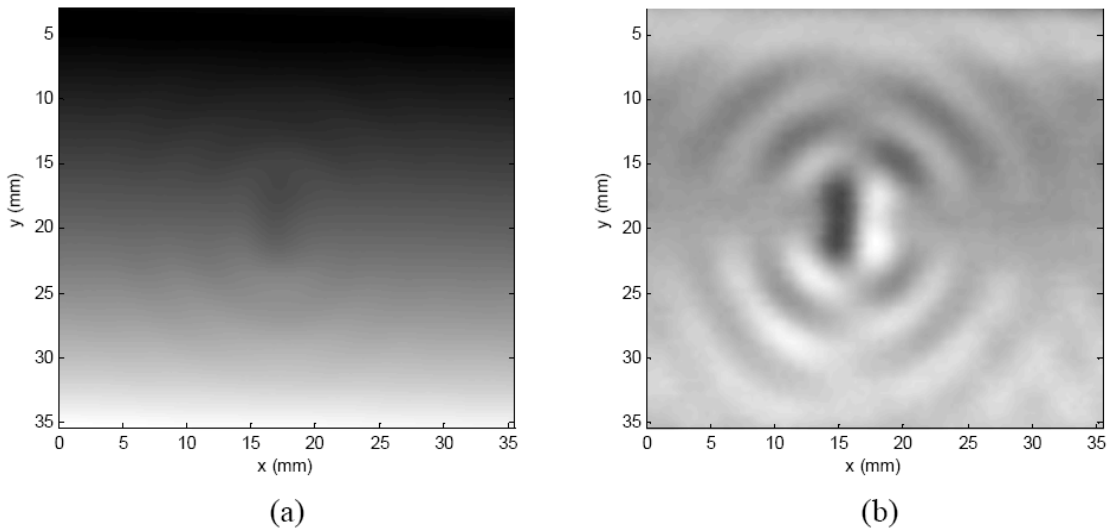
Figure 5.16. Images of small hole in slanted conducting plate as obtained using (a) conventional standing-wave probe, and (b) using the proposed differential probe.

However, undesired changes in this parameter can adversely influence the detection outcome to the extent that a target may be totally masked. Consequently, in the past several different methods and remedies have been proposed to eliminate or drastically reduce this adverse influence, each with its own limitations.

Herein, a novel microwave and millimeter differential probe which operates in a differential mode and is capable of automatically eliminating undesired changes in standoff distance during near-field imaging was designed based on dual-loading and modulating a single waveguide aperture. The proposed probe was shown to combine the attractive features of the coherent and non-coherent probes; versatility and simplicity, in a compact design. The idea behind the proposed probe; synthesizing two mirror electric field distributions through dual aperture loading, was verified via simulations and experiments. Extensive numerical simulations were performed to study the design parameters which impact the probe sensitivity and resolution.

A Ka-band prototype probe was designed and tested experimentally. The symmetry of the probe design was confirmed and the probe response to standoff distance variations was investigated as well. It was shown that the proposed probe efficiently

reduces the standoff distance variations based simple non-coherent detection. Scanning 1D target verified the basic principle of synthesizing two symmetric aperture field distributions using single waveguide aperture dual modulated by loaded dipoles. Furthermore, the linear scans provided insight into the expected response when the probe was subsequently used for 2D scans. The image obtained for a localized target in severe standoff distance variations setup demonstrated the potential of the proposed probe for near-field microwave and millimeter wave imaging. The various features in the obtained image were in-line with observations drawn from the simulation results as well as the experimental linear scans. With the proposed approach, 2D standoff distance compensation using a rectangular aperture with two diodes might be feasible by processing two additional modulation states; both diodes OFF/ON. This scheme, along with using square waveguide aperture, should be the subject of future investigations.

6. NOVEL AND SIMPLE VECTOR NETWORK ANALYZER (VNA)

Microwave and millimeter wave (300 MHz-300 GHz) vector network analyzers (VNAs) are testing instruments used to perform vector/complex signal measurements, i.e., magnitude and phase. Nowadays, VNAs are critically in demand for many applications encompassing circuit characterization, reflectometry, imaging, and material characterization to name a few. They are also utilized in various emerging biomedical as well as promising industrial applications involving nondestructive testing (NDT). Furthermore, they are necessary and important academic laboratory instructional tools. However, the high cost (in excess of several tens of thousands to several hundreds of thousands of dollars) and complexity of the currently available commercial VNAs have put them prohibitively out of the financial reach of many users. Consequently, there is a great need for an alternative VNA system that is not only capable of addressing these established and emerging needs, but is also relatively inexpensive, less complex, portable, more user friendly while providing unique optional features that can expand its realm of utility.

High performance VNAs are the most prominent measurement instruments used to characterize circuits and devices at RF, microwave, millimeter wave and sub-millimeter wave frequencies [66], [67]. The VNA is designed to measure vector scattering parameters, i.e., the complex reflection coefficient, of a device-under-test (DUT) connected at its test port, without disturbing the waves at that port, i.e., without changing the electric and magnetic fields distributions over the cross-section of that port. Therefore, the actual signal measurements within the VNA are typically performed at another location or port, and subsequently, the vector parameter at the test port is inferred or calculated from these measurements [68]. This is the major distinction between the low-frequency and high-frequency measurement techniques.

In general, vector network analyzers can be realized based on coherent and non-coherent detection schemes. A VNA with coherent detection scheme measures the in-phase and quadrature components of the complex signal reflected at or transmitted through the test port. This is accomplished by utilizing a tuned-receiver, e.g., heterodyne receiver, architecture [69]. Nowadays, commercial VNAs operating based on this detection scheme are the most developed instruments for high frequency

vector measurements. Since typical tuned-receiver detection schemes are inherently narrowband in nature, e.g., narrowband IF stage, these VNAs usually offer large measurement dynamic range and very low noise floor [69]. However, the high complexity and cost associated with implementing the tune-receiver, i.e., the need for highly stable phase-locked sources, limits the utility of such VNAs in many applications where simple, handled, and relatively inexpensive high-frequency *in-situ* vector measuring devices are needed.

On the other hand, automatic VNA systems based on non-coherent detection offer relatively inexpensive and simple alternative to the tuned-receiver VNAs. With non-coherent detection, the complex signal magnitude and phase are inferred from simple power measurements. Multi-probe [70], [71], six-port [68], [72], and multi-state [73] reflectometers are among the pioneering designs upon which VNA designs based on non-coherent detection schemes were realized. The measurement dynamic range of these systems is limited by the relatively low dynamic range of a power detector, which for these purposes is commonly a diode detector. However, this range can be extended using phase modulation and locked-in amplifier [74]. Many automatic VNA systems based on these reflectometers have been proposed and successfully implemented in the past, with a recent system described in [75]. All of the designs mentioned above are fundamentally based on utilizing multiple power detectors connected to multi-port junctions, i.e., hybrid couplers, which necessitates multi-step characterization and calibration procedures [76].

A simple non-coherent detection-based VNA design using a single power detector and a set of perturbation-two-port (PTP) networks was proposed in [77]. The PTP approach is based on using a set of perturbation networks inserted between a DUT and a scalar network analyzer. The complex reflection coefficient of the DUT is calculated from the magnitude of the reflection coefficient measured by the scalar network analyzer using a given set of PTP networks [77].

This section introduces a novel and simple non-coherent detection-based VNA which utilizes a single power detector and an electronically-controllable phase shifter inserted between a DUT and a standing-wave probing device [78]. Subsequently, the magnitude and phase of reflection coefficient of the DUT, Γ, are uniquely determined from standing-wave voltages measured at three or more phase shift settings. Given

the phase shifter characteristics at these settings are known, the proposed VNA can be fully calibrated with only three standards loads, i.e., known reflections. The phase shifter can be characterized by measuring its scattering parameters either using an independent VNA or using this same VNA in conjunction with a characterization procedure involving a set of known standards.

Unlike the PTP approach, the proposed VNA design does not require a scalar network analyzer. Using a single power detector and avoiding the use of a scalar network analyzer and multi-port hybrid junctions by performing standing-wave measurements are the main unique aspects of the proposed VNA. These aspects significantly reduce the proposed VNA complexity compared to the previously proposed non-coherent detection-based VNAs. Given the current advanced state of small electronically-controllable phase shifter designs, implementing the proposed novel VNA design yields accurate, wideband, robust, handheld, relatively inexpensive and high-performance measurement device that may be used for a variety of diverse applications.

This section describes the design of the proposed VNA and demonstrates its accuracy for complex reflection coefficient measurements. Subsequently, the VNA performance is investigated via simulations considering various critically important system parameters such as the number of phase shift settings, relative phase shifts, characteristics of the phase shifter as well as detector noise. Moreover, the experimental attributes of an X-band (8.2-12.4 GHz) prototype system are presented based on a commercially-available off-the-shelf electronic phase shifter. The measurement accuracy associated with the prototype VNA is then compared to that of an Agilent HP8510C VNA.

A Ka-band handheld prototype VNA based on custom-designed phase shifter is also described and its measurement accuracy is benchmarked against an Agilent E8364B performance network analyzer (PNA). To demonstrate the developed VNA

capabilities in imaging applications, the Ka-band prototype is used to produce phase and magnitude images of a test radome panel.

6.1. BACKGROUND

The basic theory behind the proposed VNA is based on the standing-wave measurement using the conventional slotted transmission line technique shown in Figure 6.1. The backward traveling reflected wave from the DUT connected at the test-port (TP) is combined with the forward traveling incident wave (from the isolated source) to form a standing-wave in the transmission line. Subsequently, a diode detector, located a distance z from the TP, produces a dc voltage proportional to the standing-wave power at that location. To measure the complex reflection coefficient of the DUT, Γ, the diode detector is moved along the line and the measured diode voltage is recorded (the line has a longitudinal slot to allow such movement). While the magnitude of the reflection coefficient is thereafter computed from the measured voltage standing-wave ratio, i.e., maximum to minimum, its phase is determined from the displacement of the measured standing-wave pattern along the line relative to the pattern measured when a reference load with known reflection such as a short-circuit is connected at the TP [66]. Assuming the frequency of operation is known precisely, three standing-wave voltage measurements are needed with this technique; the maximum and minimum voltages with the DUT, and the reference voltage with a short-circuit, e.g., the minimum. This process involves the movement of the probe along the transmission line to measure the maximum and minimum voltages [66].

The slotted-line technique for measuring the complex reflection coefficient, although simple, is inconvenient for automation, i.e., it requires mechanical movement of the probe. In the past, many automated VNA systems based on the slotted line technique were proposed. The six-port reflectometer design with multiple detectors placed along the transmission line to sample the standing wave pattern at different locations was proposed to realize an automated version of the slotted line technique [70], [79], [80] as shown in Figure 6.2. In the multi-probe technique, a minimum of three fixed detectors are placed along the line and used to measure the standing-wave voltages $\{V(z_1),\ V(z_2),\ V(z_3)\}$. When the inter-spacing between these detectors is less than half-of-wavelength, the DUT complex reflection coefficient can be uniquely
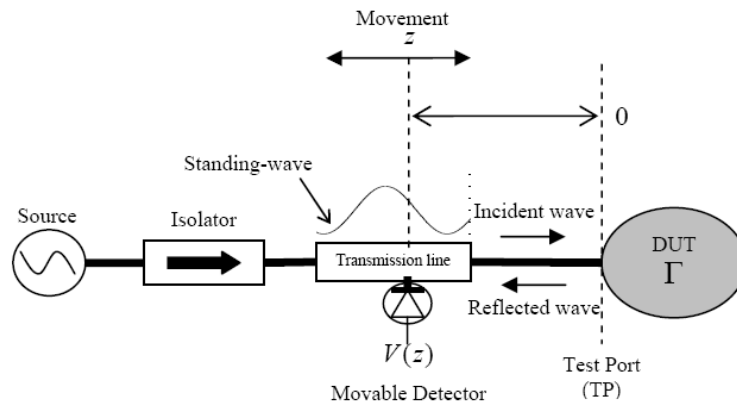
Figure 6.1. Slotted-line technique for measuring DUT complex reflection coefficient, Γ.

determined using the measured voltages [70], [80]. This technique has shown limited utility for wideband VNA implementations due to two fundamental drawbacks associated with its design. First, using multiple detectors not only accounts for additional complexity, but also necessitates involved calibration routines which may result in ill-conditioned solutions for the calibration constants [76]. Furthermore, all three detectors should be always biased in the square-law region, i.e., where their produced voltage is proportional to the standing-wave power. Given that different detectors have different characteristics in practice, separate response linearization might be needed for each individual detector [81]. Second, due to the stringent restriction on the detectors physical inter-spacing, i.e., they have to be within half-of-wavelength apart, the multi-probe technique with three probes is intrinsically limited to an octave of bandwidth, and more than three detectors should be used to extend its bandwidth [80].
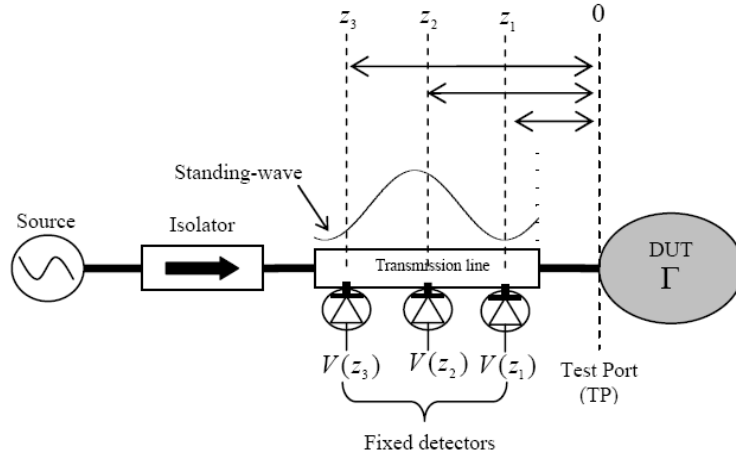
Figure 6.2. The multi-probe technique for measuring DUT complex reflection coefficient, Γ.

A simpler and easy-to-calibrate VNA can be designed with one detector as presented next.

6.2. PROPOSED VNA DESIGN

The developed VNA is founded on inserting an electronically-controllable phase shifter between a simple standing-wave probing device and a DUT, as shown in Figure 6.3. The standing-wave probing device consists of a transmission line (TL), e.g., a straight waveguide section, with a probe attached to a diode detector. The reflected wave from the DUT is then combined with the incident wave to form a standing-wave in the TL. Subsequently, a diode detector located at a fixed distance L along the TL produces a dc voltage proportional to the standing-wave power at that location. In this configuration, the phase shifter is used to electronically "move" or shift the standing-wave pattern with respect to the detector location, and hence obtain the pertinent reflection information without the need to move the detector itself as in the slotted line method [66] or use multiple detectors along the transmission line as in some realizations of six-port reflectometers [71], [79], [80].

6.2.1. System Concept. Assuming the diode detector is biased in the square-law region, the measured standing wave voltage as a function of the phase
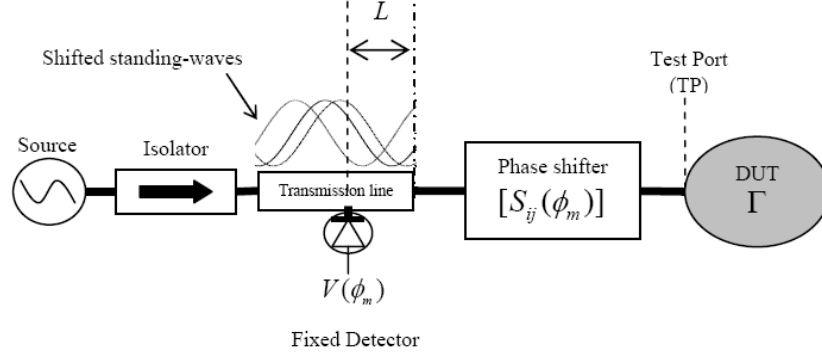
Figure 6.3. A schematic diagram of the proposed VNA.

shift ϕ_m introduced by the phase shifter is modeled by,

$$V(\phi_m) = C \left| 1 + S(\phi_m)e^{-2j\beta L} \right|^2 , \tag{87}$$

where is C a constant proportional to the incident power and the diode detector characteristics, $\beta = 2\pi/\lambda_g$ and λ_g are the propagation constant and the wavelength in the TL, respectively, and,

$$S(\phi_m) = S_{11}(\phi_m) + \frac{S_{11}(\phi_m)S_{21}(\phi_m)\Gamma}{1 - S_{22}(\phi_m)\Gamma} \tag{88}$$

is the effective reflection coefficient referenced to the output port of the TL after accounting for the scattering characteristics (S-parameters) of the phase shifter, i.e., $\{S_{ij}(\phi_m),\ i = 1, 2,\ j = 1, 2\}$.

The S-parameters of the phase shifter are assumed to be known either from system characterization procedure or prior independent measurements using a VNA. The latter option is particularly appealing with stable phase shifters since the measured S-parameters can be saved and later used during system operation. Similarly, the propagation constant, β, detector location along the line, L, and constant C are assumed to be known from system characterization. Hence, the only remaining unknown in (87) is the sought-after DUT reflection coefficient, Γ. Several phase shifts, $\{\phi_m,\ m = 1, 2, \ldots, M\}$, and their corresponding measured standing-wave voltages,

$\{V(\phi_m),\ m = 1, 2, \ldots, M\}$, are used to formulate a system of nonlinear equations which can be subsequently solved, i.e., using Gauss-Newton method, to determine Γ. For example, Figure 6.4 shows the actual (simulated) and calculated complex DUT reflection coefficient obtained using the proposed procedure for $L = \lambda_g/4$, $C = -1$ (negative diode detector polarity is assumed), with an ideal phase shifter, i.e., $\{S_{11}(\phi_m) = S_{22}(\phi_m) = 0,\ S_{12}(\phi_m) = S_{21}(\phi_m) = e^{j\phi_m},\ \forall\ m\}$, and three phase shifts of $\{\phi_1 = 0,\ \phi_2 = 10^o,\ \phi_3 = 20^o\}$. As shown in Figure 6.4, the obtained solution for Γ, based on using the three standing-wave voltages produced by the three phase shifts, very closely matches the actual DUT reflection used for the simulation.
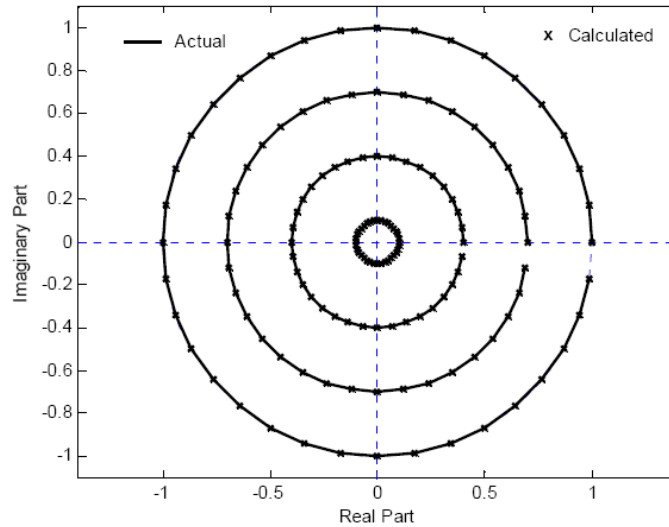
Figure 6.4. Actual and calculated DUT reflection coefficient based on standing-wave voltages and three phase shifts (noise-free).

For system design, it is important to find the minimum number of phase shifts, M, required to uniquely calculate the complex reflection coefficient of the DUT from the voltage measurements in (87). Assuming that the discrete phase shifts are a means to sample the standing-wave pattern along the line, the minimum number of phase shifts required to accurately recover the standing-wave pattern from its samples,

and consequently the reflection information, is essentially dictated by the Sampling Theorem [54]. The standing-wave pattern is periodic with a period equal to half of the wavelength in the TL, $\lambda_g/2$. If we were to sample the standing-wave pattern using the phase shifter and a single detector, the minimum number of samples (phase shifts) is determined by Nyquist rate [54]. Accordingly, the minimum sampling rate required to reconstruct the standing-wave pattern of period $\lambda_g/2$ should be greater than $4/\lambda_g$. This results in at least four samples for every λ_g along the TL. Since the distance λ_g in the TL corresponds to a total phase shift of 2π radians, the sampling rate should be greater than $2/\pi$. Assuming relative phase shift interval of π radians ($V(\phi_m)$ is periodic with a period of π), the minimum number of required phase shifts is given by,

$$M > 2 \implies M_{\min} = 3 \tag{89}$$

This result is analogous to the requirement of using at least three power detectors spaced along line to insure proper sampling of the standing-wave in multi-probe transmission line methods [71], [80]. It is also interesting to notice that, as mentioned before, at least three voltage measurements are needed with the slotted-line method.

6.2.2. Calibration. In practice, the obtained DUT complex reflection coefficient after solving the nonlinear equations involving the phase shifter characteristics and the corresponding standing-wave measurements might not be accurate due to various imperfections in the measurement system, i.e., reflections due to connector mismatch, losses in the TL, etc. (these were not accounted for in the model given in (87)). The effects of such imperfect hardware can be modeled collectively as *systematic errors* which in turn can be calibrated out from the measured DUT reflection coefficient, and hence enhancing the measurement accuracy.

To reduce the effects of systematic errors, the proposed VNA can be calibrated using the conventional three-term calibration procedure used with traditional four-port reflectometers [82]. Following this procedure, a fictitious error adapter representing three systemic errors is inserted between the test port and the phase shifter. The three error parameters are determined from the measured effective complex reflection coefficient of three standard (known) loads. For this purpose, a termination, short, and offset short loads are used as the standard or calibration loads. The effective complex reflection coefficient, measured at the output port of TL, for each

standard load connected at the test port is found after solving the set of nonlinear equations involving the phase shifts and the corresponding standing-wave voltages. Subsequently, the measured DUT reflection coefficient is corrected based the obtained error terms [82].

6.2.3. Features. With three phase shifts, the resulting system of nonlinear equations is in fact over-determined since the complex reflection coefficient represents two unknowns only (real and imaginary parts of Γ). Hence, these equations can also be simultaneously solved to obtain C. Additional phase shifts may also be used to solve for other unknowns if needed, e.g., detector location, and more importantly, increase the measurements accuracy through coherent averaging using many phase shifts produced via simple electronic control. Consequently, the effects of the unreliable standing-wave pattern measurements near standing-wave nulls, and detector noise can be significantly reduced.

Unlike the multi-probe techniques which are bandwidth-limited due to the fixed relative placement of the detectors, the proposed design does not impose any restriction neither on the placement of the detector nor on the values of the phase shifts for wide-band coherent reflectometry measurements. In general, the performance of the proposed VNA depends on the following factors;

- detector noise level,

- phase shift interspacing,

- number of phase shifts,

- DUT reflection coefficient, i.e., low and high reflection coefficients,

- quality of the phase shifter, i.e., return and insertion losses,

- detector characteristics, and

- repeatability in producing the phase shifts.

The effect of the first five factors will be examined further shortly. The effect of the detector characteristics will not be addressed herein. The detector is assumed to produce a dc voltage proportional to the standing-wave power, i.e., operating in

the square-law region. Deviations from this norm can be usually corrected using known methods [81]. The phase shift settings should be repeatable in order to obtain consistent measurements. To this end, the used phase shifter characteristics should remain constant over the course of the measurements. Phase shifters with highly repeatable phase shift settings are very common nowadays.

6.3. SIMULATION RESULTS

The capability of the proposed VNA to accurately measure various DUT reflection coefficients in the presence of measurement noise, i.e., detector noise, was investigated via simulations. A VNA system with $L = \lambda_g/4$ and $C = -1$ was considered to illustrate the operation of the proposed VNA without the error adapter. The effect of detector noise was simulated by adding independent and identically distributed random noise terms to the voltages computed from the standing-wave model as per (87) before calculating the DUT reflection coefficient, Γ. The noise terms were modeled as samples of Gaussian random process with zero mean and standard deviation, σ, representing the detector noise root-mean-squared (RMS) value. Figure 6.5 shows the actual and calculated DUT reflection coefficient, Γ, with an ideal phase shifter producing three phase shifts of $\{\phi_1 = 0, \phi_2 = 10^o, \phi_3 = 20^o\}$, based on noisy standing-wave voltages ($\sigma = 1$ mV) . As shown in Figure 6.5 and when compared with the noise-less results shown in Figure 6.4, it is clear that the DUT reflection coefficient was uniquely determined even in the presence of detector noise. Average performance metrics, i.e., root-mean-squared error, will be used next to quantify the errors introduced due to noise.

6.3.1. Phase Shift Interspacing. Theoretically speaking, the interspacing between the phase shifts can be arbitrarily small and yet an accurate estimate of the DUT reflection coefficient may still be obtained. However, due to the noise contaminating the detected voltage, the spacing between the phase shifts, within a relative phase shift interval of π, affects the accuracy of the measurement results. Extensive simulations were performed to study the effect of phase shift interspacing and noise RMS on the accuracy of the obtained DUT reflection coefficient. For instance, consider measuring a DUT reflection coefficient of $\Gamma_{actual} = 0.5e^{j\pi/4}$ using the proposed system with $M = 3$ equally-spaced phase shifts in the interval from 0
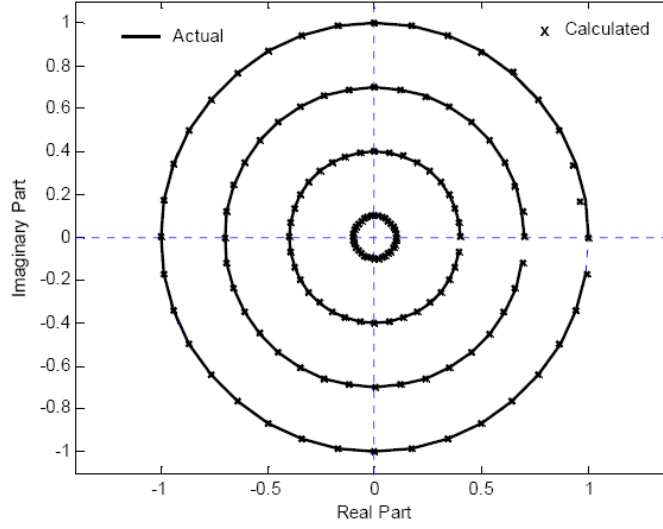
Figure 6.5. Actual and calculated DUT reflection coefficient based on noisy standing-wave voltages and three phase shifts (noise RMS of 1 mV).

to π. The phase shifts were $\{\phi_1 = 0,\ \phi_2 = \delta\phi,\ \phi_3 = 2\delta\phi\}$, where $\delta\phi$ is the phase shift interspacing (in degrees) such that $\delta\phi < 90^o$. Several noise RMS values and phase shift interspacing were considered, and the magnitude and phase average root-mean-squared error (RMSE) relative to the actual (simulated) DUT reflection coefficient were computed for combinations of noise RMS value and phase shift interspacing. The RMSE for magnitude and phase are defined, respectively, as,

$$\text{Magnitude RMSE} = \sqrt{\frac{1}{N}\sum_{i=1}^{N}\left(|\Gamma_i| - |\Gamma_{actual}|\right)^2}, \tag{90}$$

$$\text{Phase RMSE} = \sqrt{\frac{1}{N}\sum_{i=1}^{N}\left(Angle\{\Gamma_i/\Gamma_{actual}\}\right)^2}, \tag{91}$$

where Γ_i is the computed DUT reflection coefficient at the ith simulation run. A total of $N = 10000$ simulation runs with different noise realizations were used to estimate the average magnitude and phase RMSE. The RMSE is used here as a *figure-of-merit* to quantify the uncertainty in phase and magnitude measurements

due to the detector noise only. Analysis of other typical sources of measurement uncertainties such as connection repeatability and calibration standards accuracy is beyond the scope of this investigation (such uncertainty analysis requires precisely known traceable standards which are not available at disposal currently).

Figure 6.6(a)-(b) show the RMSE for magnitude and phase, respectively, as a function of the phase shift interspacing for different noise RMS values using an ideal phase shifter with $M = 3$. The results show magnitude and phase RMSE values less than 0.01 and 1°, respectively, at $\delta\phi = 10^o$ can be achieved with noise RMS value as high as 10 mV. For $\delta\phi < 10^o$, the RMSE for magnitude and phase decrease rapidly and monotonically as the phase shift interspacing decreases for all noise levels. A marginal decrease in the RMSE performance is observed after increasing the phase shift interspacing beyond $\delta\phi = 10^o$ (RMSE performance remains within the order of the magnitude attained at $\delta\phi = 10^o$). It is also apparent that the RMSE performance degrades linearly as a function of noise RMS value increases.
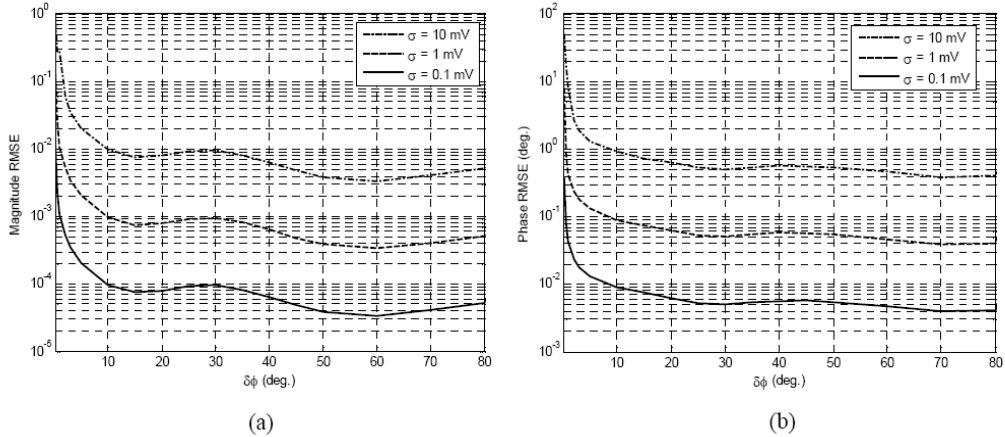
Figure 6.6. (a) Magnitude and (b) phase RMSE as obtained using the proposed VNA with $M = 3$ as a function of the phase shift interspacing for different noise RMS values.

6.3.2. Number of Phase Shifts. As the minimum number of discrete phase shifts was established earlier, it becomes important to study the improvement in the

performance of the system when more than three phase shifts are used to calculate the DUT reflection coefficient. Figure 6.7(a)-(b) show the RMSE for magnitude and phase, respectively, as a function of the number of phase shifts for different noise levels with $\delta\phi = 10^o$ for the same system parameters and DUT used above. For all noise levels, increasing the number of phase shifts results in decreasing the RMSE for both magnitude and phase. An increase beyond 8 phase shifts only marginally improves the performance. The linear relationship between the noise RMS value and the RMSE for magnitude and phase is also manifested in these results.
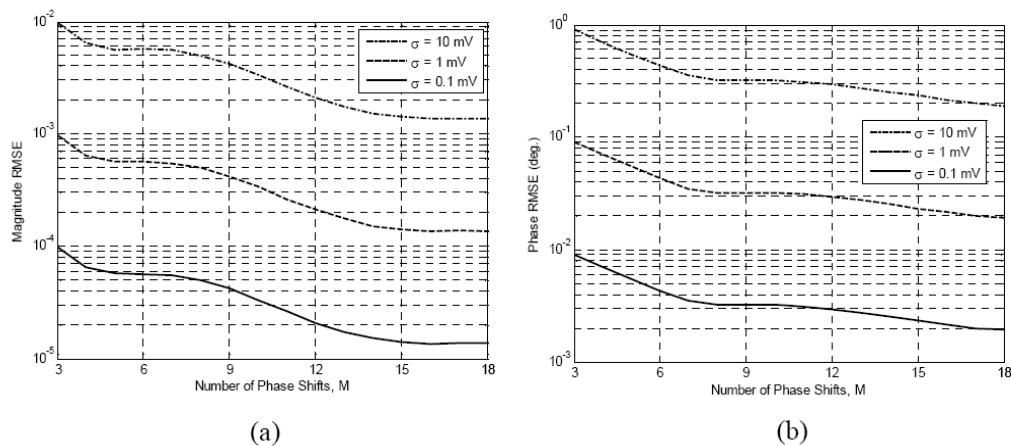
Figure 6.7. (a) Magnitude and (b) phase RMSE as obtained using the proposed VNA as a function of the number of phase shifts for different noise RMS values, $\delta\phi = 10^o$.

6.3.3. DUT Reflection Coefficient. Since the probed standing-wave voltage dynamic range changes as a function the magnitude of the DUT reflection coefficient, $|\Gamma|$, the accuracy of the computed reflection coefficient is also dependent on $|\Gamma|$. Typical magnitude RMSE, for three phase shifts and $\delta\phi = 10^o$, as a function of $|\Gamma|$ for different noise RMS values are shown Figure 6.8(a). The RMSE curves shown in Figure 6.8(a) were normalized to the actual magnitude of the DUT reflection coefficient (such that they become directly related to the percentage error). The

normalized RMSE is relatively high for low DUT reflections. For such low reflections, the standing-wave pattern is almost flat, and consequently the anticipated changes in the standing-wave voltage as a function of the phase shifts can be easily masked by system noise. On the other hand, high DUT reflections cause sharp nulls in the standing-wave pattern. Reliable detection of changes in the standing-wave voltage around these nulls in the presence of noise is always problematic. Relatively better performance is obtained for the middle reflection values between these two extremes, as expected. For $0.1 < |\Gamma| < 0.8$, the phase RMSE is almost linear as a function of , as shown in Figure 6.8(b).
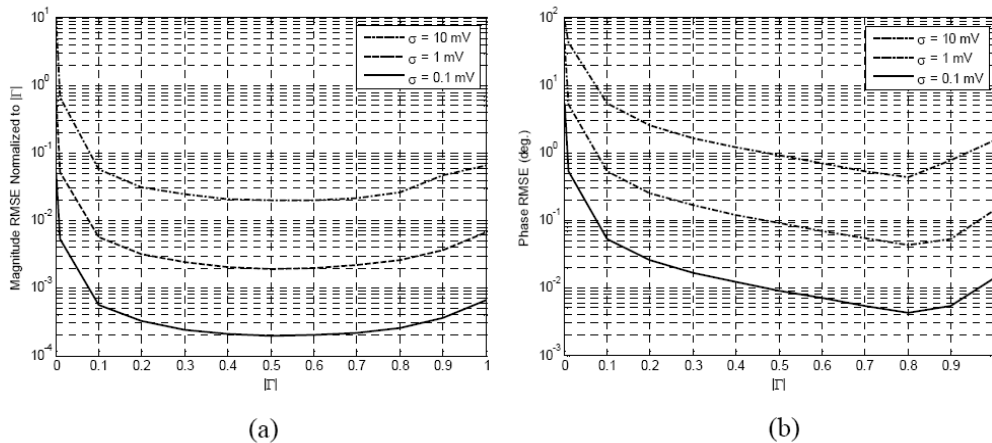
Figure 6.8. (a) Normalized magnitude and (b) phase RMSE as obtained using the proposed VNA as a function of the magnitude of the reflection coefficient, $M = 3$, $\delta\phi = 10^{o}$.

6.3.4. Phase Shifter Quality. Thus far, the analyses and the corresponding results were for an ideal phase shifter. However, non-ideal phase shifter characteristics, such as input port return loss (RL_i), insertion loss (IL), and output port return loss (RL_o), also alter the standing-wave pattern, and consequently influence the performance of the proposed VNA. To highlight this effect, the performance of the proposed VNA when using a non-ideal phase shifter characterized by $RL_i = 10$ dB, IL = 8 dB, and $RL_o = 20$ dB was simulated. These values were chosen since they

closely match corresponding mid-band values of an X-band phase shifter used to construct the prototype VNA, and it will be described later. Figure 6.9(a)-(b) show the magnitude normalized RMSE and phase RMSE, respectively as function of $|\Gamma|$. The high insertion loss of the phase shifter reduces the standing-wave voltage dynamic range, and hence, the accuracy with the non-ideal phase shifter is in general lower compared to when an ideal phase shifter is considered (see Figure 6.8), as expected. The effect of standing-wave nulls on the accuracy of determining high DUT reflections is also reduced in this case since the insertion loss in the phase shifter significantly reduces these nulls. Consequently, the RMSE decreases monotonically as a function of increasing $|\Gamma|$.
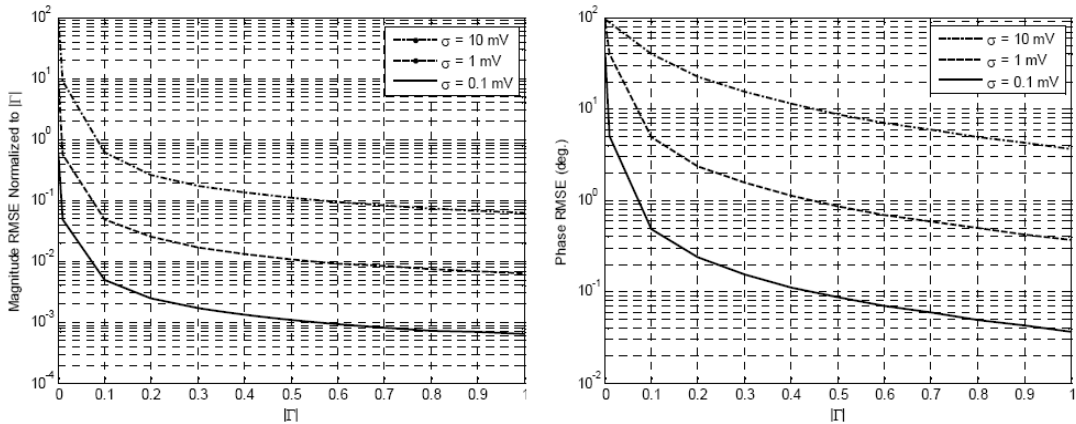
Figure 6.9. (a) Normalized magnitude and (b) phase RMSE as obtained using the proposed VNA with non-ideal phase shifter as a function of the magnitude of the reflection coefficient, $M = 3$, $\delta\phi = 10^o$.

Collectively, the simulation results show that the detector noise and the characteristics of the phase shifter have profound effect on the performance of the proposed VNA, and therefore must be properly accounted for. The uncertainties in measuring the magnitude and phase of the DUT reflection coefficient change linearly with increasing noise RMS value. Hence, it becomes imperative to use low noise power detectors and acquisition systems in order to obtain accurate measurement results.

Coherent averaging, using multiple sets of phase shift, can be implemented to reduce the combined effect of noise and reduction in voltage dynamic range due the losses in the phase shifter, as it will be shown later.

6.4. X-BAND VNA PROTOTYPE

An X-band (8.2-12.4 GHz) automated VNA prototype, as depicted in Figure 6.10, was constructed and tested. The standing-wave device consisted of a straight section of an X-band rectangular waveguide and a zero-biased Schottky diode detector. The output power of the sweep oscillator was set such that the diode detector operated in the square-law region for all frequencies within the band. Since the corresponding detector output voltage is low in that region, a low-noise instrumentation amplifier was used to amplify the output voltage.
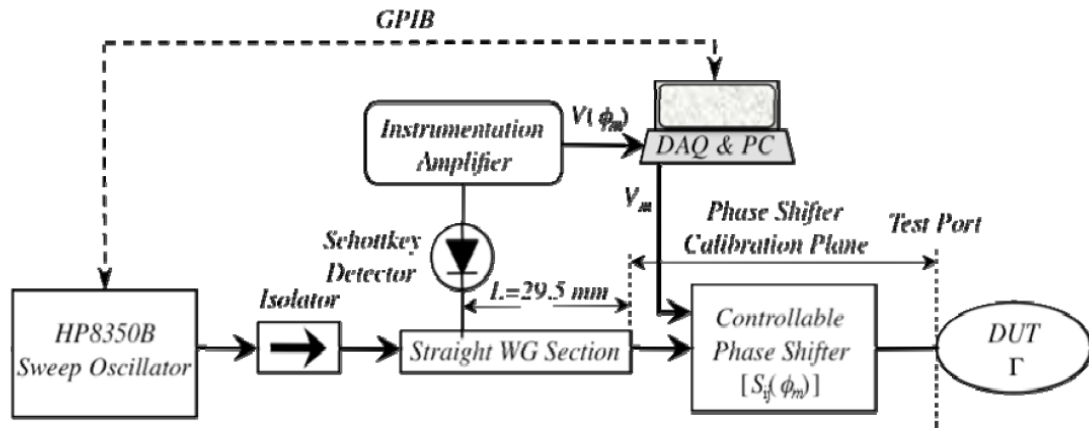
Figure 6.10. Schematic diagram of the X-band prototype VNA system.

A commercially available electronic phase shifter (controllable by a variable dc input voltage) was used in this implementation. The S-parameters of the phase shifter (in between the calibration planes shown in Figure 6.10) were measured over the X-band using an Agilent HP8510C VNA and subsequently incorporated in the calculation of Γ, as per (88).

The phase shifter input return loss, output return loss, and insertion loss are around 10 dB, 20 dB, and 8 dB, respectively at the center frequency of 10.3 GHz. The phase shifter provides relative phase shift of around 140° and 90° at the beginning and toward the end of the band, respectively in response to control voltages, V_m, ranging of 0.4-1.2 V. Voltage steps of 0.1 V were used to control the phase shifter in that range, i.e., total of 9 discrete phase shifts. Each 0.1 V results in a phase shift of $\sim18^o$ and $\sim10^o$ at the beginning and toward the end of the band, respectively.

The system was calibrated using a short, 0.902 cm offset-short, and a matched load as calibration standards. In solving for the error terms, the standards were assumed to be ideal and they were also used to calibrate the Agilent HP8510C VNA for comparison purposes. To account for any source and/or amplifier drifts during the course of the measurements, the constant C was computed simultaneously with the complex reflection coefficient during the measurement of the calibration standards as well as the DUT. Automation of the swept measurements was accomplished through a PC with fast data acquisition (DAQ) card and a GPIB control link. The detection system noise RMS value was estimated to be around 4 mV.

Figure 6.11(a)-(b) show the measured complex reflection coefficient of a variable DUT using the HP8510C and the proposed VNA at a frequency of 10.3 GHz. The variable DUT consisted of a variable phase shifter and an attenuator terminated with a short which allowed synthesis of various complex reflection coefficients with $0.028 < |\Gamma| < 0.78$ (-2 to -31 dB) and wide range of phase values. While all HP8510C measurements were conducted with an internal averaging factor of 16, i.e., averaging internal system noise only, the proposed VNA measurements were the results of coherent average of four different sets of phase shifts, each consisting of $M = 3$ phase shifts (cf. Table 6.2 for the control voltages in each set). As shown in Figure 6.11(a)-(b), the results of measurements obtained using the proposed VNA are in excellent agreement with their counterparts obtained using the HP8510C VNA.

Referenced to the HP8510C VNA measurements, Table 6.1 list the average absolute error in phase and magnitude measurements as obtained using X-band VNA for different $|\Gamma|$. As shown in Table 6.1, the average absolute magnitude error in the proposed VNA measurements ranged from a minimum of 7.68×10^{-4} (for $|\Gamma| = 0.028$, 2.77% error) to a maximum of 0.018 (for $|\Gamma| = 0.708$, 2.52% error). On the other

(a)   (b)
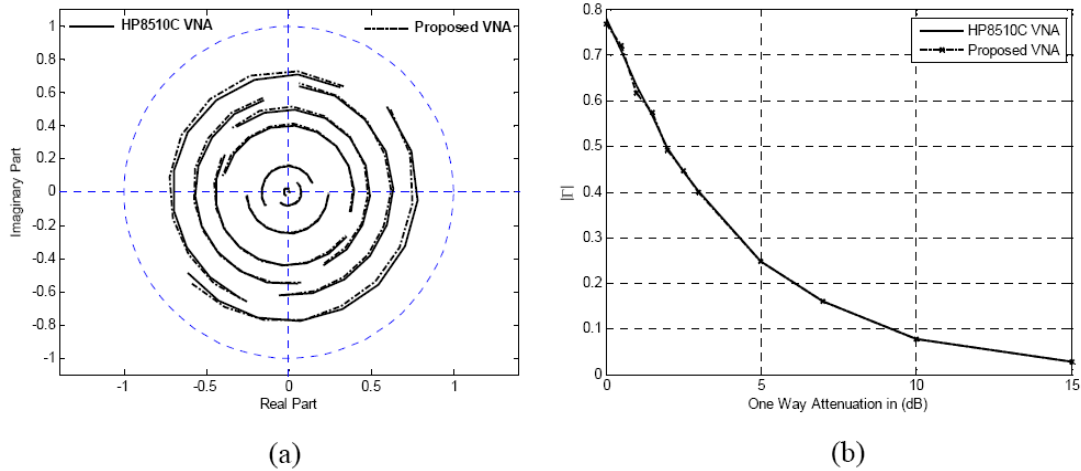
Figure 6.11. Measured DUT reflection coefficient using HP8510C VNA and the proposed VNA, (a) real and imaginary parts of Γ, and (b) $|\Gamma|$ as a function of the DUT one-way attenuation.

hand, average absolute phase error in the range 0.69^o (for $|\Gamma| = 0.401$) and 2.54^o (for $|\Gamma| = 0.708$) was observed, respectively. Most of the magnitude and phase average errors are actually within the measurement uncertainties of the HP8510C VNA [83].

Table 6.1. The average absolute error in phase and magnitude measurements as obtained using the X-band VNA prototype.

$|\Gamma|$	Absolute Error in Magnitude (deg.)	Absolute Error in Phase (deg.)
0.780	0.016	1.92
0.708	0.018	2.54
0.634	0.012	1.10
0.566	0.008	2.46
0.497	0.010	1.02
0.444	0.005	2.34
0.401	0.007	0.69
0.248	0.002	1.48
0.160	0.001	1.67
0.078	8.3×10^{-4}	1.56
0.028	7.7×10^{-4}	2.25

It is important to note that the utilized electronic phase shifter quality is far from ideal, i.e., it presents high insertion loss resulting in a two-way attenuation of ~16 dB. Nevertheless, the high measurement accuracy demonstrated with this phase shifter is attributed to the capability of performing coherent averaging of the complex reflection coefficient measurements obtained using different and multiple sets of phase shifts. This effect was also studied by performing measurements with different sets of phase shifts each with phase shifts for the same DUT described earlier. Table 6.2 lists the phase control voltages corresponding to each phase shift set used in this study.

Table 6.2. The utilized phase shifter sets with the X-band VNA prototype.

Number of Sets	Set Control Voltages V_m, (V)
1	$\{0.4, 0.5, 0.6\}$
2	$\{0.4, 0.5, 0.6\}, \{0.6, 0.7, 0.8\}$
3	$\{0.4, 0.5, 0.6\}, \{0.6, 0.7, 0, 8\}, \{0.8, 0.9, 1.0\}$
4	$\{0.4, 0.5, 0.6\}, \{0.6, 0.7, 0, 8\}, \{0.8, 0.9, 1.0\}, \{1.0, 1.1, 1.2\}$

Figure 6.12 shows the RMSE for the phase and magnitude of the measured complex reflection coefficient using the proposed VNA with one set of phase shifts, and averaging the results of two, three, and four different sets. The RMSE values were computed with respect to the HP8510C VNA measurements, i.e., the HP8510C VNA measurements were used as Γ_{actual} in (90) and (91). As shown in Figure 6.12, using one set of phase shifts did not yield accurate phase and magnitude results. However, coherent averaging of the measurements obtained using two sets of phase shifts enhances the performance significantly. Marginal improvement was obtained by averaging the results of three and four sets of phase shifts. With four sets of phase shifts, the maximum magnitude RMSE (normalized to $|\Gamma|$) was ~0.03 (for $\Gamma| = 0.028$) and a maximum phase RMSE was obtained 2.83^o (for $|\Gamma| = 0.708$), as shown in Figure 6.12.

The proposed VNA was used to perform swept frequency measurements of an arbitrary unknown DUT and the results were compared to those obtained with the HP8510C VNA. Figure 6.13 shows the magnitude and phase of the DUT complex
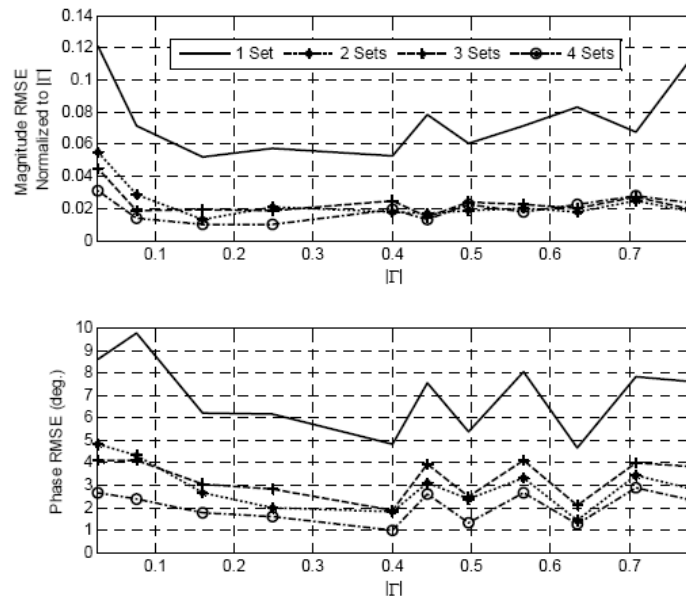
Figure 6.12. Magnitude RMSE normalized to $|\Gamma|$ (top) and phase RMSE (bottom) as a function of with averaging over different number of phase sets, $M = 3$.

reflection coefficient measurements over the entire X-band frequencies. The proposed VNA results were the average of the measurements obtained with four sets of phase shifts as used before. As indicated in Figure 6.13, the proposed VNA measurements closely match those of the HP8510C VNA. The proposed VNA results presented in Figure 6.13 are raw measurement results corresponding to 51 frequency points in the band without any smoothing.

The proposed VNA produced highly consistent and repeatable complex reflection coefficient measurements as observed from testing the system repeatedly over long periods of time with different calibration runs. The sensitivity of the proposed VNA to changes in the phase shifter characteristics was investigated as well. Repeated measurements of the phase shifter characteristics showed that they remain fairly constant over time (almost 18 months), and consequently, the performance of the proposed VNA remains robust. In fact, the used phase shifter was characterized five months before taking the measurements presented here. Finally, It is emphasized that higher measurement accuracy can be potentially obtained with the proposed
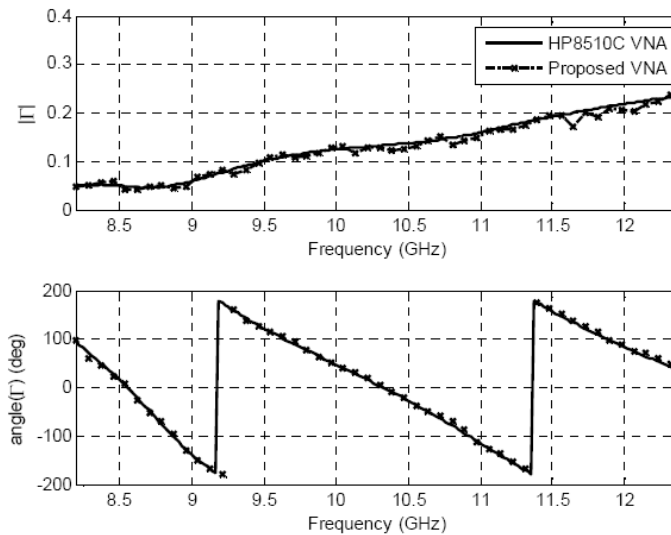
Figure 6.13. Magnitude (top) and phase (bottom) measurements of an X-band DUT obtained using HP8510C and the proposed VNAs.

VNA design when a phase shifter of higher quality, i.e., smaller insertion loss, is used. To this end, one may design and use a wideband phase shifter in-line with some of most recent and interesting coupled line design appearing in [84]

6.5. KA-BAND VNA PROTOTYPE

A Ka-band (26.5-40 GHz) VNA system based on the proposed approach was designed and customized to be used in millimeter wave imaging at 35.5 GHz. To facilitate *in-situ* imaging and inspection, the design requirements included that the VNA should be accurate, robust, handheld, battery operated, and relatively inexpensive. To meet these requirements, the designed Ka-band VNA including the phase shifter was completely waveguide based. A variable, electronically-controlled Ka-band waveguide-based phase shifter was designed specifically for this VNA. The phase shifter design is described next.

6.5.1. Phase Shifter Design. Microwave and millimeter electronically tunable phase shifters are essential control components in phased array/beam-forming sub-systems needed in radars and wireless communications systems. They are also

used extensively in high-frequency test equipment. In general, microwave and millimeter electronically tunable phase shifters can be designed based on the basic principles of loaded/coupled transmission lines, switched delay lines, and reflection [85], [86]. At low microwave frequencies; loading, coupling, switching, and generating the reflection needed for these phase shifter designs can be realized using simple designs based on active discrete components, i.e. PIN diodes, field-effect-transistor (FET) switches, varactor diodes, transmission lines, and couplers. Such simple designs based on discrete components are difficult to be implemented directly at millimeter frequencies. Besides the high loss associated with these components, the wavelength becomes much shorter relative to the circuit dimensions (thus small unintentional dimension variations results in high undesirable performance degradation). Consequently, at millimeter wave frequencies, either distributed phase control is implemented, e.g., using substrates of variable dielectric constants, band-gap effect, etc., or the circuit dimensions are reduced using integrated technology. Towards the latter end, phase shifters are designed using monolithic microwave integrated circuit (MMIC) technology where the phase shifter circuit including all control components are integrated on a single semiconductor substrate (reduces the form-factor significantly). Replacing some of the control components, i.e., FET switches, with micro-electro-mechanical-system (MEMS) based components in the MMIC phase shifter design is the current dominant trend in millimeter phase shifter designs (reduces losses at the expense of the control speed) [87]. On other hand, millimeter wave variable phase shifters can be designed based on ferrites and ferro-electric materials (recent 20 GHz and 30 GHz designs appears in [88]).

Unlike X-band and low-frequency microwave phase shifters, commercial, off-the-shelf, relatively inexpensive, and electronically-controlled millimeter wave phase shifters were not available in the market at the time when the need for the Ka-band VNA arose. To realize such system a waveguide-based Ka-band shifter had to be custom designed using commercially available PIN diodes.

The phase shifter design presented here is based on sub-resonant slots cut into the wall of a waveguide. Loading the slots with active elements such as PIN diodes for example and thereafter controlling the loads electronically can provide highly stable and distinctive phase shifts. The only requirement on the slots is to be sub-resonant

so that they do not radiate efficiently or cause high reflections (in effect, they don't distort the standing-wave in the waveguide once the phase shifter is used). Following this concept, the phase shifter can be designed to provide desired fine setting of the signal phase with minimum insertion and return losses as it will be shown later.

Figure 6.14 shows a generic example of a waveguide phase shifter design following the above description. It consists of two rows of longitudinal sub-resonant slots loaded with PIN diodes. The slots are cutout into a printed circuit board (PCB) forming the broad wall of a rectangular waveguide. Descriptions of the various phase shifter design parameters are given Table 6.3. Ma-com MA4GFCP910 flip-chip high-frequency flip-chip PIN diode was used to load the slot [49]. This PIN diode is similar to the one used in the previous sections except that its reverse-bias capacitance is a bit lower, i.e., 18 fF. Turning each PIN diode ON and OFF using control dc bias voltage provides control over the phase shift values. In this sense, this phase shifter can be regarded as digitally controlled phase shifter.
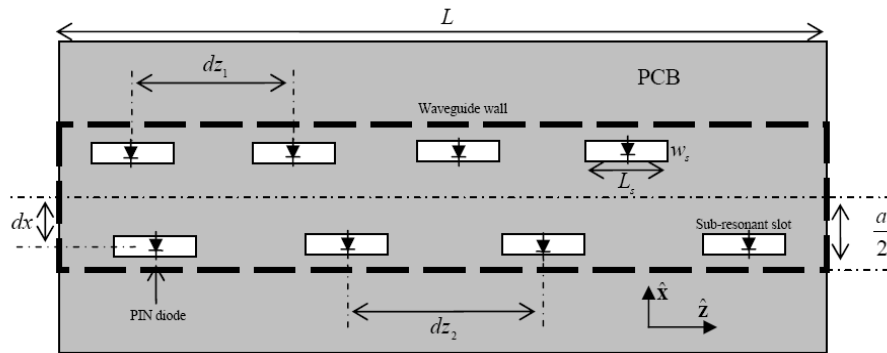
Figure 6.14. Schematic of a waveguide phase shifter design using two rows of longitudinal sub-resonant slots loaded with PIN diodes.

As shown in Figure 6.14, the slot rows are offset from the waveguide center such that each slot interacts sufficiently with the current flowing on the waveguide wall. The center-to-center slots separation is not necessarily the same for both slot

rows. Making slot inter-separation different for different rows can help in reducing the in-band resonances.

For this phase shifter design, it is conceived that the slots can be placed along the center of the waveguide wall while rotated 90 degrees (become transversal) or even be placed on the narrow waveguide wall. Numerical simulation results in the Ka-band showed that this phase sifter can provide 2-3 degrees of relative phase shift by turning ON one PIN diode at a time. Simulations also showed that the phase shift is accumulative in many cases when multiple PIN diodes are turned ON at the same time.

Table 6.3. Description of the Ka-band phase shifter parameters.

Parameter	Description
a	Waveguide broad-side
L	Waveguide length
L_s	Slot length
w_s	Slot width
d_{z1}	Interspacing between 1st row slots along z
d_{z2}	Interspacing between 2nd row slots along z
d_x	Slot center-to-waveguide-center offset along x
$s = a/2 - w_s/2 - d_x$	Slot edge-to-waveguide-wall offset

A waveguide Ka-band phase shifter design based on the above concept was realized to be used with the proposed VNA at 35.5 GHz. Table 6.4 lists the dimensions of the designed phase shifter and Figure 6.15 shows pictures of its various components. The phase shifter was fabricated using a two-layer 0.508 mm thick (1 oz copper) PCB with Rogers-4350 substrate material ($\varepsilon_r = 3.48$ and loss-tangent of 0.004). The phase shifter PCB was mounted on Ka-band aluminum waveguide base and the structure was covered by an aluminum cap. The waveguide phase shifter structure is shown in Figure 6.16 (all dimensions are in mils, 40 mils $\approx$ 1 mm).

Note that diodes 2, 3, 5, 6 and 8 (D2, D3, D5, D6 and D8) load the slots in the first row while diodes 1, 4, 7 and 9 (D1, D4, D7 and D9) load the slots of the second row as shown in Figure 6.15. In general, the relative phase shift at the high

Table 6.4. The designed Ka-band phase shifter dimensions.

Parameter	Dimension (mm), [mils]
a	7.11, [280]
L	44.7, [1700]
L_s	4.0, [157]
w_s	1.0, [40]
d_{z1}	6.25, [246]
d_{z2}	12.5, [492]
d_x	2.0, [80]
$s = a/2 - w_s/2 - d_x$	1.0, [40]
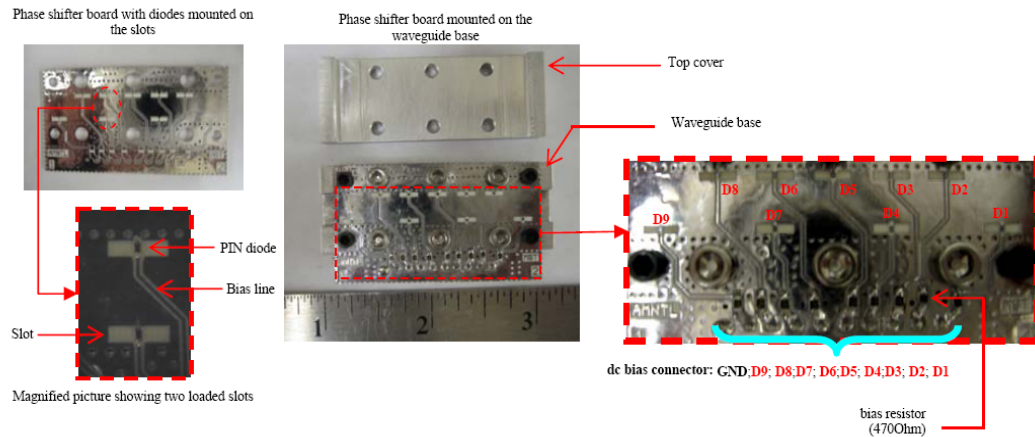
Figure 6.15. Ka-band phase shifter picture showing various it design components.

frequencies in band, i.e., around 35 GHz, is more affected by activating the diodes in the first row (closely-spaced slots).

The designed phase shifter can be controlled digitally by activating 10 states. The first state (state 0) corresponds to all PIN diodes being turned OFF. The second state (state 1) is activated by switching the first and second diodes (D1&D2) ON while keeping the rest OFF, and so on (state 9, all PIN diodes are turned ON). The S-parameters of the designed Ka-band phase shifter were measured at all of its 10 states using Agilent 8364B performance network analyzer (PNA).
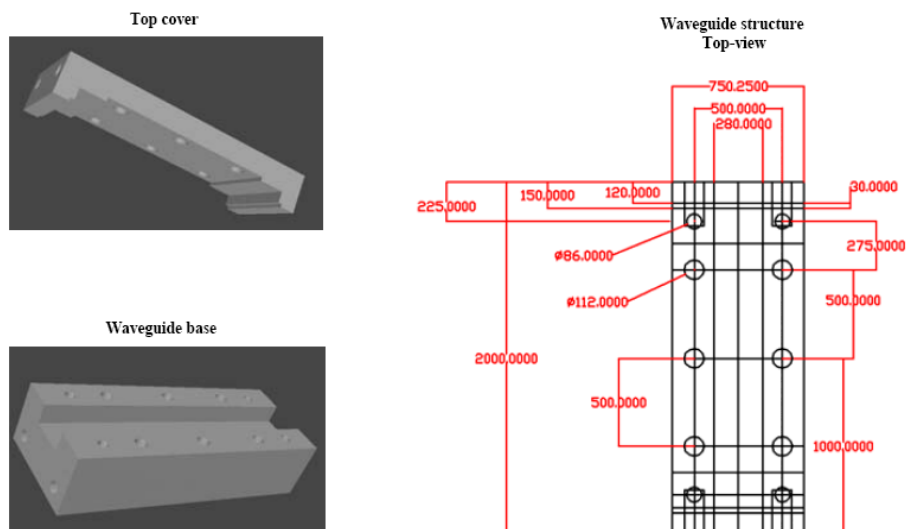
Figure 6.16. Ka-band phase shifter waveguide dimensions (in mils) and 3D pictures.

Figure 6.17 shows a summary of the phase shifter S-parameter measurement results. Figure 6.17(a) shows the minimum (over all states) input and output ports return loss (RL) as well as the maximum insertion loss (IL) measured for the designed phase shifter over the Ka-band. The measured maximum relative phase is shown Figure 6.17(b) as a function of frequency. The min and max curves shown in Figure 6.17(a) give the worse case scenarios for both RL and IL, respectively (high RL and low IL are desired). As shown in Figure 6.17(a), around the frequency of interest, 35.5 GHz, the minimum input and output ports return loss (RL) as well as the maximum insertion loss (IL) are around 14 dB, 16 dB and 4 dB. Around this frequency, a phase shift of about 19 degrees is obtained as shown in Figure 6.17(b). Measurements showed that, linear relative phase shift is obtained by activating diodes 2, 3, 5, 6 and 8 (D2, D3, D5, D6 and D8) only (while keeping the rest ON or OFF).

The Ka-band handheld VNA is intended to be used with a Gunn Oscillator operating at around 35.525 GHz. Figure 6.18 shows the phase shifter insertion loss and relative phase shift as function of the activated phase shifter state measured at 35.525 GHz. The insertion loss at this frequency ranges from 2-4 dB as a function of the phase shifter states (see Figure 6.18(a)). The maximum phase shift is around
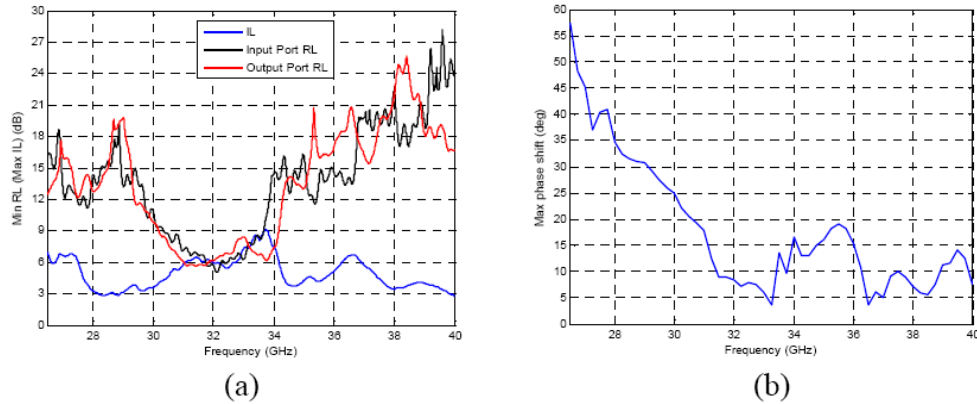
Figure 6.17. Ka-band phase shifter measured (a) minimum input/output ports return loss and maximum insertion loss, (b) maximum relative phase shift.

19 degrees at this frequency (see Figure 6.18(b)). Such phase shift is believed to be sufficient to produce accurate results (as observed from simulations earlier, $\delta\phi = 10^o$ with three phase shifts is adequate for the proposed VNA design.)

Most of the insertion loss associated with the designed phase shifter is attributed to the imperfect contact between the waveguide base and the PCB (which forms the top waveguide wall). The PCB in the current phase shifter design is fixed on top of the waveguide base using screws (see Figure 6.15). Such imperfect fixture results in additional signal losses (there is a longitudinal "gap" between the top and side walls of the waveguide). Future phase shifter designs should consider using conductive adhesive in lieu of the screws to provide better contact between the waveguide base and the PCB. It is believed that once such improved fixture is used, the phase shifter insertion loss can be reduced by 1-2 dBs.

6.5.2. Reflection Measurements. To demonstrate the accuracy of the developed Ka-band VNA, the phase shifter described above was used in a VNA system similar to the one shown in Figure 6.10. The standing-wave device consisted of Ka-band waveguide section and high-frequency diode detector ($L = 31.3$ mm). For this system, there was no need to use an instrumentation amplifier since the designed phase shifter insertion loss was not as high as it was with the X-band phase shifter.
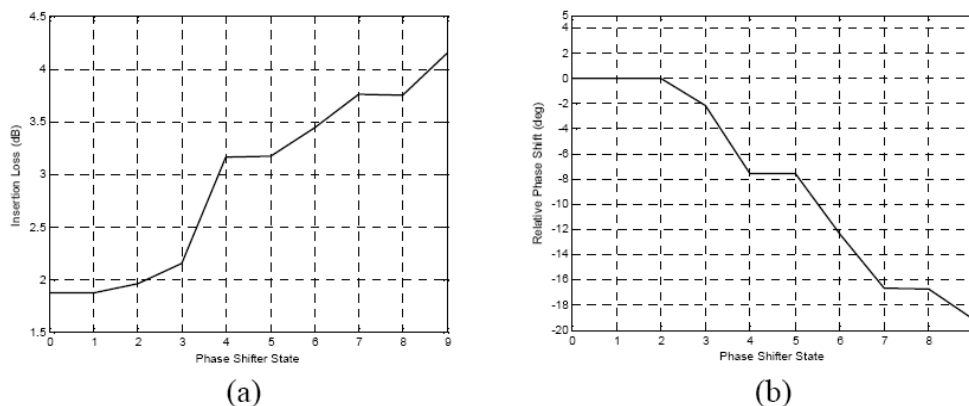
Figure 6.18. Ka-band phase shifter measured (a) insertion loss, and (b) relative phase shift for 10 states at 35.525 GHz.

Frequency doubler was used to generate a 35.525 GHz signal from an HP8350B sweep oscillator signal at 17.763 GHz.

Figure 6.19 shows the measured power-voltage characteristics of the utilized diode detector measured at 35 GHz. The square law-region is indicated in Figure 6.19. Accordingly, the Ka-band VNA system was adjusted such that the diode is always biased in the square-law region.

In this implementation, all 9 phase shifter states were used to solve for the reflection coefficient from the standing-wave voltage measurements. Reflection coefficient measurements of various Ka-band devices were performed using the developed VNA and the measurements were compared to Agilent 8364B PNA. Table 6.5 compares the reflection measurements obtained for a short and 3 mm offset short using both VNA systems at 35.525 GHz. As shown in Table 6.5, the development VNA measurements were very close to those of the 8364B PNA.

To further highlight the efficacy of the developed Ka-band VNA, reflection measurements of variable loads were also performed. To this end, two variable loads consisting of a variable offset-short (Load 1, see Figure 6.20(a)), and a 3 dB-attenuator cascaded with the variable offset-short (Load 2, see Figure 6.20(b)) were considered for measurement using the proposed VNA and Agilent 8364B PNA at 35.525 GHz.
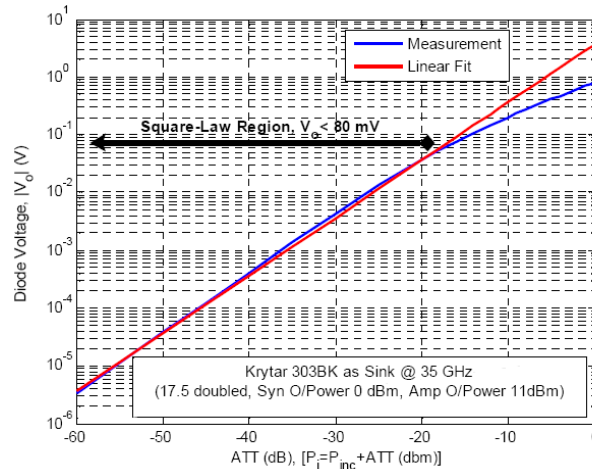
Figure 6.19. Diode detector measured characteristic curve (input power vs. output).

Table 6.5. Reflection coefficient measurements obtained using Agilent 8364B PNA and the proposed VNA for short and offset short loads at 35.525 GHz.

Load	$|\Gamma|$ (dB)		**Phase of** Γ (deg.)	
	8364B PNA	Proposed VNA	8364B PNA	Proposed VNA
Short	-0.010	-0.008	-179.97	-179.92
3mm Offset Short	-0.014	0.066	-25.83	-25.57

The complex reflection coefficients of Load 1 and 2 shown in Figure 6.20 were measured for short offsets ranging from 0 to 6 mm in steps of 0.5 mm (which gives more than one phase cycle at 35.525 GHz). Figures 6.21(a)-(b) show the measured magnitude and phase of the reflection coefficient using the developed VNA and the 8364B PNA for both loads.

It is evident from the measurements results presented in Figure 6.21 that the proposed VNA measurements closely match Agilent 8364B PNA results for both loads and for most of the considered short offsets. Assuming the PNA measurements are closer to the nominal reflection values, the average absolute phase error in the obtained measurements using the proposed VNA with respect to the PNA measurements for the first and second loads were around 4.32^o and 3.72^o, respectively. Average absolute
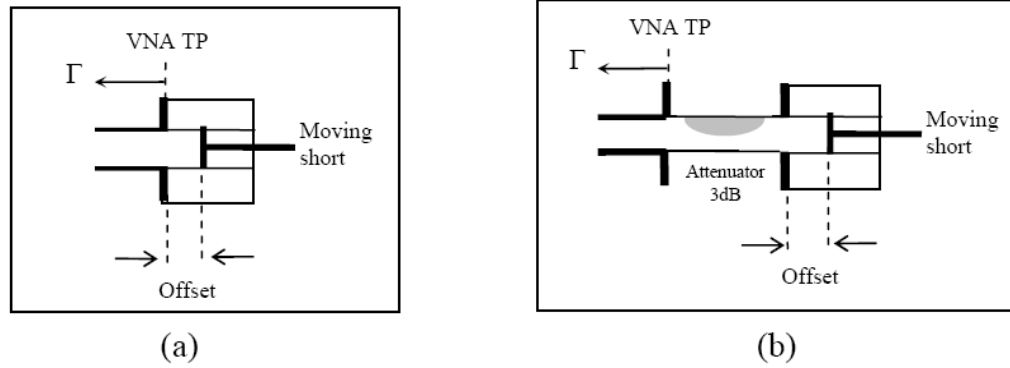
Figure 6.20. Schematics of the variable Ka-band loads used in testing, (a) Load 1, and (b) Load 2.
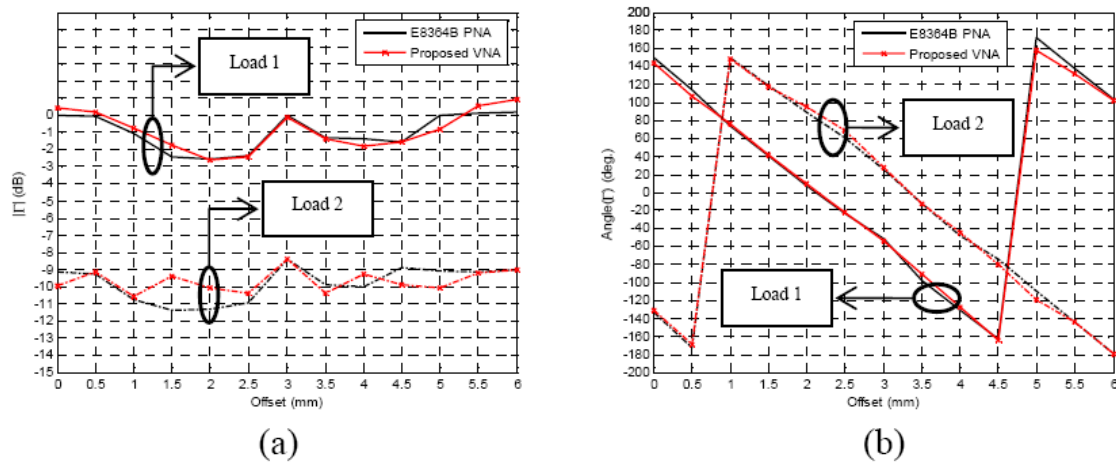
Figure 6.21. Measured (a) magnitude and (b) phase of the reflection coefficients for two variable loads as obtained using the proposed VNA and Agilent 8364B PNA at 35.525 GHz.

magnitude errors of around 0.037 and 0.023 were observed for the first and second loads, respectively.

It is believed that this is the first time when a VNA based on simple power-detection scheme, such as the developed VNA, provides Ka-band measurement (around

35 GHz) results comparable to a high-performance tuned-receiver VNA such as Agilent 8364B PNA.

6.5.3. Imaging Results. Radomes are typically designed to protect radar or communication systems from undesired environmental effects while minimally influencing the system performance. Radomes are typically made of Honeycomb composite cores and fiber-glass skins. Any subsurface flaws in a honeycomb composite radome can significantly degrade the performance of the system the radome was intended to protect. Hence, there is a great need to inspect the honeycomb radomes routinely and assess the integrity of their electrical and structural properties. Millimeter waves imaging and inspection techniques have shown great potential for such application [22], [23]. The standing-wave based Ka-band VNA was specifically developed to image and quantitatively inspect radome structures.

A handheld Ka-band VNA based on the developed approach was realized using a compact Gunn oscillator and a Ka-band waveguide isolator. Figure 6.22 shows a picture of the handheld Ka-band VNA (various system components are indicated).
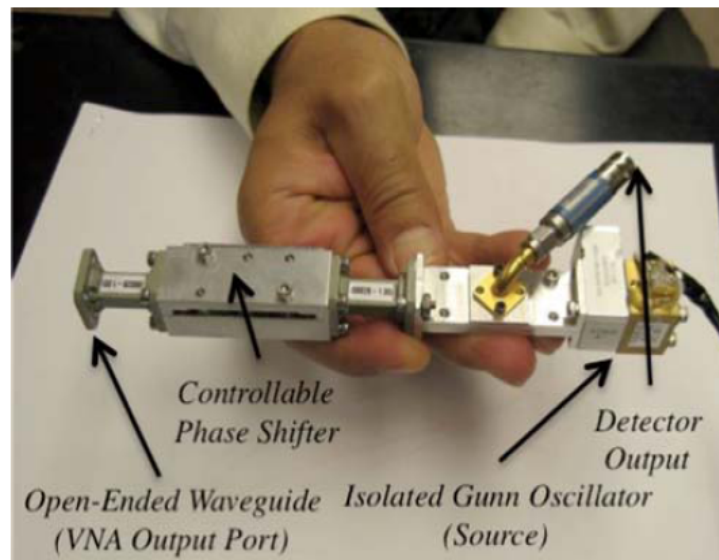
Figure 6.22. Handheld Ka-band VNA system designed based on the proposed approach.

The spectrum of the Gunn oscillator was measured using Agilent E4448A spectrum analyzer. The frequency of the Gunn oscillator was measured to be around 35.535 GHz under normal conditions, and its output power was around 9 dBm as shown in Figure 6.23(a). The magnitude of the measured S-parameters of the utilized Ka-band isolator is shown in Figure 6.23(b) as a function of frequency. At 35.535 GHz, the isolator passes the oscillator signal with minimum attenuation and it provides a high isolation of around 22 dB in the reverse direction as desired.
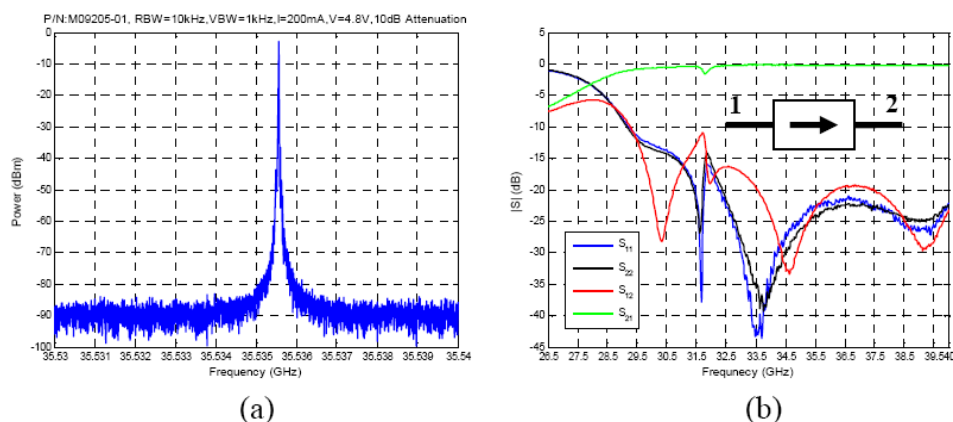
Figure 6.23. (a) Measured spectrum of the Gunn oscillator, and (b) magnitude of the measured S-parameters of the Ka-band isolator.

The VNA was used to produce raster scan images of a 3/4"-thick radome test panel constructed with several subsurface inserts (square and circular in shape). The subsurface inserts are of different sizes and embedded at different depths within the panel. Figure 6.24(a) shows a picture the radome panel considered here. Detailed schematic of the panel (its insert map) is shown in Figure 6.24(b).

Figures 6.25(a)-(b) show the magnitude and phase raster images, respectively, obtained using the developed Ka-band VNA at 35.535 GHz with a relatively short Ka-band horn antenna at standoff of 2 mm. The images in these figures correspond to the scanned area indicated in Figure 6.24(b) (note that the produced images are transposed with respect to the actual schematic of the panel). As shown in the

Honeycomb Radome Panel

Top 2 Rows All 0.012" thick
1ˢᵗ Row – 0.5" dia inserts – mid of top skin – top core – bottom core – mid of bottom skin – then repeated as 0.25" dia
2ⁿᵈ Row – Repeat of circles in top row, but 1" dia
3ʳᵈ row 8, 12, 16, 20 mils thick & All at top skin to core interface
Fourth row 8, 12, 16, 20 mils thick & All at bottom skin to core interface
5ᵗʰ row Top of core milled down 8, 12, 16, 20 mils
6ᵗʰ Row Bottom of core milled down 8, 12, 16, 20 mils
7ᵗʰ Row – Water Intrusion Flaws – 0.25", 0.5" 1" dia

(a)   (b)

Figure 6.24. (a) A picture showing the imaged radome panel, and (b) detailed schematic of the panel showing the subsurface insert map.

obtained images, most of the subsurface inserts are detected with high resolution, i.e., their actual shapes are apparent in the obtained images.

Since the phase and magnitude measurements at each scan point are now available, the measurements can be processed using synthetic aperture focusing techniques (SAFT) [25]. Figure 6.25(c) shows the focused image after applying SAFT (focused at the surface of the panel). Because the standoff distance is small and the used horn has small aperture, the improvement in the SAFT image over the raw near-field images is marginal in this case.

A longer Ka-band horn placed at standoff distance of 10 mm was also used with the developed Ka-band VNA to produce raster magnitude and phase images of the test radome panel. Figures 6.26(a)-(b) show the obtained magnitude and phase images with the long horn.

Although the indications/signatures of the inserts are clearly observed in the obtained raw phase and magnitude images shown in Figures 6.26(a)-(b), respectively,
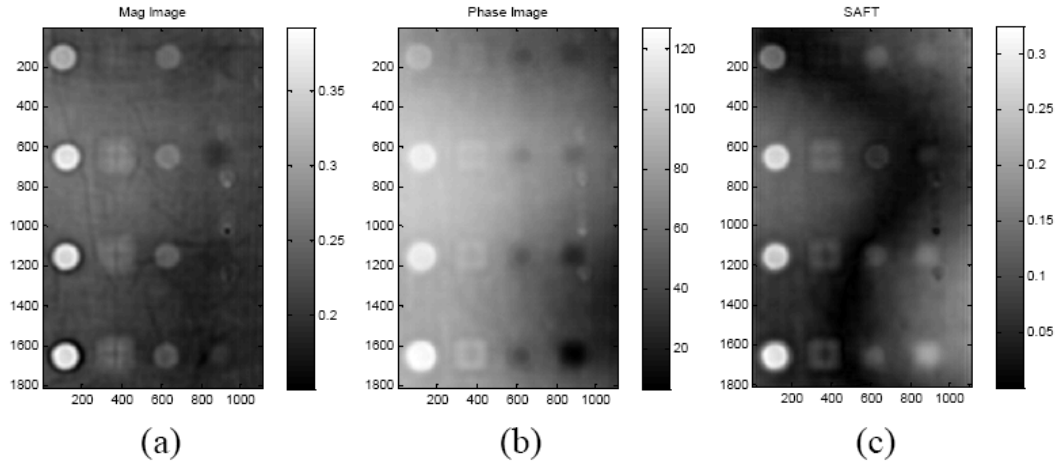
Figure 6.25. (a) Magnitude, (b) phase, and (c) SAFT images of the radome panel
obtained at 35.535 GHz using the developed handheld Ka-band VNA
with a short-horn antenna at standoff distance of 2 mm.

these indications are faint in most cases. Processing the phase and magnitude measurements using SAFT produced a high resolution image as shown in Figure 6.26(c).

6.6. SUMMARY

Simple, handheld, relatively inexpensive, and automated vector network analyzers (VNAs) are in demand for wide range of applications requiring *in-situ* vector measurements such as microwave and millimeter wave circuit characterization, imaging, material characterization, and nondestructive testing. For these and similar emerging applications, a novel vector network analyzer (VNA) design was introduced in this section. The simplicity of the proposed VNA design stems from the fact that it is based on standing-wave measurements performed using single power detector. Additionally, the proposed VNA can be calibrated following simple procedure using three calibration standards only. The complex reflection coefficient of the device-under-test (DUT) is inferred from three phase-shifted standing-wave measurements. An electronic phase shifter inserted between the DUT and the standing-wave probing device is controlled to yield the required phase shifts. Various attributes of the
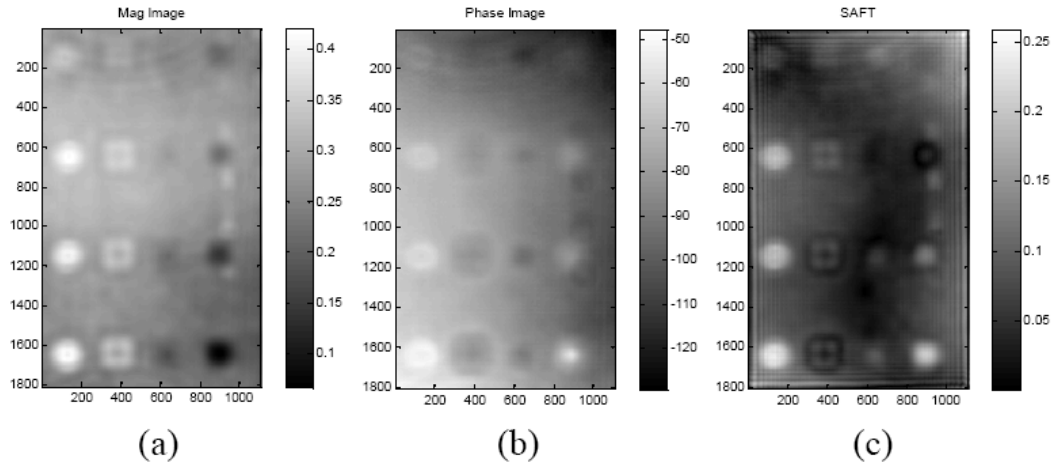
Figure 6.26. (a) Magnitude, (b) phase, and (c) SAFT images of the radome panel obtained at 35.535 GHz using the developed handheld Ka-band VNA with a long-horn antenna at standoff distance of 10 mm.

proposed design were investigated in simulation considering the phase shifter characteristics and the detector noise. It was shown that the uncertainties in phase and magnitude measurements increase linearly with the detector noise RMS value.

To demonstrate the feasibility and accuracy of the proposed VNA, off-the-shelf electronic phase shifter was used in constructing a prototype automated X-band VNA. The prototype was used to perform swept and single frequency measurements of various DUTs. Excellent agreement between the measurements obtained using the proposed VNA prototype and the HP8510C VNA was observed. The results showed that the proposed VNA provides highly accurate vector measurements with typical errors in the order of 0.01 and 1°, for magnitude and phase respectively. The measurement accuracy of the proposed VNA can be improved further by utilizing a higher quality phase shifter.

This section also presented a Ka-band handheld prototype VNA using a phase shifter designed specifically to be used with the VNA. The measurement accuracy of the Ka-band VNA was illustrated via various comparisons with an Agilent E8364B performance network analyzer (PNA). Furthermore, the capabilities of the developed VNA in practical millimeter wave imaging scenarios were demonstrated.

Future investigations should consider performing comprehensive measurement uncertainty analysis. Extending the scope of application of the proposed VNA to perform transmission as well as reflection measurements poses no problem of fundamental nature and it follows the same concepts adopted for the well-established six-port reflectometer. Finally, constructing VNAs using planner circuit technology with discrete components or monolithic microwave integrated (MMIC) circuit technology is very feasible. Such VNAs with reduced form-factor are by far more convenient for *in-situ* measurements.

7. CONCLUDING REMARKS

The ability of microwaves and millimeter waves (300 MHz – 300 GHz) to penetrate into dielectric structures makes them particularly appealing for subsurface sensing purposes. Consequently, microwave and millimeter wave imaging techniques have shown great potential in a wide range of industrial and medical applications. These techniques are fundamentally based on measuring relative and coherent electromagnetic field distributions, e.g., electric field, scattered due to an irradiated object. Various systems can be devised for measuring the relative field distributions; each with it own advantages and limitations. This dissertation was focused on addressing critical challenges related to the practical implementation of various microwave and millimeter wave imaging systems. Specifically, this research was meant to achieve three main objectives related to designing efficient modulated imaging array elements/methods, reducing the sensitivity to standoff distance variations in near-field imaging, and designing a simple vector measuring device for *in-situ* imaging applications. The idea of direct antenna and scatterer modulation via controlled loading was central for achieving these three objectives.

The simplest microwave and millimeter wave imaging system uses a single mechanically scanned antenna to measure the coherent field distribution in the spatial domain of interest. Due to their simplicity, imaging systems with scanned antennas have been used successfully in many applications. This is particularly true for near-field imaging systems using scanned open-ended waveguides. Obviously, such systems cannot be used for real-time imaging required in some critical applications. However, scanning-based microwave and millimeter wave imaging systems will continue to have a major role in applications where real-time imaging is not required, mainly since they are relatively inexpensive.

To facilitate real-time imaging, array of antennas can be utilized where each antenna (element) in the array provides a measure of the electric field at its location in the array. Using arrays provides the required spatial field sampling while eliminating the need for time-consuming mechanical scanning. Proper design of the antenna array, array elements, and the receiving scheme are critical to realize relatively inexpensive, high-resolution, and sensitive imaging systems.

For high-resolution real-time imaging systems, spatially large and compact antenna arrays are typically required. For microwave and millimeter wave imaging, this requires implementing arrays with number of elements ranging from few hundreds to few thousands. Designing receiving schemes for such large arrays is the main challenge in building microwave and millimeter wave imaging systems. Due to the required large number of array elements, using a dedicated receiver to measure the signal picked up by each element is prohibitively expensive and complex to implement in practice especially in the millimeter wave frequency range. Hence, cost-effective receiving schemes must utilize spatial-signal multiplexing to reduce of number of receivers and the complexity of the high-frequency circuitry, i.e., switches, while providing high measurement sensitivity. The modulated scatterer technique (MST)-based imaging systems uses such spatial multiplexing.

In MST-based imaging systems, array of auxiliary scatterers such as small dipoles is placed in the electric field of interest. By controlled electrical loading, the scattering cross-section of these dipoles are modulated over time, and this in turn, modulates the scattered electric field. The modulated electric field is then detected at a remote location away from the object being imaged. Essentially, the phase and magnitude of field of interest at the location of a certain scatterer, is carried by the modulated signal received form that scatterer. Basically, modulating the dipole scatterers allows for spatial electric field measurement multiplexing, and thus, the MST-based imaging system can potentially be built with single receiver only. The conventional MST-based systems, as known today, suffer from major limitations which render their implementation in or near the millimeter wave frequency range very challenging. The inefficiency of the small dipoles typically used with these systems limits the modulation depth and the signal-to-noise ratio, and hence, the obtained measurement sensitivity. Since the modulated scattered signal level from the array dipole is very small, the robustness of the conventional MST system is undermined by a residual carrier problem which complicates detecting the signal of interest. Furthermore, the mutual coupling among the array dipoles can significantly limit the system dynamic range.

In this dissertation, the sensitivity of the conventional MST based on modulated dipoles was studied theoretically and experimentally. It was found that the

major problem with the conventional MST is the very low modulation depth obtained with dipoles (less than 2% modulation depth was observed with such elements at 24 GHz). To realize high sensitivity MST-based imaging systems, more efficient modulated scatterers and array elements should be utilized. Designing modulated scatterers and antennas which can provide modulation depths much higher than the dipoles typically used with MST was the first objective of this research. To achieve that; the multiple loaded scatterer (MLS) method and the loaded elliptical slot were introduced.

The proposed MLS method is based on modulating a single strong scatterer as opposed to the small loaded dipoles used in the conventional MST arrays. The MLS method allows for accurate recovery of the electric field distributions of interest based on measurements performed using a single receiver. For this purpose, the MLS method utilizes a linear scatterer loaded with PIN diodes, at multiple discrete locations over its length, while placed in the field of interest. Using multiple loads allows for loading the scatterer structure with distinct modulation states, or loading conditions. As an intermediate step towards recovering the field of interest, the MLS method reconstructs the current distribution induced on the scatterer when all of its loads are short-circuited. Since the MLS method is not based on discrete elements, the limiting factors of the conventional MST which are related to array element dispersion and mutual coupling do not limit its performance. Furthermore, the modulated scattered signal level in the MLS implementation is much higher than that in the conventional MST case (measurement results showed that the MLS can provide a modulation depth of around 14%). In practice, this fact translates to higher measurement sensitivity.

A new modulated elliptical slot was introduced as an alternative to the inefficient loaded dipoles conventionally used with the imaging arrays. The proposed slot is a compact resonant slot loaded with a PIN diode. Although, the longest dimension of the slot is only around one third of the operating wavelength, it is resonated to work at the frequency of interest by special loading. It was shown that the designed slot provides modulation depth of around 96.5% which is significantly higher than the modulation depth obtained using a dipole scatterer. The designed slot is efficient and exhibits very small mutual coupling once used in an array. Consequently, when array

of these slots are used in MST-based imaging system, they result in higher sensitivity compared to arrays of loaded dipoles. Besides improving the system sensitivity by the virtue of increasing the modulation depth, the residual carrier suppressing procedures routinely used with the conventional MST imaging arrays are not needed when the designed slot is utilized since the modulated signal is only 6 dB below the carrier. Due to its efficiency, the developed slot was successfully used to implement the first prototype of a microwave camera operating at 24 GHz. It is also being currently used in the design of the second generation of the camera.

The second objective of this research was to design a near-field imaging probe that is relatively insensitive to variations in standoff distance. A unique near-field microwave and millimeter wave differential probe based on dual-loaded modulated single waveguide aperture is developed. In this design, two PIN-diode loaded dipoles were used to modulate the aperture of the waveguide. Using this novel design the undesired influence of standoff distance variation in near-field imaging can be eliminated, or otherwise significantly reduced by non-coherently detecting and subtracting the signals measured at two different aperture modulation states. In addition, this differential probe efficiently overcomes the limitations of the previously developed standoff distance variation compensation methods. The proposed dual-loaded modulated aperture probe was shown to combine the attractive features of the previous coherent and non-coherent probes; versatility and simplicity, in a compact design. The idea behind the proposed probe; synthesizing two mirror electric field distributions through dual aperture loading, was verified via simulations and experiments. Extensive numerical simulations were performed to study the design parameters which impact the probe sensitivity and resolution. A Ka-band prototype probe was designed and tested experimentally. It was shown that the proposed probe efficiently reduces the standoff distance variations based simple non-coherent detection.

Finally, the third objective was to design vector network analyzer (VNA) aimed to meet the rising needs for wideband, simple, handheld, relatively inexpensive, and *in-situ* vector measuring devices. Such device can be used effectively for quantitative microwave and millimeter wave inspection and imaging as well as many other critical applications such as circuit characterization, reflectometry, and material characterization. To this end, a novel VNA system based on simple standing-wave measurements

was designed, implemented, and tested. The proposed design circumvents the expensive heterodyne detection scheme required to implement tuned-receiver based VNAs. It also is unique compared to the previously developed power measurement based VNA systems in that it utilizes single power detector, and it does not require multi-port coupling devices. Furthermore, the proposed VNA can be calibrated with three known standards only to yield accurate vector measurements. To realize handheld millimeter wave VNA based on the proposed approach, a custom-designed waveguide phase shifter was introduced. The developed phase shifter is based on loaded sub-resonant slots cut into the wall of a waveguide. Loading the slots with PIN diodes and thereafter controlling the diodes electronically can provide highly stable and distinctive phase shifts. The only requirement on the slots is to be sub-resonant so that they do not radiate efficiently or cause high reflections.

To demonstrate the feasibility and accuracy of the proposed VNA, automated X- and Ka-band VNAs were developed and their measurements were compared to tuned-receiver commercial VNAs. These prototypes were used to perform swept and single frequency measurements of various devices in the X- and Ka-bands. Excellent agreement between the measurements obtained using the proposed VNA prototypes and the tuned-receiver commercial VNAs was observed.

BIBLIOGRAPHY

[1] R. Zoughi, *Microwave Non-Destructive Testing and Evaluation*, Kluwer Academic Publishers, the Netherlands, 2000.

[2] R. Zoughi, "Microwave and millimeter wave nondestructive testing: a succinct introduction," *Materials Evaluation*, vol. 53, no. 4, pp. 461-462, April, 1995. Reprinted in the *Research in Nondestructive Evaluation*, vol. 7, no. 2/3, pp. 71-74, 1995.

[3] R. Zoughi and S. Bakhtiari, "Microwave nondestructive detection and evaluation of disbonding and delamination in layered-dielectric slabs," *IEEE Trans. on Instrum. and Measure.*, 39(6), pp. 1059-1063, Dec. 1990.

[4] N. Qaddoumi, S. I. Ganchev, G. Carriveau and R. Zoughi, "Microwave imaging of thick composites with defects," *Materials Evaluation*, vol. 53, no. 8, pp. 926-929, August, 1995.

[5] N. Qaddoumi, R. Zoughi, and G.W. Carriveau, "Microwave detection and depth determination of disbonds in low-permittivity and low-loss thick sandwich composites," *Research in Nondestructive Evaluation*, vol. 8, no. 1, pp. 51-63, 1996.

[6] N. Qaddoumi, W. Saleh, and M. Abou-Khousa, "Innovative near-field nondestructive testing of corroded metallic structures utilizing open ended rectangular waveguide probes," *IEEE Trans. on Instrum. and Measure.*, vol. 56, no. 5, pp. 1961-1966, Oct. 2007.

[7] E. Nanni, M. Abou-Khousa, S. Kharkovsky, R. Zoughi and R. Austin, "Near-field microwave in-process thickness monitoring of coatings undergoing curing," *Materials Evaluation*, vol. 66, no. 8, pp. 865-870, Aug. 2008.

[8] L. Handjojo, K. J. Bois, J. Bauer, R. Hamilton and R. Zoughi, "Broad-band microwave dielectric property characterization of various glass specimens," *Nondestructive Testing & Evaluation*, 2000.

[9] K. Bois, A. Benally and R. Zoughi, "Microwave near-field reflection property analysis of concrete for material content determination," *IEEE Trans. on Instrum. and Measure.*, vol. 49, no. 1, pp. 49-55, February 2000.

[10] K. Bois, L. Handjojo, A. Benally, K. Mubarak and R. Zoughi, "Dielectric plug-loaded two-port transmission line measurement technique for dielectric property characterization of granular and liquid materials," *IEEE Trans. on Instrum. and Measure.*, vol. 48, no. 6, pp. 1141-1148, December 1999.

[11] C. Yeh and R. Zoughi, "A Novel microwave method for detection of long surface cracks in metals," *IEEE Trans. on Instrum. and Measure.*, vol. 43, no. 5, pp. 719-725, October, 1994.

[12] E. J. Bond, X. Li, S. C. Hagness, B. D. V. Veen, "Microwave imaging via space-time beamforming for early detection of breast cancer," *IEEE Trans. Antennas Propag.*, vol 51, no. 8, pp. 1690 – 1705, Aug. 2003.

[13] E. C. Fear and M. A. Stuchly, "Microwave detection of breast cancer," *IEEE Trans. on Microwave Theory and Tech.*, vol. 48, no. 11, pp. 1854 – 1863, Nov. 2000.

[14] J.-C. Bolomey, G. E. Gardiol, *Engineering applications of the modulated scatterer technique*, Norwood, MA: Artech house Inc. 2001.

[15] S. Kharkovsky, J. T. Case, M. A. Abou-Khousa, R. Zoughi, and F. Hepburn, "Millimeter wave detection of localized anomalies in the space shuttle external fuel tank insulating foam," *IEEE Trans. on Instrum. and Measure.*, vol. 55, no. 4, pp. 1250-1257, Aug. 2006.

[16] S. Kharkovsky, F. Hepburn, J. Walker, R. Zoughi., "Nondestructive testing of the space shuttle external tank foam insulation using near field and focused millimeter wave techniques," *Materials Evaluation*, vol. 63, N5, pp. 516-522, 2005.

[17] N. Qaddoumi, M. Abou-Khousa, and W. Saleh, "Near-field microwave imaging utilizing tapered rectangular waveguides," *IEEE Trans. on Instrum. and Measure.*, vol. 55, no. 5, pp. 1752-1756, Oct. 2006.

[18] M. Ghasr, M. Abou-Khousa, S. Kharkovsky, R. Zoughi and D. Pommerenke, "A Novel 24-GHz, one-shot, rapid, and portable microwave imaging system," *Proc. IEEE Intern. Instrum. and Measure. Tech. Conf.*, I2MTC 2008, pp. 1798-1802, May 2008.

[19] C. Yu, and *et al*, "Active microwave imaging II: 3-D system prototype and image reconstruction from experimental data," *IEEE Trans. Microw. Theory Tech.*, Vol. 56, no 4, pp. 991 – 1000, April 2008.

[20] M. Pastorino, "Modern microwave: inverse-scattering techniques for image reconstruction," *IEEE Instrum. & Measur. Mag.*, vol. 1, no. 4, pp. 20 – 25, Dec. 1998.

[21] M. Pastorino, "Stochastic optimization methods applied to microwave imaging: a review," *IEEE Trans. Antennas Propag.*, vol. 55, no. 3, pp. 538 – 548, March 2007.

[22] M. A. Abou-Khousa, A. Ryley, S. Kharkovsky, R. Zoughi, D. Daniels, N. Kreitinger and G. Steffes, "Comparison of x-ray, millimeter wave, shearography and through-transmission ultrasound methods for inspection of honeycomb composites," *Proc. of the 33rd Annual Review of Progress in Quantitative Nondestructive Evaluation*, QNDE 2006, vol. 26A, pp. 999-1006, Portland, Oregon, July 30-August 4, 2006.

[23] M. Ravuri, M. Abou-Khousa, S. Kharkovsky, R. Zoughi, and R. Austin, "Microwave and millimeter wave near-field methods for evaluation of radome composites," *Proc. of the 34th Annual Review of Progress in Quantitative Nondestructive Evaluation*, QNDE 2007, vol. 27B, pp. 976-981, Golden, CO, July 22-July 27, 2007.

[24] N. Qaddoumi, T. Bigelow, R. Zoughi, L. Brown and M. Novack, "Reduction of sensitivity to surface roughness and slight standoff distance variations in microwave inspection of thick composite structures," *Materials Evaluation*, vol. 60, no. 2, pp. 165-170, February 2002.

[25] J. T. Case, J. Robbins, S. Kharkovsky, F. Hepburn, R. Zoughi, "Microwave and millimeter wave imaging of the space shuttle external fuel tank spray on foam insulation (SOFI) using synthetic aperture focusing techniques (SAFT)," *Proc. of the 33th Annual Review of Progress in Quantitative Nondestructive Evaluation*, QNDE 2006, vol. 820, pp. 1546-1553, July 2006.

[26] M. Abou-Khousa, and R. Zoughi, "Disbond thickness evaluation employing multiple-frequency near-field microwave measurements," *IEEE Trans. on Instrum. and Measure.*, vol. 56, no. 4, pp. 1107-1113, Aug, 2007.

[27] M. Abou-Khousa and R. Zoughi, "Microwave quantitative NDE technique for dielectric slab thickness estimation using the MUSIC algorithm," *Proc. of the 33rd Annual Review of Progress in Quantitative Nondestructive Evaluation,* QNDE 2006, vol. 26A, pp. 440-447, Portland, Oregon, July 30- August 4, 2006.

[28] J. H. Richmond, "A modulated scattering technique for measurement of field distributions," *IEEE Trans. Microw. Theory Tech.*, vol. 3, no. 4, pp. 13-15, Jul 1955.

[29] M-K Hu, "On measurements of microwave E and H field distributions by using modulated scattering methods," *IRE Trans. Microw. Theory Tech.*, vol. 8, no. 3, pp. 295-300, May 1960.

[30] K. Iigusa, and *et al*, "Experimental proof of electrically invisible state of inductively loaded dipole and proposal of electrically invisible meander-lines," *IEEE Trans. Antennas Propag.*, vol. 54, no. 11, pp. 3374-3382, Nov. 2006.

[31] C. A. Balanis, *Advanced Engineering Electromagnetics*, New York: Wiley,1989.

[32] D. H. Werner, P. L. Werner, and J. K. Breakall, "Some computational aspects of Pocklington's electric field integral equation for thin wires," *IEEE Trans. Antennas Propag.*, vol. 42, no. 4, pp. 561-563, April 1994.T.

[33] R. Harrington, "Matrix methods for field problems," *Proceedings of the IEEE*, vol. 55, no. 2, pp. 136-149, Jan. 1967.

[34] T. K. Sarkar, A. R. Djordjevic, and E. Arvas, "On the choice of expansion and weighting functions in the numerical solution of operator equations," *IEEE Trans. Antennas Propag.*, vol. AP-33 , no. 9, pp. 988-996, Sept. 1985.

[35] R. Harrington and J. Mautz, "Straight wires with arbitrary excitation and loading," *IEEE Trans. on Anten. and Propag.*, vol. 15, no. 4, pp. 502-515, July 1967.

[36] C. A. Balanis, *Antenna Theory, Analysis and Design*, 2nd Ed., Wiley, NY,1982.

[37] K. K. Mei, "Theory of maxwellian circuits," *Radio Sci. Bull*, vol. 305, pp. 6-13, Sept. 2003.

[38] L. Li., and *et al*, "Applications of the maxwellian circuits to linear wire antennas and scatterers," *IEEE Trans. Antennas. Propag.*, vol. 54, no. 10, pp. 2725-2730, Oct. 2006.

[39] Y. Liu; M. He, and K. K Mei, "Implement the theory of Maxwellian circuits to spiral antennas," *IEEE Trans. on Electromag. Compat.*, vol 47, no. 4, pp. 998-1003, Nov. 2005.

[40] M. Abou-Khousa, and R. Zoughi, "Maxwellian circuits-based analysis of loaded wire antennas and scatterers," *IEEE Antennas and Wireless Propag. Letters*, vol. 7, pp. 318-320, Oct. 2008.

[41] J. Jin, *The Finite Element Method in Electromagnetics*, 2nd Ed., Wiley, NY, 2002.

[42] T. P. Budka, S. D. Waclawik, and G.M Rebeiz, "A coaxial 0.5-18 GHz near electric field measurement system for planar microwave circuits using integrated probes," *IEEE Trans. Microw. Theory Tech.*, vol 44, no. 12, part 1, pp. 2174-2184, Dec. 1996.

[43] S. Caorsi, M. Donelli, and M. Pastorino, "A passive antenna system for data acquisition in scattering applications," *IEEE Antennas and Wireless Propag. Letters*, vol. 1, no. 1, pp. 203-206, 2002.

[44] M. A. Abou-Khousa and R. Zoughi, "Electric field measurement using multiple loaded linear scatterers," *Proc. Intern. Symp. on Antennas and Propag.*, ISAP'08, Taipei, Taiwan, pp. 565-568, Oct 2008.

[45] M. A. Abou-Khousa and R. Zoughi, "Multiple loaded scatterer method for E-field mapping applications," *IEEE Trans. on Antennas and Propag.*, In review, p. 8, Jan. 2009.

[46] R. Harrington and J. Mautz, "Pattern synthesis for loaded N-port scatterers," *IEEE Trans. on Antennas and Propag.*, vol. 22, no. 2, pp. 184-190, March 1974.

[47] R. Harrington and J. Mautz, "Optimization of Radar cross section of N-port loaded scatterers," *IEEE Trans. Antennas Propag.*, vol. 22, no. 5, pp. 697-701, Sept. 1974.

[48] A. Poggio and P. Mayes, "Bandwidth extension for dipole antennas by conjugate reactance loading," *IEEE Trans. Antennas Propag.*, vol. 19, no. 4, pp. 544-547, July 1971.

[49] Tyco Electronics, M/A-COM Wirless Components; [Online], http://www.macom.com/DataSheets/MA4AGP907_FCP910.pdf.

[50] A. D. Skinner, "Modulation: fundamental techniques for traceability," *IEE Colloquium on Accreditation of RF Measurement*, pp. 6/1 - 6/6, Feb 1993.

[51] J.-C. Bolomey, and *et al*, "Rapid near-field antenna testing via arrays of modulated scattering probes," *IEEE Trans. Antennas Propag.*, vol. 36, no. 6, pp. 804-814 , June 1988.

[52] R. F. Harrington, "Small resonant scatterers and their use for field measurements," *IRE Trans. Microw. Theory Tech.*, vol. MTT-10, pp.165–174, May 1962.

[53] O. Franza, N. Joachimowicz, and J.-C. Bolomey, "SICS: a sensor interaction compensation scheme for microwave imaging," *IEEE Trans. Antennas Propag.*, vol. 50, no. 2, pp. 211-216 , Feb. 2002.

[54] A. V. Oppenheim, R.W. Schafer, and J. R. Buck, *Discrete-Time Signal Processing*, 2nd Ed., Prentice-Hall, NJ, 1999.

[55] J. D. Kraus, *Antennas*, 2nd Ed., McGraw-Hill, NY, 1988.

[56] Y. T. Lo (Ed) and S.W Lee (Ed), *Antenna Handbook: Theory, Applications, and Design*, Van Nostran Reinhold Com. Inc, NY, USA, 1988.

[57] P. Li, J. Liang, and X. Chen, "Study of printed elliptical/circular slot antennas for unltrawideband applications," *IEEE Trans. Antennas Propag.*, vol. 54, no. 6, pp. 1670-1675, June 2006.

[58] C.-Y. Hong, C.-W. Ling, I-Y. Tarn, and S-J. Chung, "Design of a planner ultrawideband antenna with a new band-notch structure," *IEEE Trans. Antennas Propag.*, vol. 55, no. 12, pp. 3391-3397, Dec. 2007.

[59] M. A. Abou-Khousa, S. Kharkovsky, and R. Zoughi, "On the mutual coupling between circular resonant slots," *Proc. 3rd Intern. Conf. on Electromagnetic Near-Field Charact. & Imaging* (ICONIC 2007), pp. 117 – 122, St. Louis, USA, 27 – 29 June 2007.

[60] CST - Computer Simulation Technology, http://www.cst.com.

[61] S. Kharkovsky, A.C. Ryley, V. Stephen and R. Zoughi, "Dual-polarized near-field microwave reflectometer for non-invasive inspection of carbon fiber reinforced polymer (CFRP) strengthened structures," *IEEE Trans. on Instrum. and Measur.*, vol. 57, no. 1, pp. 168-175, Jan. 2008.

[62] M. T. Ghasr, B. Carroll, S. Kharkovsky, R. Austin, and R. Zoughi, "Millimeter-wave differential probe for nondestructive detection of corrosion precursor pitting," *IEEE Trans. on Instrum. and Measur.*, vol. 55, no. 5, pp. 1620-1627, Oct. 2006.

[63] M. A. Abou-Khousa and R. Zoughi, "Novel near-field microwave and millimeter wave differential probe using a dual-modulated single aperture," *Proc. IEEE Intern. Instrum. and Measure. Tech. Conf.*, I2MTC 2008, pp. 442-445, May 2008, Victoria, BC, Canada.

[64] M. A. Abou-Khousa, S. Kharkovsky, and R. Zoughi, "Novel near-field millimeter wave differential probe using loaded modulated aperture," *IEEE Trans. on Instrum. and Measure.*, Accepted, To appear in May 2009.

[65] R. Janaswamy and S-W. Lee, "Scattering from dipoles loaded with diodes," *IEEE Trans. on Antennas and Propag.*, vol. 36, no. 11, pp. 1649-1651, Nov. 1988.

[66] D. M. Pozar, *Microwave Engineering*, 2nd Ed, Wiley, NY, 1998.

[67] A. Fung, and et al, "Tow-port vector network analyzer measurements in the 218-344 and 356-500 frequency bands," *IEEE Trans. Microw. Theory Tech.*, vol. 54, no. 12, pp. 4507-4512, Dec. 2006.

[68] G. F. Engen, "The six-port reflectometer: an alternative network analyzer," *IEEE Trans. Microw. Theory Tech.*, vol. 25, no. 12, pp. 1075-1080, Nov. 1977.

[69] Agilent Technologies, Inc., Application Note, *Exploring the Architectures of Network Analyzers*, Agilent AN 1287-2, [Online], http://cp.literature.agilent.com/litweb/pdf/5965-7708E.pdf.

[70] A. L. Samuel, "An oscilloscope method of presenting on the reflection coefficient plane," *Proc. IRE*, vol. 35, pp. 1279-1283, Nov. 1947.

[71] R. Caldecott, "The generalized multi-probe reflectometer and its application to automated transmission line measurements," *IEEE Trans. Antennas Propag.*, vol. 21, No. 4, pp. 550-554, July 1973.

[72] C. A. Hoer, "The six-port coupler: a new approach to measuring voltage, current, power, impedance, and phase," *IEEE Trans. on Instrum. and Measure.*, vol. 21, no. 4, pp. 466-470, June 1972.

[73] L. C. Oldfield, J. P. Ide, and E. J. Griffin, "A multistate reflectometer," *IEEE Trans. on Instrum. and Measure.*, vol. 34, no. 2, pp. 198-201, June 1985.

[74] J. R. Juroshek and C. A. Hoer, "A technique for extending the dynamic range of the dual six-port network analyzer," *IEEE Trans. Microw. Theory Tech.*, vol. 33, no. 6, pp. 453-459, June 1985.

[75] J. J. Yao and S. P. Yeo, "Six-port reflectometer based on modified hybrid couplers," *IEEE Trans. Microw. Theory Tech.*, vol. 56, no. 2, pp. 493-498, Feb. 2008.

[76] G. F. Engen, "Calibrating the six-port reflectometer by means of sliding terminations," *IEEE Trans. Microw. Theory Tech.*, vol. 26, no. 12, pp. 951-957, Dec. 1978.

[77] K. Hoffmann and Z. Skvor, "A novel vector network analyzer," *IEEE Trans. Microw. Theory Tech.*, vol. 46, no. 12, pp. 2520-2523, Dec. 1998.

[78] M. A. Abou-Khousa, M. A. Baumgartner, S. Kharkovsky, and R. Zoughi, "Novel and simple high frequency vector network analyzer (VNA)", In review, *IEEE Trans. on Instrum. and Measure.,* p. 8, March 2009.

[79] G. F. Engen, "A (historical) review of the six-port measurement technique," *IEEE Trans. Microw. Theory Tech.*, vol. 45, no. 12, pp. 2414-2417, Dec. 1997.

[80] S. Ulker and R. M. Weikle, "A millimeter-wave six-port reflectometer based on the sample-transmission line architecture," *IEEE Microw. Wireless Comp. Lett.*, vol. 11, no. 8, pp. 340-342, Aug. 2001.

[81] E. Bergeault, B. Huyart, G. Geneves and L. Jallet, "Characterization of diode detectors used in six-port reflectometers," *IEEE Trans. on Instrum. and Measure.*, vol. 40, no. 6, pp. 1041-1043, Dec. 1991.

[82] D. Rytting, "An analysis of vector measurements accuracy enhancement techniques," presented at the *RF and Microwave Symp. Exhibition*, 1980.

[83] Agilent Technologies, Inc, Data Sheet, *Agilent 8510C Network Analyzer*, [Online], http://cp.literature.agilent.com/litweb/pdf/5091-8484E.pdf.

[84] A. M. Abbosh, "Ultra-wideband phase shifters," *IEEE Trans. Microw. Theory Tech.*, vol. 55, no. 9, pp. 1935-1941, Sept. 2007.

[85] R.V. Garver, "Broad-band diode phase shifters," *IEEE Trans. Microw. Theory Tech.*, vol 20, no. 5, pp. 314 – 323, May 1972.

[86] B. Schiffman, "A new class of broadband microwave 90-degree phase shifters," I*RE Trans. Microw. Theory Tech.*, vol. MTT-6, no. 4, pp. 232–237, Apr. 1958.

[87] G. M. Rebeiz, G.-L. Tan; J. S. Hayden, "RF MEMS phase shifters: design and applications," *IEEE Microw. Mag.*, vol. 3, no. 2, pp. 72 – 81, June 2002.

[88] Z. Zhao and *et al*, "Ferroelectric phase shifters at 20 and 30 GHz," *IEEE Trans. Microw. Theory Tech.*, vol 55, no. 2, pp. 430 – 437, Feb. 2008.

VITA

Mohamed Ahmed Al-Ghanem AbouKhousa was born in Al-Ain, United Arab Emirates (UAE), on May 1, 1980. He received the B.S. EE degree (*Magna Cum laude*) from the American University of Sharjah (AUS), Sharjah, UAE in 2003, the M.S. EE degree from Concordia University, Montreal, QC, Canada in 2004, and the Ph.D. degree in electrical engineering from Missouri University of Science and Technology, Missouri S&T (formerly, University of Missouri-Rolla, UMR), MO, USA in 2009. His current research interests include microwave and millimeter wave measurement and instrumentation, imaging, numerical electromagnetic analysis, reconfigurable antennas, and wideband wireless communication systems.

Dr. AbouKhousa has to his credit more than 45 technical publications (journal papers, conference proceedings papers, and technical reports) in his area of expertise, in addition to three patent applications. In 1999, he received AUS Chancellor Scholarship and maintained it throughout his undergraduate study. In 2002, he became a Cisco Certified Networking Associate (CCNA) while he was undergraduate student at AUS. He was a recipient of the first prize of the IEEE IAS 2003 Myron Zucker Student Design Contest. In May 2003, he co-founded Glory Horizons Trading Company, LCC in Sharjah and Dubai, UAE. He is a student member of IEEE, and serves as a reviewer for IEEE Transactions on Antennas and Propagation and IEEE Transactions on Instrumentation and Measurement (Recognized as Outstanding Reviewer for the year 2008).